Phase Coherence in the Regime of Bilayer Exciton Condensation

Der Fakultät für Physik
der Universität Bielefeld
zur Erlangung des Grades eines
Doktors der Naturwissenschaften
- Dr. rer. nat. -
vorgelegte Dissertation

von

Lars Tiemann

geboren am 9. Juli 1975 in Bünde (Westfalen)

Referent:	**Prof. Dr. G. Reiss**
Korreferent:	**Prof. Dr. K. v. Klitzing**
Tag der Promotion:	**04.09.2008**

Max-Planck-Institut für Festkörperforschung
Stuttgart, 2008

Mistakes are the portals of discovery.
- James Joyce (1882-1941)

Contents

Abbreviations, Symbols and Physical Constants

Abbreviations:

2D	two-dimensional
2DES	two-dimensional electron system
2pt	two-terminal/point
4pt	four-terminal/point
AC	alternating current
AlAs	aluminium arsenide
a.u.	arbitrary units
BEC	Bose-Einstein condensate
CB	conduction band
CP(s)	composite particle(s)
DA	digital-analog
DC	direct current
DOS	density of states
DMM	digital multimeter
HF	high-frequency
MBE	molecular beam epitaxy
QW	quantum well
FWHM	full width at half maximum
GaAs	gallium arsenide
GPIB	general purpose interface bus
VB	valence band
VGND	virtual ground (of a current pre-amplifier)

Symbols:

$A_\square$	area of the sample/the 2DES
$A_\circlearrowleft$	area enclosed by cyclotron motion
$\Delta_{S,AS}$	single electron tunneling splitting (between the symmetric and antisymmetric state)
Φ	magnetic flux
Φ_0	magnetic flux quantum
ρ_{xx}	longitudinal resistivity
ρ_{xy}	Hall resistivity
σ_{xx}	longitudinal conductivity
σ_{xy}	Hall conductivity
ω_C	cyclotron frequency
μ	mobility
ν	filling factor
ν_{CP}	filling factor for composite particles
ν_{tot}	total filling factor (sum of all individual filling factors)
B	strength of the magnetic field (in Tesla)
d	(center-to-center) quantum well separation
$dG = dI/dV$	differential conductance
$D(E)$	density of states (general)
D_0	density of states (in a 2D system which is independent of E)
E_d	interlayer Coulomb interaction
E_F, ϵ_F	Fermi energy
E_{l_B}, E_l	intralayer Coulomb interaction
G	conductance
k_x, k_y	wave vector components in plane of a 2DES
k_z	wave vector components perpendicular to the 2DES
l_B	magnetic length
n, n_e, n_s	electron (sheet) density
t, t_{QW}	width of a quantum well
T	temperature

Physical Constants:

ε_0	$8.854187{\cdot}10^{-12}$	F m^{-1}	vacuum permittivity
e	$1.602176{\cdot}10^{-19}$	C	electron charge in Coulomb
h	$6.626068{\cdot}10^{-34}$	J s	Planck's constant
$\hbar = h/2\pi$	$1.054572{\cdot}10^{-34}$	J s	Planck's constant divided by 2π
k_B	$1.380650{\cdot}10^{-23}$	J K^{-1}	Boltzman constant
m_e	$9.109382{\cdot}10^{-31}$	kg	mass of an electron
$m^* = 0.067 \cdot m_e$	$6.103291{\cdot}10^{-32}$	kg	effective mass of an electron in GaAs
$R_K = h/e^2$	25812.807	Ω	von-Klitzing constant

Conversions:

1 eV	$\doteq$	$1.60217{\cdot}10^{-19}$	J
1 J/k_B	$\doteq$	$7.24293{\cdot}10^{+22}$	K
1 eV/k_B	$\doteq$	$\sim$11604	K

Chapter 1

Introduction

Macroscopic quantum systems such as superconductors and superfluids are the remarkable consequence of many of bosonic particles occupying the same lowest energy state, and thus forming a Bose-Einstein condensate (BEC). The feasibility of a BEC of excitons in semiconductors was suggested in 1962 [Bla1962], however, it has shown to be difficult to realize experimentally. Generally, excitonic condensation is expected to occur at low temperatures and low exciton densities n_X. While the critical temperature[1] $T_X \propto \frac{n_X^{2/3}}{M_X} \sim$ 1 K for exciton condensation is much larger than for an atomic BEC owing to the lower effective mass M_X of the excitons, the condensation of optically excited electron-hole pairs is limited by their finite life-time. There are certain possibilities to increase the excitonic life-time and make it much longer than the exciton thermalization time, however, only the design of two closely-spaced two dimensional electron systems allows to realize quasi-excitons with *infinite* life-time.

The foundation to create these quasi-excitons is the quantum Hall effect [Kli1980, Tsu1982] which is observed in two-dimensional electron systems under a strong perpendicular magnetic field B. Exposed to a sufficiently large B, the density of states of each of the two-dimensional systems (referred to simply as *double-layer* or *bilayer*, owing to their reduced dimensionality) will condense into a discrete set of dispersionless sub-bands, the Landau levels. The number of occupied states is then parameterized by the filling factor $\nu \propto n/B$. If the electron densities n are tuned to be identical in both layers, the two filling factors will simultaneously be at $\frac{1}{2}$ at a particular magnetic field. In this situation, where only the lowest Landau levels are half-filled, the dynamics of each layer is governed by Coulomb interactions (not by the kinetic energies of the electrons) where the electrons in *each* layer correlate their motion in order to comply with the Fermi exclusion principle. If the distance between the two layers is sufficiently small, of the order of 10 nm, then also Coulomb interactions between electrons of *opposite layers* will occur. Trying to maintain

[1] For a three dimensional semiconductor.

maximal distance between one another the electron configuration at this total filling factor $\frac{1}{2}+\frac{1}{2}$ is that where an electron in one layer is opposite a correlation space (or hole) in the opposite layer and vice versa. It can be shown that the ground state of this strongly correlated bilayer system is that of a Bose condensate of interlayer quasi-excitons. As the filling factor in each layer is at $\frac{1}{2}$, this correlated state is denoted as *total filling factor 1 state* or simply $\nu_{tot} = 1$ *state*. These interlayer excitons have infinite life-time, so their properties can be investigated via electrical transport experiments. However, an exciton is a charge-neutral object, and condensation may not lead to any spectacular electrical effect. Nevertheless, many experiments have shown remarkable properties owing to the interlayer-phase coherence associated with the Bose condensate. Interlayer tunneling experiments (which require independent Ohmic contacts to the two layers) have shown an I/V characteristic which has an astonishing resemblance to the one of the Josephson-effect of superconductivity. Other Magneto-transport experiments performed *on the common Hall bar geometry*, where currents of equal magnitude but opposite sign are sent through the two layers, have shown that (only) when the system approaches a total filling factor of 1, the Hall voltage and the longitudinal voltage (i.e., the voltage drop along the current direction) vanish. The vanishing Hall voltage indicates the existence of charge-neutral excitons, and the disappearance of all resistivity components may suggest that the system could indeed be a superconductor. However, the absence of dissipation may simply be owing to *dissipationless* one-dimensional edge channels which would mimic superfluidity/superconductivity at $\nu_{tot} = 1$. Thus, the use of a ring geometry (referred to as *Corbino ring*) instead of the common Hall bar was suggested for it excludes the influence of the edge channels and allows straightforward computation of the conductivity. The focus of this work is the investigation of the correlated $\nu_{tot} = 1$ state on these Corbino rings (and to a certain level, on the common Hall bars).

The chapter *Physics of the Quantum Hall Effect* will introduce to the physics of the integer and fractional quantum Hall effect which are essential for this work as it also defines many important parameters such as the filling factor.

The chapter *The $\nu_{tot} = 1$ Quantum Hall State in Bilayers* discusses the properties and physics of the (electron) bilayer at $\nu_{tot} = 1$ in detail and also introduces other equivalent pictures which the Bose condensed state can be mapped onto.

The chapter *Equipment and Samples* illustrates the step from the commonly used Hall bar geometry to the ring geometry both from the physical and technical side. It also discusses the experimental conditions for low temperature measurements.

The chapter *Interlayer Drag Measurements* starts with a theoretical introduction to the physics of the "drag experiments" where a current is sent through only one of the layers whereas the other is kept as an open circuit. The drag experiments on a Corbino device found that the conductance of the drive layer vanishes when the total filling factor approaches a value of one. At the same time, identical voltages across both the drive and drag layer can be observed. The results of these magneto-transport measurements on the Corbino device are shown in their dependence on the temperature and the strength of interlayer correlation. Also the differences between drag at $\nu_{tot} = 1$ and larger filling factors are discussed.

The chapter *Interlayer Tunneling* starts with the theoretical aspects of tunneling between uncorrelated and correlated layers. The empirical part begins with differential tunneling conductance experiments which will then be substituted by pure DC measurements. These experiments were able to demonstrate a critical behavior which had been expected but had not been shown before. The characteristics and properties of tunneling at total filling factor 1 are discussed. A new type of tunneling experiment is introduced which may be able to trigger excitonic supercurrents in the bulk.

Chapter 2

Physics of the Quantum Hall Effect

This chapter will give an introduction to two-dimensional electron systems (2DES) where the confinement of the electron motion in addition to strong perpendicular magnetic fields and low temperatures leads to the observation of the integer and fractional quantum Hall effect. While the integer quantum Hall effect is owing to the magnetic quantization of the single particle motion, the fractional quantum Hall effect arises when the systems dynamics are governed by Coulomb interactions between the electrons.

2.1 2-Dimensional Electron Systems

Modern molecular beam epitaxy (MBE) technology is able to produce semiconductor structures with a precision of a single atomic layer by evaporating pure materials with fast-shutting effusion cells onto a single wafer. Using this technology, heterojunctions can be grown which are composed of layers of different semiconductor materials with nearly identical lattice constants but non-equal band gaps. Of special interest are heterostructures formed by GaAs and AlAs (both zinc-blende structure with a lattice constant of approximately 0.56 nm) or their compound $Al_xGa_{1-x}As$, respectively. Usually, a composition parameter x of 0.33 is used. If GaAs (or AlAs) and $Al_xGa_{1-x}As$ are forming a heterojunction, the composition parameter influences the band structure properties at the interface.

Quantum wells (QW) consist of a thin layer of a semiconductor with a narrow band gap sandwiched between two layers of a semiconductor with a wide band gap. To obtain electrical conductance at cryogenic temperatures, the wide band-gap $Al_xGa_{1-x}As$ materials are doped, generally by Si. Owing to the alignment of the Fermi energies of both semiconductor materials, electrons originating from the doping site will re-distribute to the narrow band-gap GaAs quantum well, like in a pn-junction. The remaining positively charged ionized Si-dopant ions and the electron accumulation form a carrier depleted

space charge region. Depending on the relative positions of conduction and valence bands of the two semiconductor materials, a discontinuity (band bending) in the conduction and valence band will be formed. This discontinuity is the major advantage of hetero-junctions, since the locally modified band-structure can confine the motion of the charge carriers and produce a two-dimensional electron system (2DES). The confinement potential leads to a discreet set of energy sub-bands of the quantum well (as discussed later in this chapter). Since the doping terminates in sufficient distance from the GaAs (a method called *modulation doping*), electron scattering is strongly reduced. This technique leads to an increased mobility of the carriers which is required to observe fractional quantum Hall effects for instance.

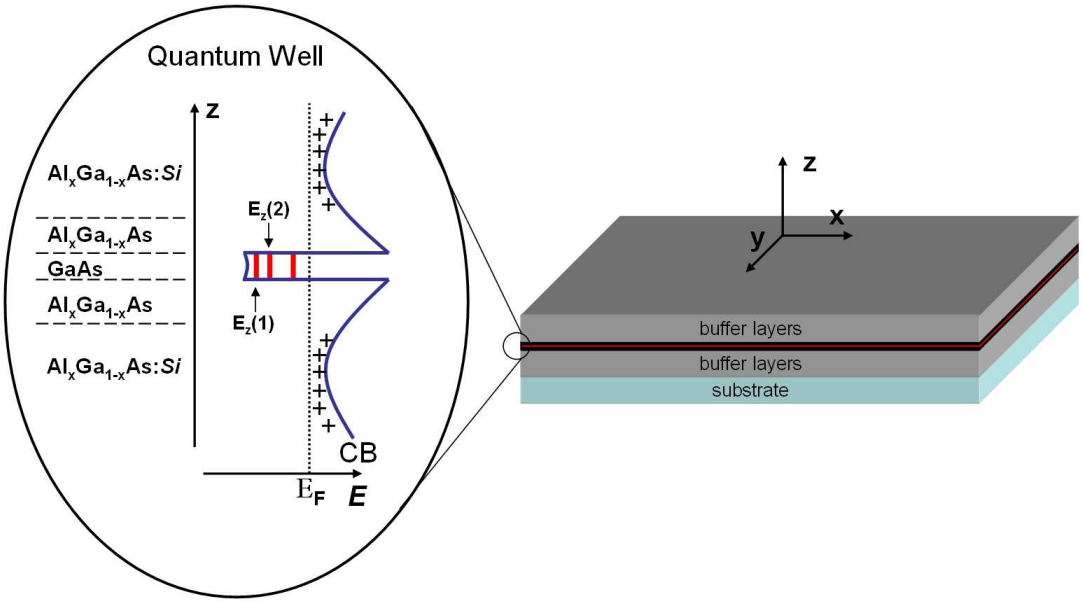

Figure 2.1: Schematics of a modulation-doped $Al_xGa_{1-x}As/GaAs/Al_xGa_{1-x}As$ single quantum well. The two lowest sub-bands are marked. At low electron densities and if $k_BT \ll (E_z(2) - E_z(1))$ only the lowest sub-band will be occupied.

2.2 Classical Magnetotransport: The Drude Theory

For a detailed discussion of the electronic transport in a 2-dimensional system, especially under strong perpendicular magnetic fields, quantum mechanical considerations are required. However, the *Drude model* of electrical conduction can be used to describe the transport properties of electrons when treated as classical, non-interacting (charged) objects, whose motion is affected by collisions.

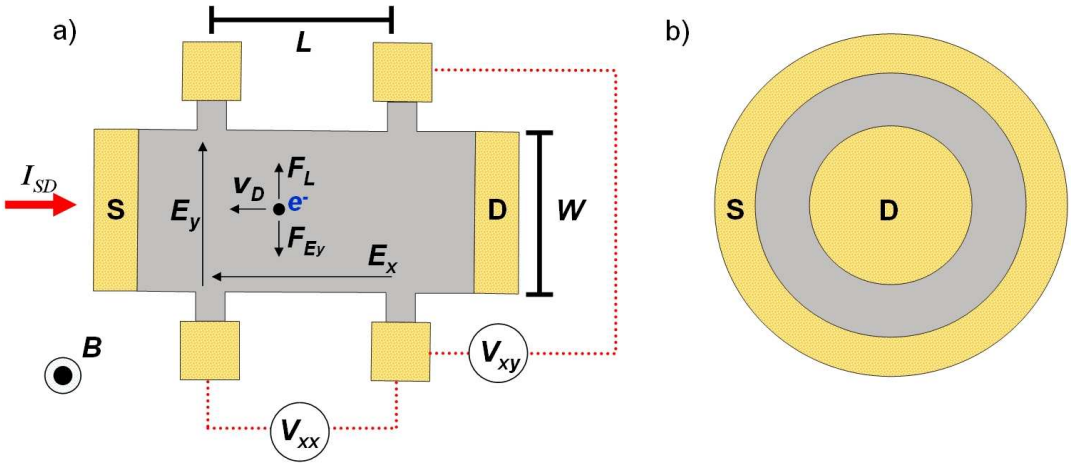

Figure 2.2: a) Hall bar and b) Corbino geometry. When a constant current I_{SD} is imposed on a Hall bar between source (S) and drain (D), the Lorentz force will lead to an accumulation of carriers on one side of the sample which creates an equilibrating electric field E_y. The boundary conditions of a Corbino geometry, which will be discussed in chapter 4, however enforce E_y=0. Yellow areas are Ohmic contacts.

The relaxation time approximation assumes that carriers are exposed to a homogeneous electric field E_x (see Figure 2.2) and a magnetic field B (with $\overrightarrow{B} \perp$ 2DES). The Lorentz force $\overrightarrow{F_L}$ will accelerate the electrons. However, permanent elastical scattering on impurities or phonons after the mean scattering time τ will impede the carriers from accelerating over the entire 2DES. In the steady state condition, the Lorentz force is balanced by the force due to scattering, i.e.,

$$\underbrace{\frac{m^*}{\tau}\overrightarrow{v_D}}_{Scattering} = \underbrace{-e(\overrightarrow{E} + (\overrightarrow{v_D} \times \overrightarrow{B}))}_{Lorentz\ force}, \tag{2.1}$$

where $\overrightarrow{v_D}$ is the electrons drift velocity which can be calculated as

$$\overrightarrow{v_D} = -\mu \begin{pmatrix} E_x + v_y B \\ E_y - v_x B \\ 0 \end{pmatrix}. \tag{2.2}$$

The newly defined parameter $\mu = \frac{e\tau}{m^*}$ is the *electron mobility*, i.e., the higher μ the higher the drift velocity. The Lorentz force which accelerates the electrons towards one side of the 2DES is opposed by the growing electric field $\overrightarrow{F_{E_y}}$ owing to the electron accumulation. In the steady state both forces balance one another so that $v_y = 0$. Note that this is the case for a Hall bar geometry. This allows to calculate the resistances using the definition of the current density $\overrightarrow{j} = -ne\overrightarrow{v_D}$

$$R_{xx} = \frac{V_{xx}}{I_{SD}} = \frac{E_x L}{j_x W} = \frac{1}{ne\mu}\frac{L}{W} = \rho_{xx}\frac{L}{W} \tag{2.3}$$

$$R_{xy} = \frac{V_{xy}}{I_{SD}} = \frac{E_y W}{j_x W} = \frac{B}{ne} \quad = \rho_{xy}. \tag{2.4}$$

More generally, magneto-transport in a 2DES can be described by Ohm's law $\overrightarrow{E} = \hat{\rho}\,\overrightarrow{j}$, with $\hat{\rho}$ being the resistivity tensor. With the two common definitions $\rho_0 = \frac{1}{ne\mu}$ and $\omega_C = \frac{eB}{m^*}$ (*cyclotron frequency*) and using $\rho_{yy} = \rho_{xx}$ and $\rho_{yx} = -\rho_{xy}$ (Onsager relation), the resistivity tensor reads

$$\hat{\rho} = \begin{pmatrix} \rho_{xx} & \rho_{xy} \\ \rho_{yx} & \rho_{yy} \end{pmatrix} = \rho_0 \begin{pmatrix} 1 & \omega_C\tau \\ -\omega_C\tau & 1 \end{pmatrix}. \tag{2.5}$$

Resistivity and conductivity are connected via tensor inversion, i.e., $\hat{\sigma}^{-1} = \hat{\rho}$ which also yields the Drude conductivity $\sigma_0 = \frac{1}{\rho_0}$. The conductivity tensor

$$\hat{\sigma} = \frac{1}{\rho_{xx}^2 + \rho_{xy}^2} \begin{pmatrix} \rho_{xx} & -\rho_{xy} \\ \rho_{xy} & \rho_{xx} \end{pmatrix} \tag{2.6}$$

is relevant for measurements on the Corbino device in Figure 2.2 b) where, in contrast to Hall bars, a constant voltage is applied and the current is measured (see chapter 4 for details). It should be emphasized that in strong magnetic fields, i.e., for $\tau >> \omega_C^{-1}$, the diagonal components of the resistivity and conductivity tensor are proportional to one another, whereas in the limit of resistivity scattering that both ρ_{xx} and σ_{xx} become zero which is characteristic for the quantum Hall effect.

2.3 The Landau Quantization

With increasing magnetic field, the Lorentz force will bend the electron motion from a straight line to an orbital trajectory. Within the low field regime with $\omega_C\tau \ll 1$, the electrons will only complete a small fraction of a full (cyclotron) orbit before they scatter and begin a new orbit with an arbitrary momentum vector. The situation is very different for $\omega_C\tau \gg 1$, where the electrons can complete multiple cyclotron orbits before a scattering event occurs. Under these conditions, the corresponding length scales require a quantum mechanical approach to explain the empirical observations. This quantum mechanical approach[1] will lead to the so-called *Landau quantization*.

[1] For a complete solution refer to [Coh1997, Lau1982, Cha1994].

Landau Levels

The Schrödinger equation for an electron in a magnetic field which is given by the vector potential $\overrightarrow{A}(x,y,z)$ is $H\psi(x,y,z) = E\psi(x,y,z)$. The corresponding Hamiltonian is

$$H = \frac{1}{2m^*}[\overrightarrow{P} + e\overrightarrow{A}]^2, \tag{2.7}$$

where $\overrightarrow{P} = -i\hbar\nabla$ is the momentum operator. Using the Landau gauge $\overrightarrow{A} = (0, B \cdot x, 0)$, the homogeneous magnetic field is in z-direction, i.e., $\overrightarrow{B} = \nabla \times \overrightarrow{A} = (0,0,B)$, and it is then convenient to separate the Hamiltonian to

$$H = \underbrace{\frac{p_z^2}{2m^*}}_{H_{||}(z)} + \underbrace{\frac{1}{2m^*}(p_x^2 + [p_y + eBx]^2)}_{H_{\perp}(x,y)} \tag{2.8}$$

so that $[H_\perp, H_{||}] = 0$ and consequently $E = E_\perp + E_{||}$. The two Schrödinger equations can be solved independently for a free electron in the xy-plane under B with $\psi(x,y)$ and for a free particle in z-direction with $\psi(z) = C_1 e^{ik_z z} + C_2 e^{-ik_z z}$. Since $H_{||}$ describes the kinetic energy of the free particle, its solution is easily found to be $E_{||} = \frac{\hbar^2 k_z^2}{2m^*}$. However, the (infinite) potential of the quantum well will confine the electron motion to between its boundaries. This boundary condition $\psi(z = -t/2) = \psi(z = +t/2) = 0$, where t is the well width, yields $k_z t = i\pi$ with $i \in \{0,1,2,...\}$ and thus result in an energy quantization of

$$E_z(i) = E_{||} = \frac{\hbar^2\pi^2}{2m^*}\frac{i^2}{t^2}. \tag{2.9}$$

The eigenfunction $\psi(x,y) = e^{ik_y y}\chi_n(x - x_0)$ of $H_\perp$ is a plane wave extended in y-direction and centered around the equilibration point x_0 of the eigenfunction of the Schrödinger equation for the quantum harmonic oscillator $\chi_n(x - x_0)$ [Cha1994]. Calculation of the corresponding eigenvalues yields the equally spaced energy levels of the harmonic oscillator, which are called *Landau levels*,

$$E_j = E_\perp = \hbar\omega_C\left(j + \frac{1}{2}\right) \qquad j \in \{0,1,2,...\}. \tag{2.10}$$

The electron spin has been ignored so far, however, for large magnetic fields, a Zeeman splitting term $E_{Zeeman} = sg\mu_B B$ has to be added to equation 2.4, where $s = \pm 1/2$ is the spin quantum number, g the Landé factor and μ_B the Bohr magneton.

Filling Factor and Density of States

Since the Landau energy levels depend only on the quantum number j, they are strongly degenerate (i.e., independent) with respect to the center $x_0 = k_y l_B^2$ of the j^{th} harmonic

eigenfunction $\psi(x, y)$ [Cha1994]. The newly defined length scale $l_B = \sqrt{\frac{\hbar}{eB}}$ is called *magnetic length*. Note that the commutator of the operators for the center coordinates is $[\hat{x_0}, \hat{y_0}] = il_B^2$, i.e., these coordinates are two non-commuting observables which makes a determination of their values uncertain to the order of l_B. The degeneracy (i.e. number of states per Landau level with the same energy E_j) is given by the sample length (in x-direction) divided by the distance between neighboring center coordinates Δx_0, i.e.,

$$N_L = \frac{L_y}{\Delta x_0} = \frac{L_x L_y}{2\pi l_B^2} = L_x L_y B \frac{e}{h} = \frac{\Phi}{\Phi_0} = \frac{A_\square}{A_\circlearrowleft}, \tag{2.11}$$

where $\Phi = L_x L_y B$ is the total magnetic flux through the area of the sample $A_\square = L_x Ly$ and $\Phi_0 = h/e$ the flux quantum. As equation 2.11 shows, the number of degenerate states is equal to the number of magnetic flux quanta that penetrate the 2DES or the total area of the sample $A_\square$ divided by the area enclosed by the cyclotron motion in real space $A_\circlearrowleft = h/eB$. Both the degeneracy of the Landau levels and their energetic separation $\hbar\omega_C$ increase linearly with B (see Figure 2.3).

One important quantity is the dimensionless density of electrons expressed as the Landau level *filling factor* ν. The filling factor is defined as the number of filled states by electrons $N_e = A_\square n_e$, where n_e is the electron density, divided by the number of available states N_L,

$$\nu = \frac{N_e}{N_L} = \frac{h}{eB} n_e. \tag{2.12}$$

Formally, the density of states of a 2DES exposed to a perpendicular magnetic field is a set of δ-functions at the energies of E_j,

$$D(E) = n_L \sum_n \delta(E - E_j) \qquad (B > 0\ T), \tag{2.13}$$

where $n_L = N_L/A_\square$ is the number of states per unit area. At zero magnetic field on the other hand, there is no Landau level quantization and the energy of the system is given by $E = E_z(i) + \frac{\hbar^2}{2m^*}(k_x^2 + k_y^2)$, i.e., parabolic sub-bands start off from the discrete energy $E_z(i)$ of the quantum well (see Figure 2.4 c)). The density of states $D(E)$ for these sub-bands is

$$D(E) = \underbrace{\frac{m^*}{2\pi\hbar^2}}_{\equiv D_0} \Theta(E - E_z(i)) \qquad (B = 0\ T), \tag{2.14}$$

where Θ is the step function[2]. Within a given sub-band, $D(E)$ is energy-independent[3], and as previously mentioned, at for low densities and at low temperatures only the lowest

[2]Not to confuse with the δ-function that describes the separation of the Landau levels!

[3]This is not true anymore if the effective mass m^* depends on the energy, such as in Graphene.

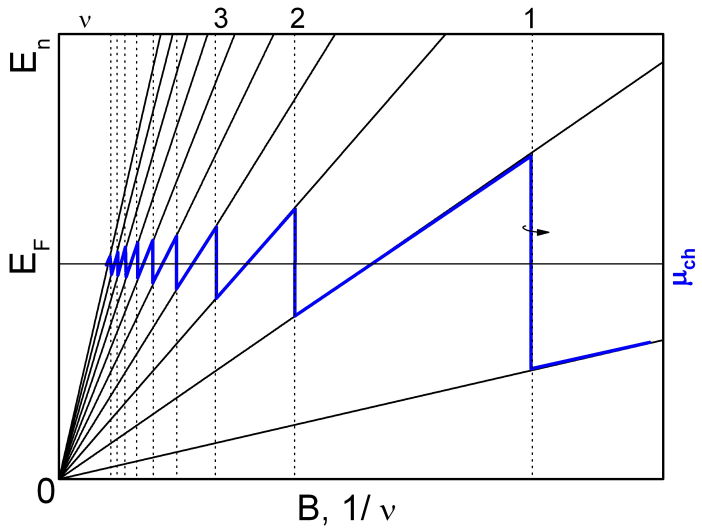

Figure 2.3: Chemical potential and Landau level energy as a function of the magnetic field. The chemical potential shows a jump of $\hbar\omega_C$ at all integer filling factors (as long as the Landau levels are not broadened by disorder). Figure from [Goe2004].

sub-band $E_z(1)$ is occupied. The Fermi energy which defines the number of occupied states is

$$E_F = \frac{2\pi\hbar^2}{m^*} n_e = n_e/D_0. \tag{2.15}$$

If Landau level quantization occurs, all electron states within the range of energy $\hbar\omega_C$ collapse onto a Landau level as shown on Figure 2.4 c).

2.4 The Integer Quantum Hall Effect

Calculation of the Hall resistance with equation 2.4 under the condition that an integer number of Landau levels are fully occupied yields the expression for the quantized Hall resistance which was found experimentally by Klaus von Klitzing [Kli1980] in 1980, i.e.,

$$R_{xy} = \frac{1}{\nu}\frac{h}{e^2} = \frac{1}{\nu} R_K \qquad \nu \in \{1, 2, 3, ...\}, \tag{2.16}$$

where R_K is the von-Klitzing constant. The quantization of the resistivity requires a minimal Landau level broadening by disorder (discussed next) and $k_B T < \hbar\omega_C$. Its value solely (!) depends on physical constants. The integer quantum Hall effect can be measured with an astonishing accuracy of approximately 10^{-9} and is used to define a resistance standard or to determine high precision values of the fine structure constant α.

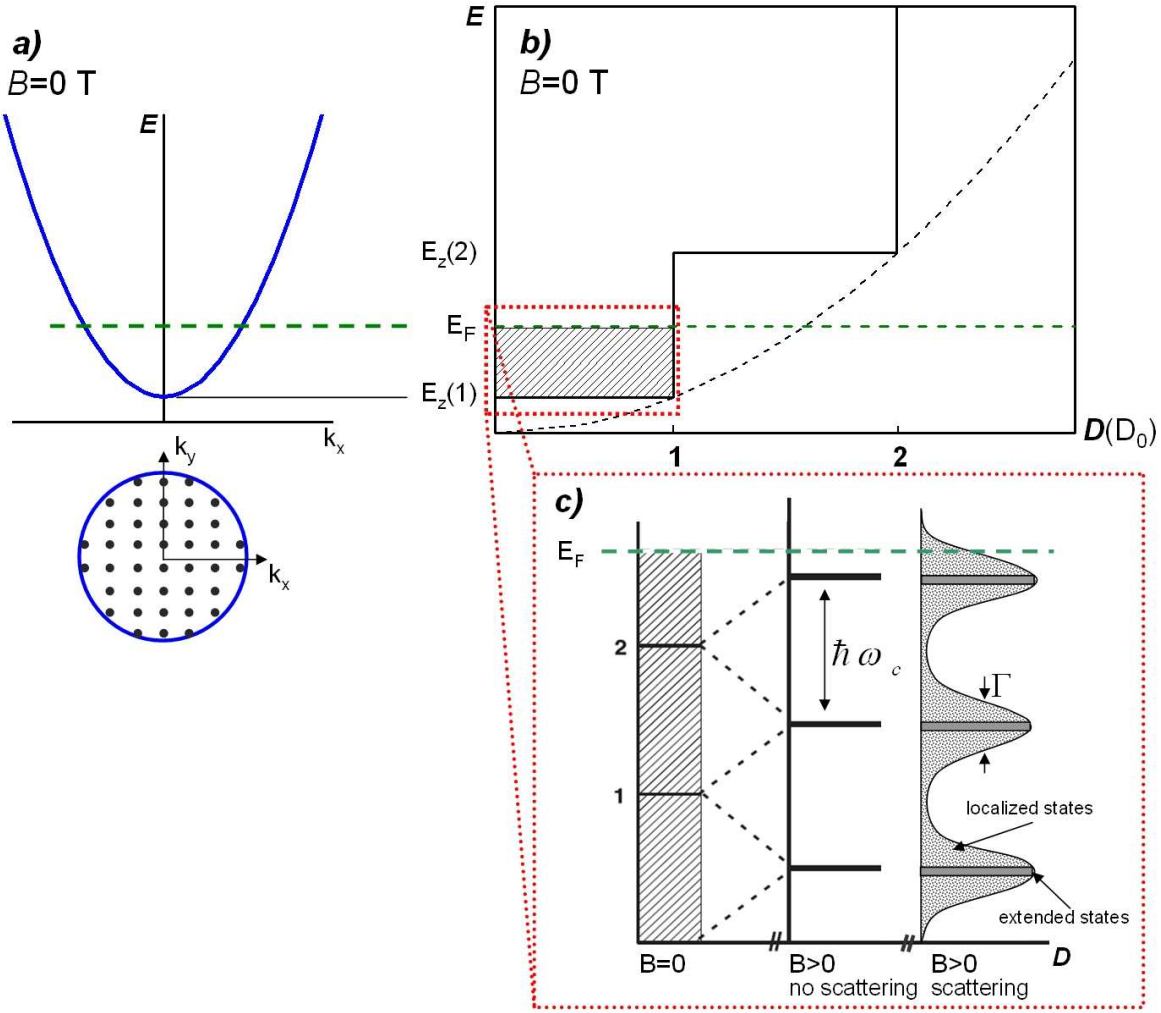

Figure 2.4: a) energy spectrum $\propto k^2$ and states (black dots) in momentum space which are filled up to the Fermi vector k_F for B=0 T. b) density of states D of a two-dimensional (solid line) and three-dimensional system (dotted line). Shaded area marks occupied states up to the Fermi energy E_F (dashed line). At low temperatures only the lowest energetic state $E_z(1)$ of the quantum well is occupied. c) blow-up of occupied states for $B \geq 0$ T. At a finite magnetic field $B \neq 0$ T the Landau level energies are separated by $\hbar\omega_C$. The Landau levels are theta functions in absence of an impurity potential or broadened into bands if impurity scattering occurs. Spins are ignored. Figure c) after [Jec2001].

Boundary Conditions: The Edge Channels

If the Fermi energy E_F lies between two Landau levels, no current would be able to flow from one arbitrary point (source) to another (drain) if the 2DES has no boundaries[4]. However, Hall bars are finite in size, thus at the sample edges a confinement potential $U(y)$ has to be added to the Landau energy E_j from equation 2.4 and will consequently bend the Landau levels upwards. Towards the sample edges the Landau levels will thus cross the Fermi energy E_F, giving rise to electron states at E_F. These states require only low energy excitations and run parallel to the sample edges, i.e., a current can flow between source and drain (see Figure 2.5) along one-dimensional (1D) *edge channels*.

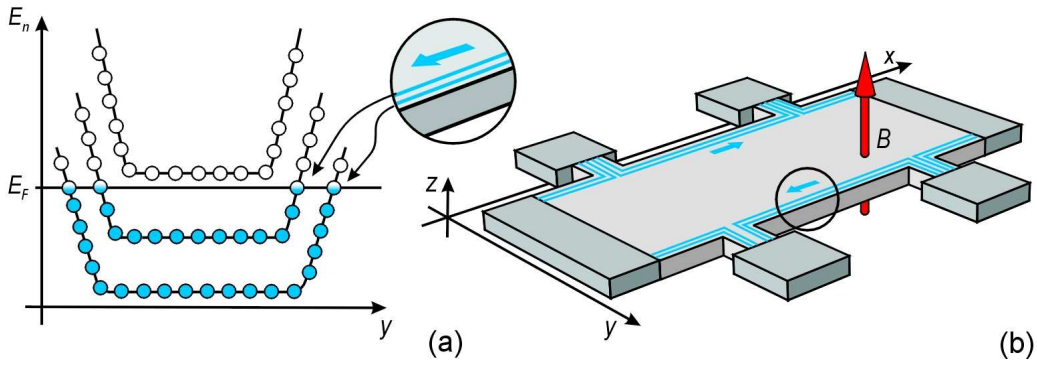

Figure 2.5: a) the Landau levels bend upwards due to the confinement potential $U(y)$. At the edges they cross the Fermi energy allowing dissipationless electron transport along one-dimensional edge channels. b) the Hall bar at filling factor 2 with the two counter-flowing edge channels at each sample boundary. Figure from [Goe2004].

As long as E_F lies between two Landau levels, there are no bulk states available and backscattering between opposite sample edges is suppressed. The current that flows along an individual edge channel between source and drain contacts is thus dissipationless, i.e., no voltage difference exists between any two points along a single edge[5] (the longitudinal voltage is zero).

The Landauer and Büttiker approach [Bue1988] to this edge channel concept is also able to explain the quantization to integers of h/e^2. The density of states of a single edge channel with index j that connects two electron reservoirs which are at the electrochemical potential μ_S and μ_D is $D(E) = (2\pi\hbar v_j)^{-1}$, where v_j is the longitudinal velocity at the Fermi energy along this channel. Assuming ideal Ohmic contacts, the current that flows owing to the potential difference $\Delta\mu = \mu_S - \mu_D \equiv eV$ is then $I_j = ev_j D(E)\Delta\mu = \frac{e}{h}\Delta\mu$.

[4] As it will be shown later that is exactly the situation for a Corbino device at all integer filling factors.

[5] This is only true if these two points are not the source and drain contacts themselves which then would include the Hall voltage.

The total current is thus the sum over all edge channels given by the filling factor, i.e., $I = \sum_j I_j = \nu \frac{e}{h} \Delta\mu$. Note that the velocity is $v \propto \frac{\partial U(y)}{\partial y}$ [Dat1995], i.e., the edge states at opposite sample edges carry current of opposite direction.

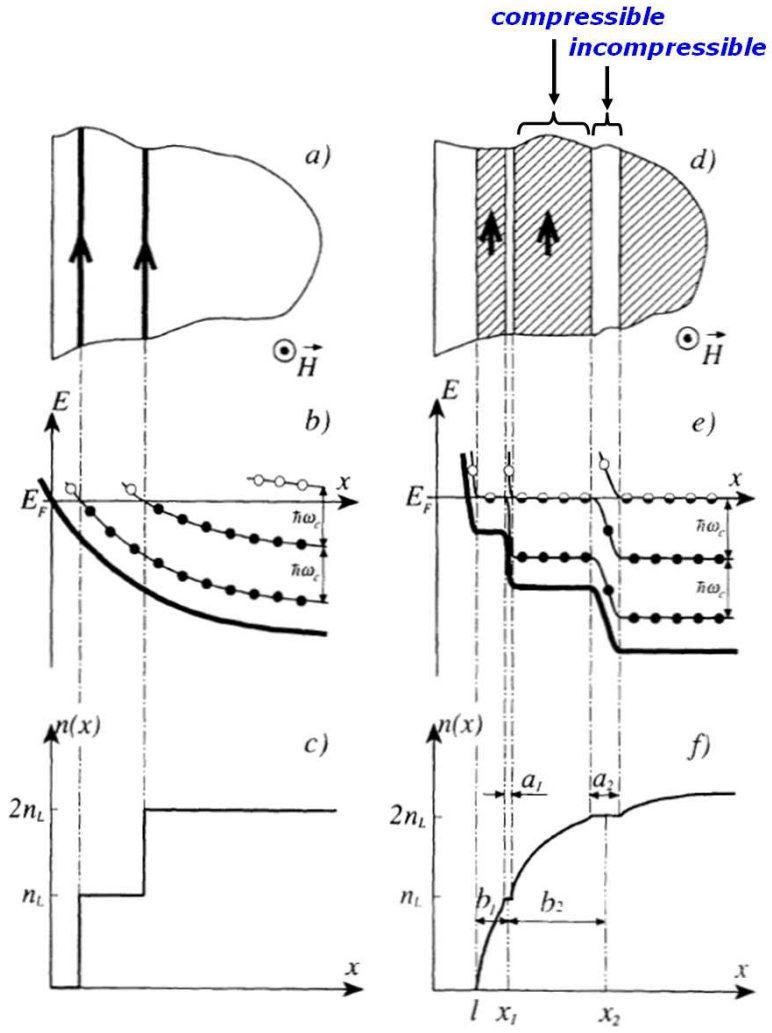

Figure 2.6: Left hand side: a), b) one electron picture of edge states. c) electron density as a function of the distance to the boundary. Right hand side: d)-f) electrostatic picture: shaded areas are compressible strips (non-integer filling factors), unshaded areas are the incompressible ones (integer filling factors). Figure from reference [Chk1992].

In this edge channel picture, the electron density should jump from zero at the very edge to the value of the first edge channel as depicted in Figure 2.6 c), and the width of each edge channel should be of order of the magnetic length l_B. However, as calculations [Chk1992, Lie1994] have shown, the density gradually increases within the depletion length. In their quantitative electrostatic theory which includes the screening effects of

the electrons in the 2DES, the electrostatic potential in the region occupied by the 2DES changes in a steplike manner due to the formation of two different types of alternating edge strips: a) the *compressible* strips which are pinned at the Fermi energy (i.e., like a metallic conductor), where the electron density increases towards the bulk. Electrons can be added while leaving the electrochemical potential unchanged. b) the *incompressible* strips where there are no states at E_F (Fermi energy is in the mobility gap) and the electron density is constant. For experimental details of the potential distribution in a Hall bar refer to [Ahl2002].

Landau Level Broadening and Disorder Potential

Generally, a quantized Hall resistance is expected if no scattering between compressible strips from opposite (Hall) edges occurs, i.e, when there exists a wide incompressible strip in between. As Figure 2.3 shows, in ideal samples such incompressibility exists only for an infinitesimal small magnetic field region, where the chemical potential is located within the energy gap. However, all real samples are finite in width, and at the sample edges there exists a continuum of states which stabilizes the Fermi energy in the gap of the bulk region (i.e., there is no sharp jump of the chemical potential). Yet, the density of states of these compressible edge states is not big enough to explain the width of the Hall plateaus which are observed in experiment. That means that the density of states in the bulk region, instead of consisting of δ-functions, must have states between the Landau levels [Gud1987]. Impurity disorder such as donor atoms and crystalline defects give rise to a random impurity potential $U_{Disorder}(r) = \sum_i u_i(r - r_i)$, as a sum over all single potentials u_i, which has to be added to equation 2.8. These potential fluctuations over the entire sample area broaden the Landau levels into Gaussian-shaped distributions (the degeneracy of the states with different center coordinates (x_0,y_0) is lifted). For long range potential fluctuations (which exceed the magnetic length l_B) this leads to states near the Fermi energy within the bulk. Like at the sample edges, one-dimensional conducting channels emerge, which however form a closed trajectory around the individual potentials u_i. Since the electrons in these states are "captured" by u_i, they cannot contribute to the current from source to drain and are consequently called *localized states*. The energetic range of localized states is called *mobility gap*. The center states of each broadened Landau level are comprised of current carrying states, the so-called *extended states* which lie close to the original E_j, calculated with equation [Lau1982, Pra1987].

The impurity potential model combined with the edge channel picture can now give a qualitative explanation to describe the empirical features of the integer quantum Hall effect: if E_F lies in the center of the mobility gap, we find $\rho_{xx} = 0$ and $\rho_{x,y} = R_K/\nu$, i.e., the electrons move along equipotential lines which run parallel to the sample edges. If the

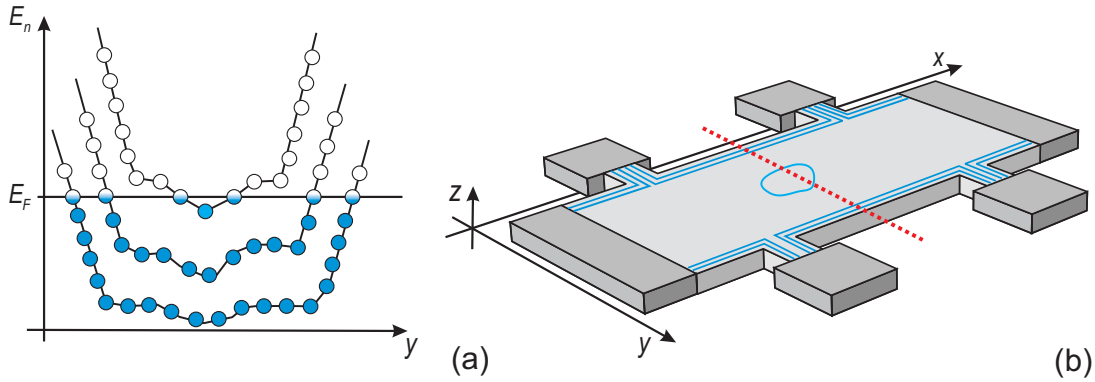

Figure 2.7: a) Landau level potential distribution with disorder along the red line in Figure b) for filling factor 2. A single exemplary disorder potential creates a closed one-dimensional conducting channel within the bulk of the topmost Landau Level. b) in addition to edge channels, the disorder potential (at cross section in red) yields localized states.

Fermi energy is shifted towards the next Landau level by increasing B (which will reduce the filling factor), individual areas of localized states will appear which are distributed over the sample area. By further increasing B, they will increase in spatial extension. Eventually, different regions of localized states percolate into a single extended state that covers the entire sample and connects both sample edges. In this situation backscattering between opposite sample edges is possible where $\rho_{xx} > 0$ and $\rho_{x,y}$ climbs to the next quantized step.

The oscillations in the longitudinal resistance are called *Shubnikov-de Haas Effect*. As outlined above, it is the result of the density of states, or the broadened Landau levels, respectively, which oscillates as a function of the magnetic field. The minima are periodic in $1/B$ as

$$\Delta\left(\frac{1}{B}\right) = \frac{2e}{hn}, \tag{2.17}$$

where it is assumed that the magnetic field B is small enough and no spin splitting has occurred yet. To observe Shubnikov-de Haas oscillations both $\hbar\omega_C > \Gamma$ (to assure sufficient separation between the Landau levels) and $\hbar\omega_C \gg k_B T$ (to avoid thermal excitations to a Landau level of higher energy) have to be met.

2.5 The Fractional Quantum Hall Effect

In high mobility (and low density[6]) samples, additional features in the longitudinal and transversal resistance can be observed mainly for $\nu < 2$. Since all magnetic field-induced energy gaps (i.e., the integer quantum Hall energy gaps of $\hbar\omega_C$) are exhausted for $\nu < 1$, these additional gaps which are shown in Figure 2.8) must be of different origin than the Landau quantization.

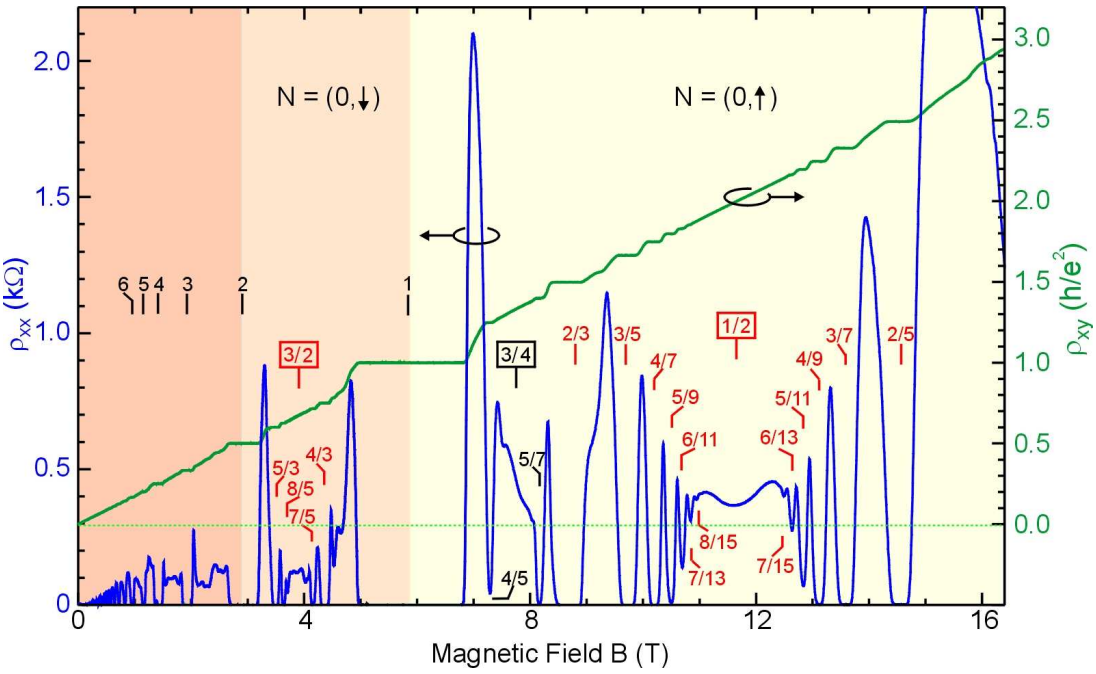

Figure 2.8: Longitudinal and Hall resistivities for a high mobility sample. Fractional features are observable in the lowest (spin-split) Landau level $N = (0, \downarrow)$ and $N = (0, \uparrow)$. Filling factor $\nu = 1/3$ lies beyond 16 T. Figure from [Goe2004].

The fractional quantum Hall effect was first observed in 1982 by Tsui *et al.* [Tsu1982] at filling factor $\nu = 1/3$. Robert Laughlin [Lau1983] developed a model that was not only able to account for this $\nu = 1/3$ state but for all $1/q$ fractional quantum Hall states (where q is an odd integer) found later on. These energy gaps are the result of interactions between the electrons, where the electrons are avoiding one another by correlating their relative motion due to the Coulomb interaction. This is only possible because for $\nu < 1$ there are (unlike at all integer filling factors) vacant states in the (lowest) Landau level available, allowing this "spatial redistribution". The interaction effects can be accounted for by including

[6]To observe effects at accessible magnetic fields.

$$\propto \sum_{j \neq k} \frac{e^2}{\mid \overrightarrow{r}_j - \overrightarrow{r}_k \mid} \tag{2.18}$$

to the Hamiltonian of equation 2.8. Laughlin's fermionic many-body ground state trial wave function is aside from a factor

$$\Psi^{1/q}(z_1, z_2, ..., z_N) \propto \prod_{j \neq k}^{N} (z_i - z_k)^q, \tag{2.19}$$

where the position (x_j, y_j) of each electron j is given by the complex representation $z_j = x_j - iy_j$. This wave function obeys the Pauli principle because if two particles approach one another, i.e., $z_j \longrightarrow z_k$, one of the factors of the product will zero and $\Psi^{1/q}$ vanishes rapidly. Also, due to the antisymmetry requirement, under particle exchange (electrons are Fermions) the Laughlin states are restricted to odd values of q. Addition or subtraction of a single electron disturbs the order described by $\Psi^{1/q}$ at a considerable energetic cost. For that reason, all $1/q$ states are referred to as ground states [Eis1990a].

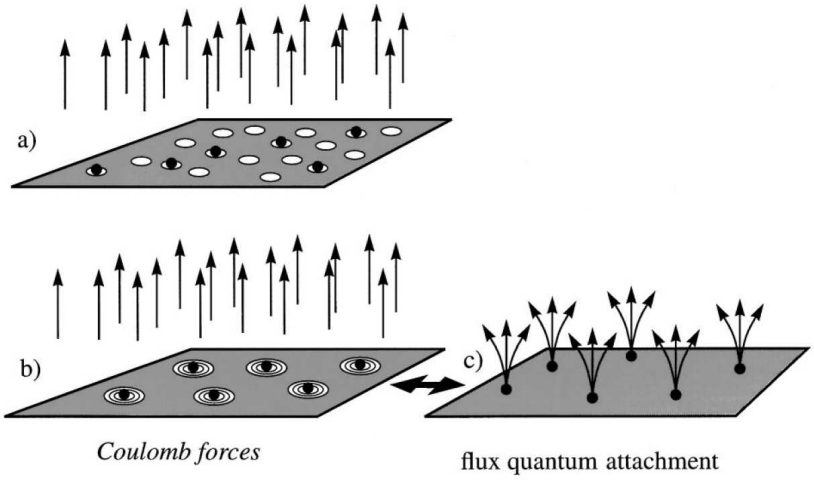

Figure 2.9: Electron-vortex system at filling factor 1/3. Black dots are the electrons, white circles are vortices and the arrows represent the flux quanta. a)-b) the spare vortices are placed onto the other electrons. c) since a vortex can be represented by its flux quantum, each electron is attached to three quanta. Figure from reference [Sto1999].

Quantum mechanically, the single electron wave functions are "smeared out" over the entire 2D system, i.e., the probability of finding a single electron at a certain location is uniform over the whole plane. The electrons behave thus as a featureless liquid. An impinging magnetic field can be viewed as creating vortices (*topological defects*) in this homogeneous liquid of charge, with one vortex per flux quantum $\phi_0 = h/e$. The charge

is displaced from the center of each vortex. As in case of the electrons, the probability of finding a vortex at a certain location is uniform over the entire plane as well. Since electrons and vortices are objects of "opposite" charge, it is energetically beneficial to place one onto the other because it reduces the repulsion between electrons[7]. For filling factor 1 there are the same number of electrons and vortices, at filling factor 1/3, however, the number of vortices is 3 times larger. The system can reduce its electrostatic Coulomb energy by placing more vortices onto each electron and thus increase the relative distance between the electrons. Conceptionally, it is equivalent to replace the vortices by the corresponding flux quanta. Electrons plus flux quanta can be viewed as a *composite particle* [Jai1989,Sto1999]. Generally, these composite particles are either Fermions if the number of attached flux quanta is even (such as for the $\nu = 1/2$ state), or bosons, if the number of flux quanta is odd. The composite particles thus obey either the Bose statistic or the Fermi statistic. For *exactly* $\nu = 1/3$ the composite particles are bosons and *all* flux quanta are attached to electrons, leading to a new ground state and the observed energy gap. When the magnetic field deviates from $\nu = 1/3$ by $+\Delta B$, more vortices are created which do not attach to electrons because this would disturbed the ground state. Instead, for each additional vortex there is a charge-deficit of $e/3$, i.e., each vortex can be considered as a *quasihole*. Equivalently, for $-\Delta B$ *quasielectrons* with excess-charge of $e/3$ are created. These quasiparticles can move freely through the 2D system and transport electrical charge, however, as in the integer quantum Hall effect, they can get trapped at weak random impurity potentials.

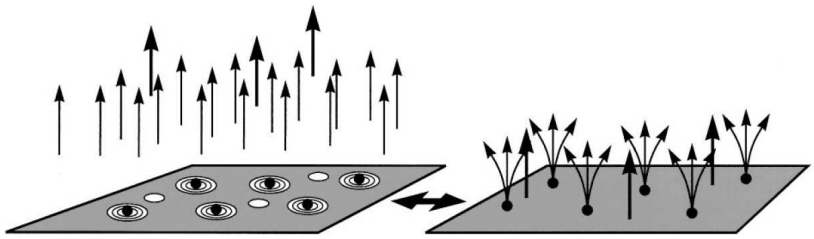

Figure 2.10: At higher magnetic fields than $\nu = 1/3$ additional vortices, i.e., quasiholes, are created each having a charge-deficit of $e/3$. These quasiparticles can move freely through the 2D system. Figure from reference [Sto1999].

The composite fermionic particle picture allows to understand the fractional quantum Hall effect in terms of an integer quantum Hall effect of composite particles. When the

[7]This is not very intrusive because now each electron is BOTH part of the uniform liquid AND at the center of a vortex. However, this can be viewed as satisfying the Pauli principle. In this configuration, no two electrons can be at the same position.

electrons attach themselves to a number m of flux quanta $\phi_0 = h/e$ with $m \in \mathbb{N}$, it will (partly) cancel the external magnetic field. The system then experiences a reduced effective magnetic field of $B^* = B - m\phi_0 n_e$. A composite particle filling factor can be defined as $\nu_{CP} = \phi_0 \frac{n_e}{|B^*|}$. Introducing $B(\nu_{CP})$ into the regular filling factor ν (equation 2.12) yields

$$\nu = \frac{\nu_{CP}}{m\nu_{CP} \pm 1} \qquad \nu_{CP} \in \mathbb{N}/0, m \in \mathbb{N}. \tag{2.20}$$

Table 2.1 shows some examples how to reduce the regular filling factor ν with a fractional value to an integer value of the composite particle filling factor ν_{CP}. For exactly $\nu = 1/2$, all flux quanta are attached to electrons again (two per electron) so that the resulting composite Fermions reside at zero effective field. Since these composite particles are Fermions, they will successively fill up all available energy states. Thus, $\nu = 1/2$ does not exhibit an energy gap, and the Hall line is featureless as it is for electrons at $B = 0$ T. The oscillating features around $\nu = 1/2$ visible in Figure 2.8 resemble those around $B = 0$ T [Sto1999].

ν	ν_{CP}	m
1/3	1	2
2/5	2	2
3/7	3	2
⋮	⋮	⋮

Table 2.1: Three examples of the integer quantum Hall effect of composite particles.

Certain fractional quantum Hall states can be observed in the second Landau level (such as $\nu = 5/2$) due to the spin degree of freedom, however, no fractional quantum Hall effect have been observed at higher filling factors.

Chapter 3

The $\nu_{tot} = 1$ Quantum Hall State in Bilayers

In this chapter the concept and properties of the *total filling factor 1 ($\nu_{tot} = 1$)* state are discussed, which displays an energy gap when the filling factors of two closely spaced 2DES are simultaneously at 1/2. Its origin is attributed to Coulomb interactions between all electrons in the two 2DES and it is thus comparable to a fractional quantum Hall state.

3.1 Electron Bilayer Systems

Generally, a bilayer system consists of two-closely spaced quantum wells (due to their dimensionality referred to as "layers") which are populated by charge carriers. The total filling factor 1 state can emerge if the carriers of both layers are either electrons or holes, or electrons for one layer and holes for the other. For this work exclusively *electron bilayer systems* were investigated. Using equation 2.9, the energy gap between the lowest and the following sub-band of a quantum well with width t=19 nm can be calculated to be $\Delta E = E_z(2) - E_z(1) \approx 360$ K. Since the intrinsic densities do not exceed $5 \cdot 10^{14}\mathrm{m}^{-2}$, it can definitely be assumed that during all measurements the electrons will occupy only the lowest subband[1].

Quantum-mechanically, the wave function of an electron in a quantum well with finite potential height has a finite decay length into the confinement potential (barrier). If the barrier between two quantum wells is smaller than this decay length, the two wave functions will overlap. This finite probability of having the particle in the barrier and

[1]Generally, the sub-band population can be calculated as the integral of the product of density of states D_0 and the Fermi-Dirac function that gives the probability of occupation of a state $\int_{subband} D_0(exp[(E - E_F)/k_BT] + 1)^{-1}dE$

in the other well is generally referred to as *(interlayer) tunneling*, and the amount of the overlap quantifies the tunneling strength. Tunneling thus violates separate charge conservation in each layer. If the overlap is strong, it forces the (degenerate) ground state to split into a bonding state $\Psi_+ = \frac{1}{\sqrt{2}}(\Psi_1 + \Psi_2)$ with lower energy and an antibonding state $\Psi_- = \frac{1}{\sqrt{2}}(\Psi_1 - \Psi_2)$ with higher energy, to satisfy the Pauli exclusion principle. This is analogous to the hydrogen molecule where the formation of a pair of bonding and antibonding orbitals occurs once two hydrogen atoms 1 and 2 are brought together. Each electron will have a wave function which is either symmetric or antisymmetric relative to the barrier. The corresponding energies for a double quantum well are separated by an energy gap $\Delta_{S,AS} = E_{AS} - E_S$, which is called *single electron tunnel splitting* [Har1999]. Figure 3.1 shows the symmetric and antisymmetric states and the single electron splitting for the double quantum well structure if (strong) tunneling occurs.

The application of a perpendicular magnetic field will split E_S and E_{AS} into a set of spin-split Landau levels [Boe1990]. For very large Δ_{SAS} ($\gg E_l$) the system is essentially a single wide quantum well. All lower lying symmetric states are occupied, while all antisymmetric states are empty. The total filling factor 1 quantum Hall state would be the ordinary $\nu = 1$ integer Hall effect [Sar1997] of a wide quantum well with double the density of the single layer.

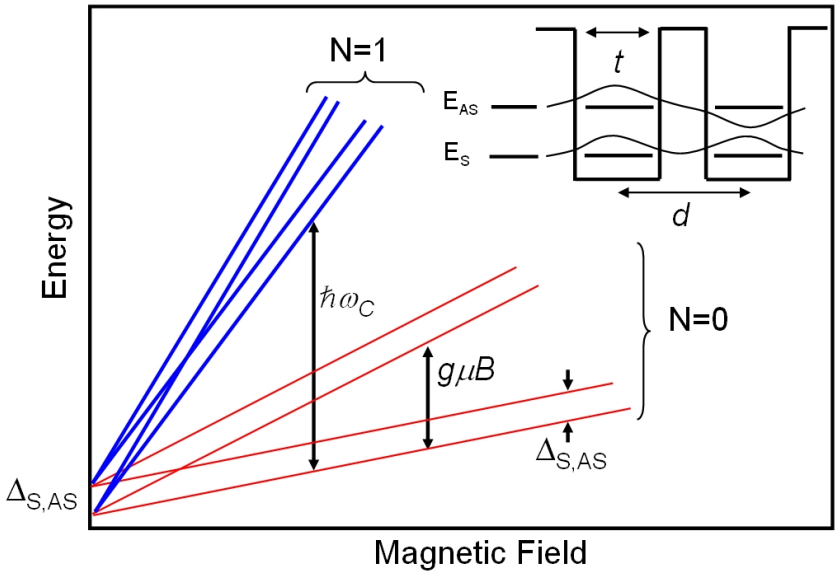

Figure 3.1: Schematic energy diagram of the single electron tunnel splitting $\Delta_{S,AS}$. As the magnetic field is increased, the energy states split due to Landau level quantization (N: Landau level index) and lifting the spin degeneracy (Zeeman term). The inset shows the symmetric and antisymmetric states. After [Boe1990].

The single electron splitting $\Delta_{S,AS}$ can be calculated by numerically solving the Poisson

and Schrödinger equation self-consistently. Its value for a (19/9.6/19) nm double quantum well system is estimated[2] to be approximately 150 μK, which is in good agreement with earlier reports on comparable double quantum well structures [Spi2000,Kel2004] that were used to investigate the total filling factor 1 state.

3.2 Weak Tunneling Limit

Since $\Delta_{S,AS}$ can vary between 0 and hundreds of Kelvin, it is important to determine its value relative to the relevant Coulomb energy E_l. At the magnetic field where the total filling factor 1 state is found to be firmly established (at about 2 T for $n_{tot} = 4 \cdot 10^{14}$ m^{-2}), the corresponding Coulomb energy E_l is about $1.3 \cdot 10^{-20}$ J or equivalently $E_l/k_B \approx 950$ K. So, even a $\Delta_{S,AS}$ of order of the measured activation energy at total filling factor 1 (i.e., $\approx$ 0.5 K, see chapter 5) would yield $\Delta_{SAS}/E_l \approx 5 \cdot 10^{-4}$. In this limit, the $\nu_{tot} = 1$ quantum Hall state is mainly the result of the competing Coulomb interactions of the electrons within the individual layer and electrons of opposite layers. Like in the fractional quantum Hall effect, these Coulomb interactions drive all electrons to minimize their exchange energy and thus form a new bilayer ground state. However, the observed energy gap at $\nu_{tot} = 1$ can even survive the limit $\Delta_{S,AS} \to 0$ so that the associated phase transition is believed to display a purely *spontaneous* breaking of the systems symmetry (what this means will become clear further in the text).

In addition to the filling factor, relevant parameters for the total filling factor one state are the *intra*layer Coulomb energy $E_l = \frac{e^2}{2\pi\epsilon l_B}$, with the magnetic length $l_B \propto B^{-0.5}$, and the *inter*layer Coulomb energy $E_d = \frac{e^2}{2\pi\epsilon d}$, with the center-to-center quantum well separation d (a fixed parameter). In the weak tunneling limit, theoretical calculations (and all experiments) show that the $\nu_{tot} = 1$ quantum Hall state cannot exist for arbitrarily weak interlayer interactions. Instead, a phase transition from two uncorrelated layers to the (excitonic) bilayer ground state occurs when the ratio $E_l/E_d = d/l_B$ is smaller than about 2 [Yos1989,Fer1989]. This ratio is often referred to as the *effective layer separation* or *coupling parameter*. Figure 3.2 shows the empirical phase diagram for a bilayer system at a total filling factor of 1. Only below the dashed line, the new $\nu_{tot} = 1$ quantum Hall state was observed in a Hall bar geometry.

The energy gap of the $\nu_{tot} = 1$ state (which can be measured via temperature activation, see chapter 5) should be dominated by $\Delta_{S,AS}$ if tunneling is strong, while it is expected to be independent of it, if the $\nu_{tot} = 1$ state is solely due to Coulomb interactions. In a tilted magnetic field with angle Θ, i.e., when an in-plane magnetic field component is

[2] I thank K. Muraki for running the calculations on a professional Poisson solver which provided the required resolution.

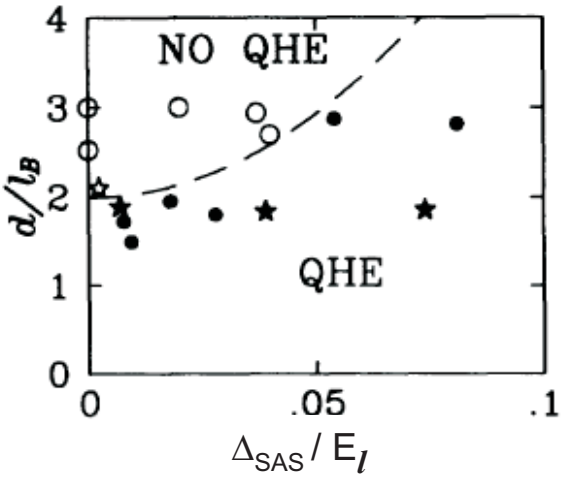

Figure 3.2: The phase diagram for the bilayer $\nu_{tot} = 1$ quantum Hall state. Solid symbols represent samples that show a quantum Hall effect while open symbols indicate samples that do not. Taken and modified from [Mur1994].

added, the single particle tunneling $\Delta_{S,AS}(\Theta)$, which is associated with hopping between layers, should reduce [Hu1992]. In their experiments Murphy *et al.* [Mur1994] found that the energy gap of the $\nu_{tot} = 1$ state partly depends on tunneling for small angles but is nearly angle-independent for larger angles[3].

3.3 The $\nu_{tot} = 1$ Ground State

At filling factor 1/2 the real *spin* degree of freedom can be ignored[4] because of complete spin alignment owing to the strong magnetic field. However, the physics of bilayers at $\nu_{tot} = 1$ can be described by using a spin analogy (the pseudo- or iso-spin) of the *layer index* degree of freedom, where a pseudo-spin up $|\uparrow\rangle$ and down $|\downarrow\rangle$ refer to the carrier in the top and bottom layer (see Figure 3.3).

A generalization of Laughlin's wave function was given by Halperin which describes systems with two different spin-split Landau states at the same energy (a level crossing). In terms of the pseudo-spin language the ground state of the bilayer system for $d \to 0$ can be expressed as [Hal1983]

$$\Psi_{111} \propto \prod_{i<j}^{N\uparrow}(z_{i,\uparrow} - z_{j,\uparrow})^1 \prod_{k<l}^{N\downarrow}(z_{k,\downarrow} - z_{l,\downarrow})^1 \prod_{m,n}^{N\uparrow,N\downarrow,}(z_{m,\uparrow} - z_{n,\downarrow})^1, \tag{3.1}$$

where $z_{s,\uparrow/\downarrow} = x_s + iy_s$ are the complex coordinates of the s^{th} electron in the top ($\uparrow$) or bottom ($\downarrow$) layer, and N is the number of electrons (which by definition should be

[3] This was for samples with a barrier of 3 nm - 4 nm, i.e., about 2-3 times smaller than the barriers of samples that were used in this work.

[4] This is only correct for strong magnetic fields, where the Zeeman splitting is large. In the regime where the $\nu_{tot} = 1$ state occurs, the spin alignment is not complete. Recent experiments [Giu2008] suggest that this may be of certain relevance for the $\nu_{tot} = 1$ state.

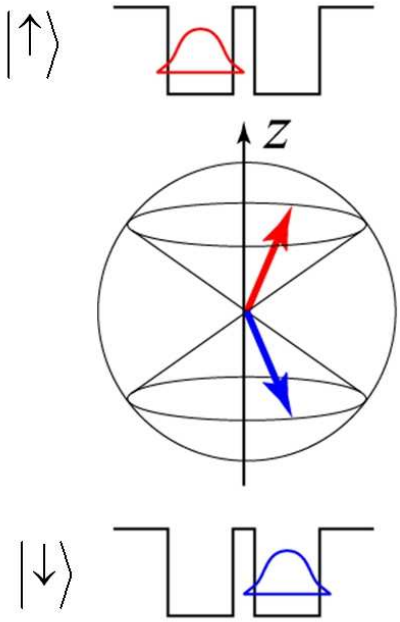

Figure 3.3: Pseudo-spin representation of a double quantum well system when the carrier is either in the top (red vector) or the bottom (blue vector) layer. Figure from [Mra2008].

identical for both layers and conserved if tunneling is zero, i.e., $N \downarrow + N \uparrow$ is a good quantum number). Like the Laughlin wave function, the Halperin (111) wave function goes to zero as soon as electrons in either the upper or the lower layer approach one another. However, it also goes rapidly to zero whenever $z_{m,\uparrow} \rightarrow z_{n,\downarrow}$, i.e., when electrons of opposite layers approach each other. For $d = 0$ this represents a single layer with a completely filled lowest Landau level, because each positional degree of freedom is occupied. For small effective layer separations d/l_B, the above wave function describes in good approximation the bilayer system in the ground state where all electrons are maximally spaced to minimize their exchange energy, as shown in Figure 3.4.

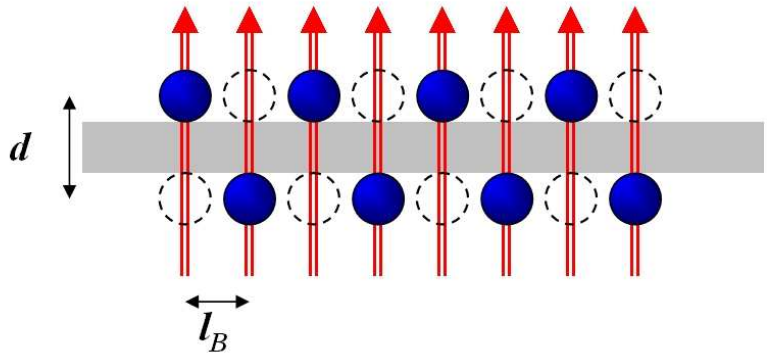

Figure 3.4: A bilayer system in the Halperin ground state, where a flux quantum (red arrows) is attached to each electron (blue filled circles). The dashed empty circles indicate positions in real space that are not occupied by electrons.

At the single layer filling factor 1/2 there are twice as many flux quanta/vortices as electrons in each layer. The Coulomb energy favors a state in which each electron is attached to one flux quantum, regardless in which layer the electron resides[5]. As in the fractional quantum Hall effect, the vortices are complex zeros of the wave function so the electrons strongly avoid one another, independent of whether they are in the same or opposite layers. *Because every electron sees a vortex attached to every other electron, the wave function in equation 3.1 is equivalent to a wave function of a single layer with a completely filled lowest Landau level. Owing to this equivalence, equation 3.1 is thus completely independent of which of the two layers a particular electron is in [Gir2002].*

The ground state may be written in a different form [Fer1989]

$$|\Psi\rangle = \prod_k (a c^\dagger_{k,\uparrow} + b c^\dagger_{k,\downarrow})|0\rangle \tag{3.2}$$

which means that $c^\dagger_{k,\uparrow/\downarrow}$ creates an electron in the upper/lower layer from the vacuum state $|0\rangle$. The index k is a momentum/wave vector index. The normalization factors $|a|^2 = |b|^2 = 1/2$ guarantee that each layer is half-filled. Using a particle-hole transformation $d^\dagger_{-k,\uparrow} \equiv c_{k,\uparrow}$, the wave function can be rewritten to a BCS-type wave function [Fer1989]

$$|\Psi\rangle = \prod_k (a + b c^\dagger_{k,\downarrow} d^\dagger_{-k,\uparrow})(\prod_k c^\dagger_{k,\uparrow}|0\rangle). \tag{3.3}$$

The operators $c^\dagger_{k,\downarrow} d^\dagger_{-k,\uparrow}$ create electron-hole pairs, and the wave function of equation 3.3 may be viewed as that of a Bose condensate of excitons in their lowest energy state [Fer1989, Paq1985]. These bilayer excitons are Bosons and have the same net $k = 0$ momentum (the electrons and hole momentum vectors are equal but opposite in direction). They have a vanishing charge-density at every point in space. These charge-neutral objects are indifferent to the Lorentz force induced by the magnetic field and should not suffer any Aharonov-Bohm phase shift which is proportional to the charge[6]. Even though bilayer excitons are charge-neutral, there is still a weak net interaction due to intralayer interactions between electrons which is stronger than the interlayer ones. As Figure 3.4 suggests, the particle-hole transformation means that each electron in one layer is coupled to the "vacant correlation space" (or hole) directly opposite to it in the adjacent layer forming an *interlayer exciton.*

[5]The 1's in equation 3.1 refer to the number of attached flux quanta.

[6]However, the experimental demonstration of Aharonov-Bohm oscillations in a bilayer sample would be able to definitely demonstrate long range quantum coherence.

Using $a = b = \frac{1}{\sqrt{2}}$, each factor $\frac{1}{\sqrt{2}}(c^\dagger_{k,\uparrow} + c^\dagger_{k,\downarrow})$ in equation 3.2 creates an electron with a pseudo-spin (degree of freedom) of $|\rightarrow\rangle = \frac{1}{\sqrt{2}}(|\uparrow\rangle + e^{i\varphi} \cdot |\downarrow\rangle)$, i.e., *each electron is in a coherent superposition of both layers.* Owing to this coherence, an electron can be destroyed in one layer and (re)created in the other layer without changing the ground state. Thus, the wave function 3.2 consists of a spatial part independent of the layer index and a pseudo-spin part [Gir2002]

$$|\Psi\rangle \propto \prod_{i<j}^{N\downarrow+N\uparrow} (z_i - z_j) \otimes \prod_{j}^{N\downarrow+N\uparrow} (|\uparrow\rangle_j + e^{i\varphi}|\downarrow\rangle_j). \tag{3.4}$$

When the total number of electrons is conserved while $N\uparrow = N\downarrow$, then the resulting coherent pseudo-spin vector has no z-component so there is a net polarization in the xy pseudo-spin plane as shown in Figure 3.5 a). While this easy-plane pseudo-spin magnetization can point in *any* direction, tunneling will orient the polarization along the x-axis [Mur1994], because the symmetric (eigen) state for the double quantum well with a finite $\Delta_{S,AS}$ is $\propto |\uparrow\rangle + |\downarrow\rangle$. In the absence of tunneling, however, the electrons have no way of telling the phase angle φ. This is a spontaneous breaking of the global symmetry (which is a planar rotational symmetry), where the system exhibits a degeneracy in φ, i.e., $0 < \varphi < 2\pi$, so the ground state energy does not depend on the pseudo-spin orientation[7].

Hence, at a total filling factor of one all pseudo-spins in the bilayer tend to align along an arbitrary direction given by φ owing to exchange interactions, resulting in an excitation gap. *The bilayer system at $\nu_{tot} = 1$ can (equivalently) be viewed as an easy-plane (quantum Hall) pseudo-spin ferromagnet [Jog2000].* If the electron densities are imbalanced (total number of electrons is still conserved), the pseudo-spin vector will have a finite z-component $\langle S_z\rangle \propto |a|^2 - |b|^2$ and will point out of the plane under an angle Θ (Figure 3.5 b)).

The Halperin (111) ground state, the Bose-Einstein condensate of excitons and the pseudo-spin representation are equivalent descriptions of the bilayer system at a total filling factor of one.

3.4 Exciton Superfluidity

As shown, the bilayer system can be described in terms of a 2-dimensional (2D) *pseudo-spin ferromagnet.* The Mermin-Wagner-Hohenberg theorem [Mer1966, Hoh1967] states that any finite 2D system at finite temperature with a continuous symmetry prohibits the possibility of spontaneous long-range order (or spontaneous symmetry breaking), owing

[7] For $d = 0$, the interactions are pseudo-spin independent, thus for small d/l_B this wave function is believed to be a good estimate for the ground state energy [Fer1989].

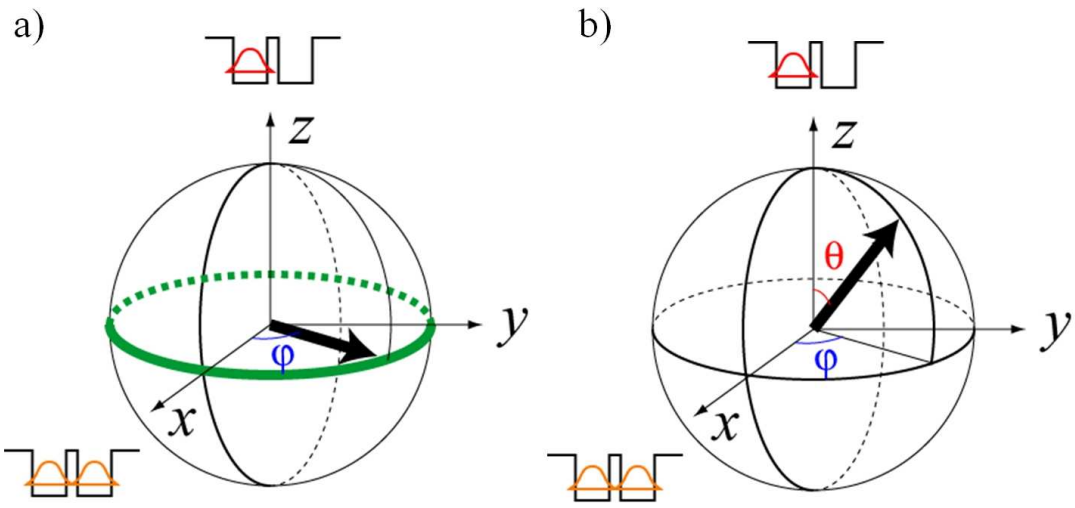

Figure 3.5: a) In the balanced case, i.e., when $N\uparrow = N\downarrow$, the pseudo-spin vector has no z-component and lies in the xy plane. b) in the imbalanced case, there is a surplus of carriers in one layer, and the pseudo-spin vector points out of the plane with an angle Θ. Figure from [Mra2008].

to phase fluctuations which are energetically favored and thus become more important. These low-energy fluctuations or pseudo-spin waves are called Goldstone modes. They are linearly[8] dispersing collective modes which are associated with a spatial gradient in the phase (see inset in Figure 3.6). Goldstone modes of the ground state are the smallest excitation of the ground state at $\nu_{tot} = 1$ and mean a *very slow change* of the phase φ from one electron to the next. It is thus a *very long wavelength*, and since the change occurs very gradually the energy is virtually zero. Goldstone modes of the ground state are therefore gapless in the long wave length limit (momentum $k \longrightarrow 0$) as shown in Figure 3.6 which also illustrates the dispersion relation for a two-layer system. The Goldstone mode is essentially an oscillation of the electron density in the bilayer where the electrons move back and forth out of phase with one another. The condensate state also possesses properties similar to superfluidity, which is associated with the gradient of the phase-variable as well. The order parameter, which is a measure for the symmetry of the system is [Gir2002]

$$\langle c^{\dagger}_{k,\uparrow} c_{k,\downarrow} \rangle \propto e^{i\varphi(\mathbf{r})}. \tag{3.5}$$

This order parameter is *charge-neutral*, so it can condense despite the presence of a

[8] In fact, for $d = 0$, the ground state is a broken-symmetry state and a Goldstone mode is expected with the dispersion $\propto k^2$. However, for small d a symmetry-breaking term is added which can be treated as a small pertubation which leads to a *linear* behavior at small k (see [Fer1989]).

magnetic field, unlike Cooper pairs where vortices would form. The symmetry is thus broken spontaneously, if φ is different from zero. If tunneling occurs, the order parameter is zero, because the pseudo-spin vector aligns along the x-axis. Superflow arises whenever the condensate phase $\varphi(\mathbf{r})$ varies in space (like for superfluid Helium). As previously mentioned, the energy does not depend on φ, however, it can depend on spatial gradients $H \propto \rho_s \int d\mathbf{r} |\nabla\varphi(\mathbf{r})|^2$, where ρ_s is the pseudo-spin stiffness which represents costs of energy to turn a pseudo-spin out of perfect alignment when $\varphi(\mathbf{r})$ varies with position. Note that an imbalance will require to introduce a capacitive term due to a charging energy of the bilayer which is proportional to the z-component of the pseudo-spin vector. The gradient energy is stored in an exciton *supercurrent* [Gir2002]

$$J_- = \rho_s \nabla\varphi(\mathbf{r}). \tag{3.6}$$

The charge conjugate to φ is the z-component of the pseudo-spin which is the *charge-difference between the two layers.* Hence, *the supercurrent corresponds to oppositely directed charge currents in the two layers.* This will become clearer in the experimental chapter 5.

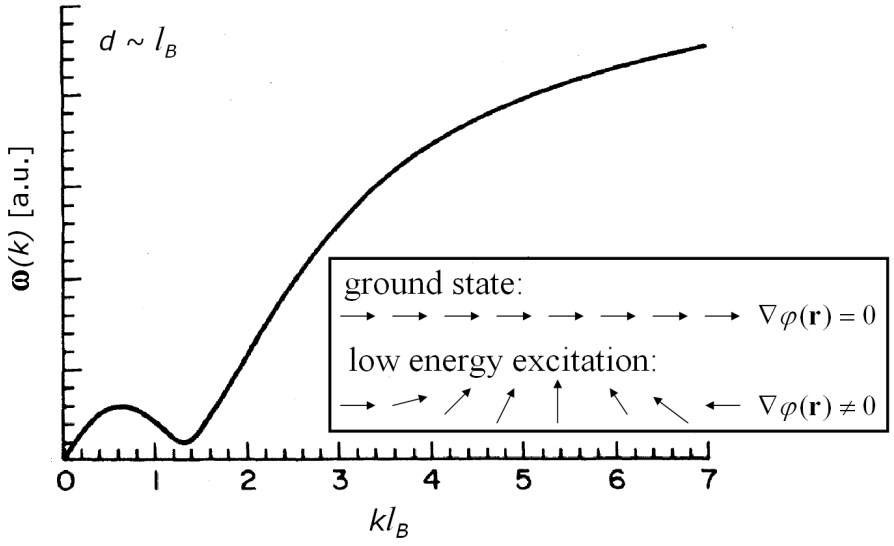

Figure 3.6: Dispersion relation for a bilayer system when the layer separation d is comparable to the magnetic length l_B. For small momenta k the dispersion relation vanishes linearly. At $kl_B \sim 1$ the dispersion relation shows a dip (roton part, like in superfluid Helium) which indicates that the system undergoes a phase-transition (after [Fer1989]). The inset shows the pseudo-spin field in the ground state which is aligned along a common direction given by the phase φ. Spin-waves (Goldstone modes) are low energy excitations (and favored to direct spin-flips).

For small k the dispersion relation for a bilayer system in Figure 3.6 increases linearly like for a weakly interacting Bose gas such as superfluid Helium. In bilayer systems, the electron-electron interaction within a layer is usually stronger than the interlayer-interaction leading to a net weak repulsive interaction between the excitons. In terms of the pseudo-spin language this means that the Coulomb interaction is spin-dependent (unlike for real spins, where the Coulomb interaction is spin-invariant). The quantum Hall gap is related to an electron-hole charged excitation with a large wave vector k (i.e., short wave length), so the quantum Hall effect itself is preserved even in the absence of long-range order.

Tunneling spectroscopy experiments were able to demonstrate long-range pseudo-spin order and the existence of Goldstone modes through the response to weak parallel, i.e., in-plane, magnetic fields. Tunneling experiments will be discussed in detail in chapter 6, it however should already be noted that they exhibit a large zero bias anomaly that resembles the one of the Josephson effect of superconductivity.

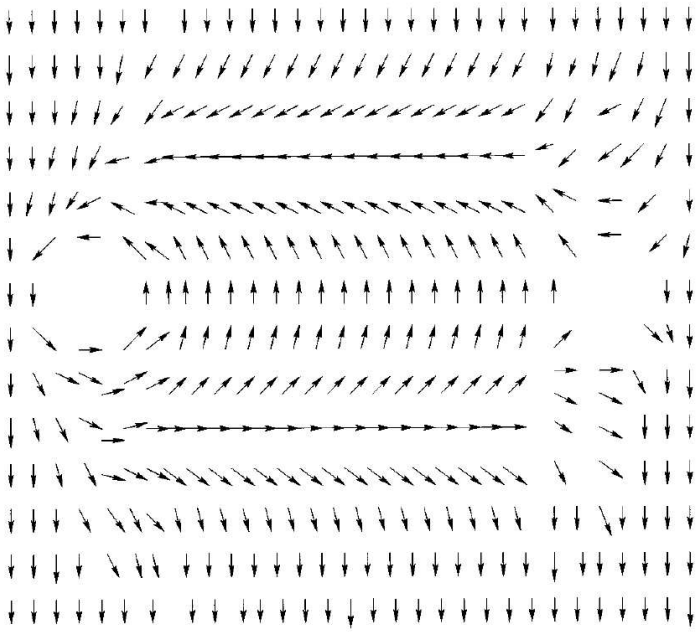

Figure 3.7: Meron pair, which is formed by local pseudo-spin re-orientation, is connected by "domain walls". From [Gir2000].

Interacting 2D spin systems are not expected to possess a normal second order phase transition. They instead undergo at a nonzero critical temperature a true thermodynamic phase transition (i.e., a "condensation"), known as the Kosterlitz-Thouless (KT) [Kos1973] transition. Below the critical temperature, the system shows "intermediate"

long-range order over a finite distance which are the result of topological defects, i.e., vortices in the pseudo-spin field called *merons* [Moo1995]. The existence of a vortex will disturb the phase with an energetic cost that is proportional to the gradient of the order parameter $\varphi(\mathbf{r})$. Consequently, it is energetically favorable to have a binding of vortices with opposite vorticity in order to "localize" the disturbance in the pseudo-spin field (Figure 3.7). Because each vortex correspond to the pseudo-spin vector locally pointing out of plane, one half of an extra electron (or hole) resides in each defect, i.e., each vortex carries a charge of $\frac{e}{2}$ [Gir2000]. The KT phase transition, which should occur at a temperature of the order of the spin-stiffness $\rho_s \sim 0.5$ K [Gir2000], is of topological nature, where vortex excitations (vortex unbinding with a gain in entropy) occur as the temperature increases.

Generally, exciton condensation has two limits. In the low density limit, excitons will already exist above the critical temperature T_C, i.e., their number does not change with T. The critical temperature in this limit is only determined by the statistical distribution in momentum space of weakly interacting bosons. On the other hand, in the high density limit, the critical temperature for condensation is reached when excitons begin to form (like Cooper pairing in the BCS theory). The condensation can exhibit a mixed nature for intermediate densities [But2004, Kel1965, Kel1968]. For typical electron densities ($n \sim 2.3 \cdot 10^{14}$ m^{-2}) at $\nu_{tot} = 1$, the exciton density can be estimated to be $a_B^2 n \approx 0.2$ (0.5*), where a_B is the exciton's Bohr radius. Naively a_B is the *center-to-center* layer separation (i.e., $a_B = d \approx$ 29 nm) but more precisely it has to include the magnetic length $l_B \approx$ 18 nm (for 2 T) since the electrons perform cyclotron orbits, i.e., $a_B = \sqrt{(2l_B)^2 + d^2} \approx 46$ nm (yields value marked with *). Even though the spacing between the excitons is comparable to the exciton Bohr radius which might suggest that the system forms a BCS-like state [Sno2002], the pairing in the excitonic state in bilayers is due to the Coulomb interactions at low densities giving it BEC characteristic.

"Superfluidity" and "superconductivity" are closely related phenomena and refer to a macroscopic state of matter, where the probability of finding one of its constituents is uniform over the entire region where the phenomenon occurs. The state can thus be described by a single wave function which exhibits coherence over macroscopic length scales. Objects which show this macroscopic phase transition always undergo a Bose condensation. These objects are either Boson particle "by nature" or they couple-up by *phonon-interaction* in the case of Cooper pairs or *Coulomb interactions* for bilayer excitons so that Bose statistics apply. Conceptionally, superconductors are also superfluids. However, in a superconductor the "fluid" is made of electrons which conduct electricity and not material atoms/molecules as in superfluid Helium for instance. While there are certain similarities

between the excitonic state in bilayers and superfluidity/superconductivity, there is no Meissner effect, i.e., the magnetic field still penetrates the bilayer (it needs to!). Also, interlayer tunneling experiments which show a Josephson-like effect are not tunneling between two superconductors but between two electron layers which only as a whole form a correlated state. So far, no long range quantum coherence has been demonstrated in experiment.

3.5 Wigner Crystallization?

At a filling factor of 1/2 (or below) and when the density is low enough, the Coulomb energies dominate and the electrons can assume a configuration which is believed to be a regular (pinned) lattice called *Wigner crystal (WC)* [Wig1934]. Such WC phases have been considered to be occurring at a total filling of one to be competing with the Bose condensate of excitons at intermediate layer separation [Che2006, Jog2006, Cot1992]. However, the appearance of a quantized Hall voltage at total filling factor 1 strongly questions its importance for the $\nu_{tot} = 1$ quantum Hall state. Yet, at sufficiently small ν_{tot}, the bilayer ground state is expected to be a pure bilayer WC. In real samples, a WC can be pinned by disorder. If the electrons coherently belong to both layer then the WC of each layer is effectively pinned by the joint disorder [Che2006]. This bilayer WC should be insulating but would exhibit a sharp interlayer tunneling conductance peak at low temperatures due to the interlayer phase coherence [Vei2002, Jog2006]. For large d/l_B two staggered WCs (due to minimization of interlayer Coulomb interaction) without interlayer coherence can exist.

Chapter 4

Equipment and Samples

The following chapter is divided into four main sections that will be used as an introduction to the experiments. Parts 1 and 2 will deliver a brief review of earlier experiments and the motivation for this experimental work. The third part will give details on the sample/crystal structure and the techniques of sample preparation. The last part will give a physical (less technical) description of the cryogenic concept which is necessary to reach sufficiently low temperatures in order to observe the $\nu_{tot} = 1$ state and give an overview over the experimental setup.

4.1 Review and Motivation

Interlayer drag measurements on Hall bars, which are performed by passing a current through one of the two layers (called *drive layer*) and measuring the voltage drop across the adjacent layer (called *drag layer*), have shown that at $\nu_{tot} = 1$ the Hall drive and drag voltages are quantized to h/e^2. At the same time, a longitudinal drag voltage is observable [Kel2002, Wie2005]. This quantized drag resistance was predicted by theory and is believed to be a direct signature of the Bose condensation of interlayer excitons [Yan1998, Zho1999, Yan2001] and the boundary condition of the drag experiment (which will be discussed in chapter 5). If the configuration is slightly changed by passing two equal but oppositely directed currents through both layers (*a counter-flow measurement*), it is found that both ρ_{xy} and ρ_{xx} tend to zero [Tut2004, Kel2004, Wie2005], as shown in Figure 4.1. Here, the boundary conditions allow the current to be completely carried by interlayer excitons which are charge-neutral and are thus unaffected by the presence of a magnetic field, i.e., the Hall voltage vanishes because excitons do not feel a Lorentz force.

While the vanishing of both resistivity components at a total filling factor of one suggests that the bilayer may indeed be a superconductor exhibiting a dissipationless exciton current, such a direct comparison is invalid. Owing to the dimensionality and

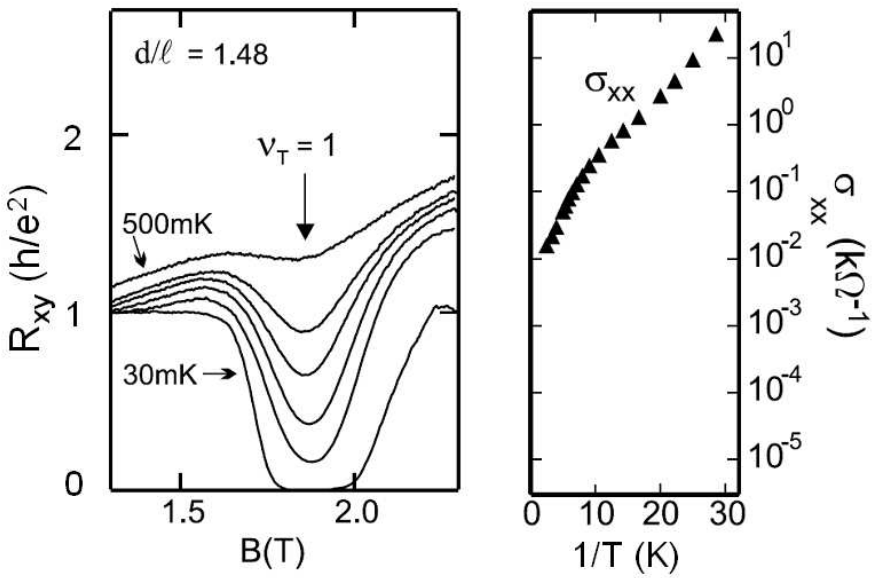

Figure 4.1: Counterflow measurements on a Hall bar. Left hand side: Hall resistance in the vicinity of $\nu_{tot} = 1$ for several temperatures. For lowest temperatures, $R_{xy} \to 0\ \Omega$. Right hand side: the calculated conductivity σ_{xx} which appears to become very large for lowest temperatures. The longitudinal resistivity, which also vanishes for $T \to 0$ K, is not shown. Plots are taken from [Kel2004].

the magnetic field, the *bulk conductivity* of a 2DES is only accessible by inverting the resistivity tensor as

$$\sigma_{xx} = \frac{\rho_{xx}}{\rho_{xx}^2 + \rho_{xy}^2}. \tag{4.1}$$

If (only) $\rho_{xx} \to 0$ then also $\sigma_{xx} \to 0$ as long as $\rho_{xy} \neq 0$. But when both resistivity components tend towards zero, this would suggest $\sigma_{xx} \to \infty$. This calculation is however formally difficult as both values become infinitesimal small, also because residual resistivities may depend on disorder [Hus2005] or other intermixed states without interlayer phase coherence [Dem2001]. Nevertheless, as temperature-dependent measurements indicate (see Figure 4.1), σ_{xx} could become very large as the temperature approaches absolute zero. Yet, the computability is not the only issue. It was suggested [Mac0708] that the vanishing of both components could rather be the result of the formation of (excitonic) edge channels which intrinsically provide dissipationless transport owing to a suppression of backscattering. By using a ring geometry instead of a Hall bar, both problems can be circumvented.

4.2 The (Quasi-)Corbino Geometry

An *ideal* Corbino ring as shown in Figure 2.2 is (usually) an annulus where the entire inner area constitutes one Ohmic contact (source) and the entire outer edge is connected to another Ohmic contact (drain). However, since an ideal Corbino ring configuration does not allow independent contacts to both layers of a double quantum well system, the ring has to be modified into a *quasi*-Corbino geometry as depicted in Figure 4.2. By using a gate technique, two independent quasi-Corbino rings can be obtained with three contacts to the outer and two contacts to the inner perimeter.

Since the ring symmetry prevents an electric field in the azimuthal direction under isotropic conditions, i.e., $E_\phi = 0$, there is no contribution to the measured conductivity from off-diagonal tensor components. So, by applying a constant potential difference V between source and drain, and measuring the current I that flows through the bulk, the (diagonal) conductivity $\sigma_{xx} = A \cdot I/V$, where A is a geometrical factor, can be calculated directly. The Corbino ring is therefore complementary to the Hall bar which directly yields the components of the resistivity tensor ρ_{xx} and ρ_{xy}. Even though edge channels will form around the inner and outer circumference in this geometry as well, they are, however, completely separated by the bulk, i.e., a Corbino ring provides an entirely edge channel free transport from source to drain.

If no magnetic field is applied, the electron transport is purely radial between source and drain. As the magnetic field B is increased from zero, Lorentz forces will bend the electron trajectory into a spiral and drive the electrons multiple times around the annulus before reaching the drain. When the magnetic field is strong enough to exhibit Landau Level quantization, the Fermi energy will eventually lie in the mobility gap, while edge channels form around the inner and outer perimeters of the ring. In this incompressible regime that occurs at all integer filling factors, the electron motion is purely orbital which leads to a vanishing radial current between source and drain. While the Fermi energy moves through extended (compressible regimes) and localized states (incompressible regimes) when B is varied, the electron motion repeatedly enter regimes of spiral and orbital nature with a $1/B$ periodicity. The total current thus consists of a radial and an azimuthal part which oscillate anti-cyclically as a function of the magnetic field, i.e., in a quantum Hall regime the radial fraction which is accessible by experiment is zero while the azimuthal (orbital) part is maximal. A finite element analysis and solver software package (Comsol Multiphysics) was used to simulate the potential and current distribution in this geometry. The simulation assumes non-vanishing diagonal components of the conductivity tensor,

$$\widehat{\sigma} = \begin{pmatrix} \sigma_{xx} & -\sigma_{xy} \\ \sigma_{xy} & \sigma_{xx}, \end{pmatrix}, \tag{4.2}$$

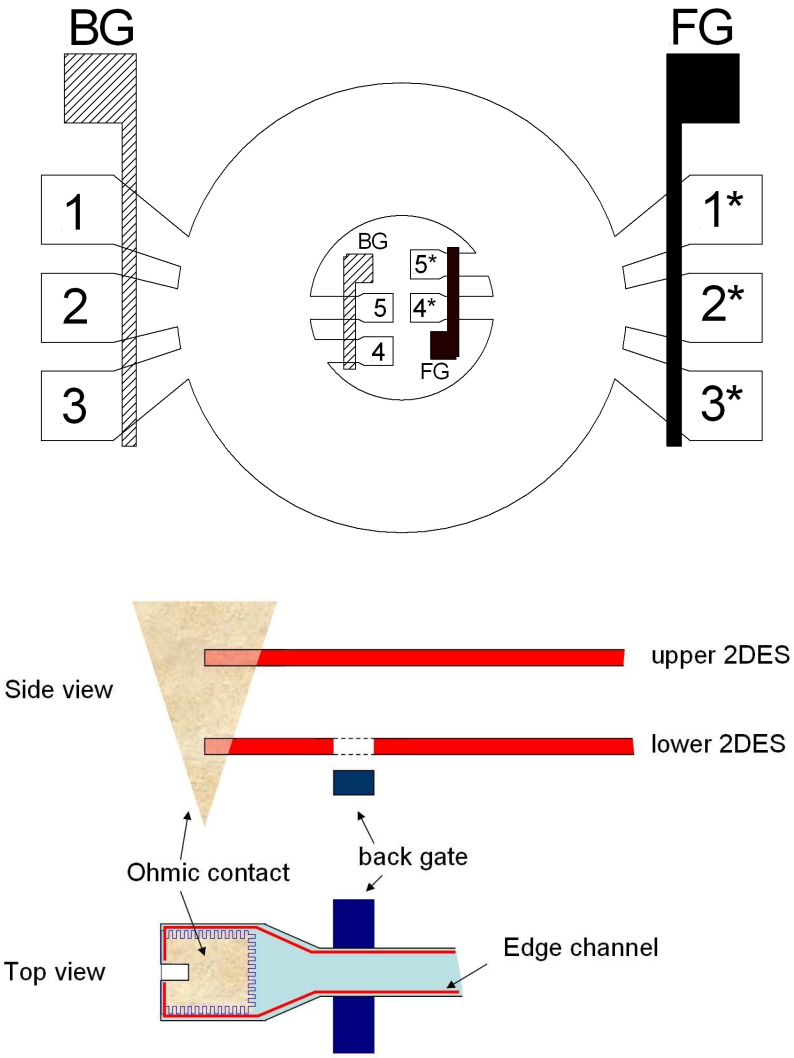

Figure 4.2: Top panel: schematic view of the Corbino geometry used in this experiment. Application of appropriate voltages to the back gates (marked as "BG") and front gates ("FG") will lead to contact separation, i.e., the Ohmic contacts 1 through 5 will connect to the upper quantum well and 1* through 5* to the lower one. Bottom panel: selective depletion technique after [Eis1990b]. An appropriate voltage to a back gate (or front gate) will depopulate the nearest 2DES in the vicinity of the gate. The tooth pattern will improve electrical contact, and the rectangular recess at the head-side will assure that contact is provided even with poor lithography (see text for details).

with $\sigma_{xx} = \cos(\theta_H)$ and $\sigma_{xy} = \sin(\theta_H)$, using the definition of the Hall angle θ_H, i.e., $\tan(\theta_H) = \frac{sin(\theta_H)}{cos(\theta_H)}$. Figure 4.3 shows a sequence of potential and current density distributions for several values of the Hall angle for a single ring including the contacts. At a Hall angle of (nearly) 90 degrees, the ring becomes incompressible.

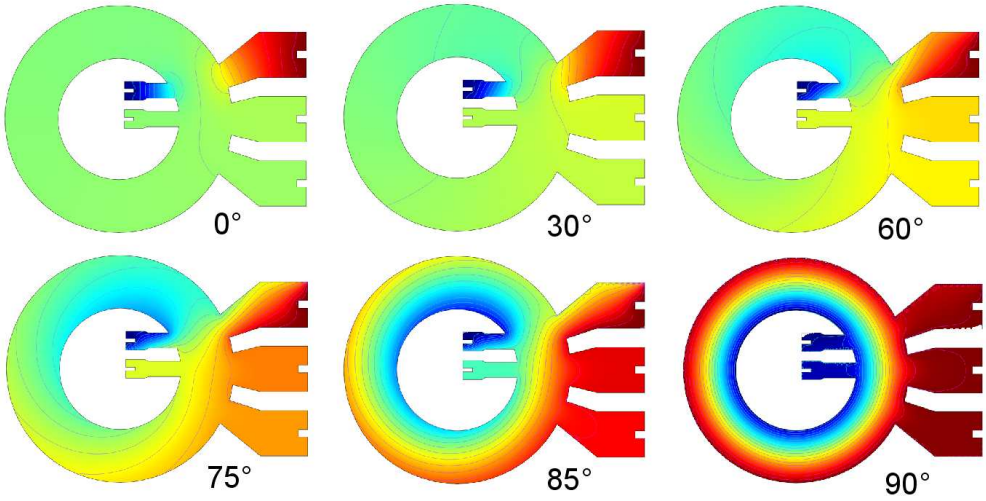

Figure 4.3: Sequence of the potential distributions for six different Hall angles. The colors mark equipotential lines, with blue being a predefined ground potential and red an arbitrary potential voltage.

With the drag experiments in chapter 5, it will be demonstrated that voltages of equal amplitude can be observed at a total filling factor of one under sufficient coupling conditions. Since the contact pairs which probe the voltages of drive and drag layer are located at opposite sample edges, the question is under which circumstances such identical potential distribution can exist. Figure 4.4 thus plots the ratios of the expected voltages probed at opposite perimeters of the sample (like in a drag experiment) versus the Hall angle. It is found that equal voltages should only be assumed for a Hall angle closest to 90 degrees.

4.3 Samples Structure and Preparation

The entire crystal structure is grown using the MBE technique and starts with a 100 nm highly Si-doped GaAs layer[1]. Ex-situ photolithography and wet chemical etching are ap-

[1]The heavy doping will lead to quasi-metallic conductance at low temperatures (degenerate conduction).

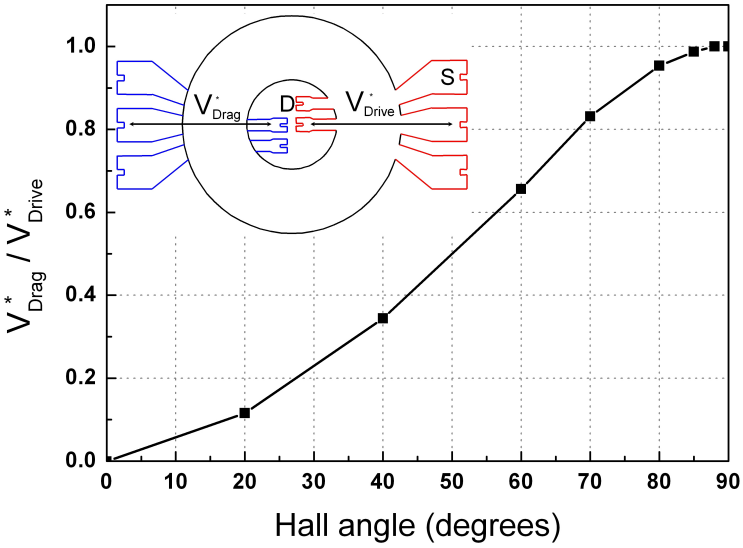

Figure 4.4: Analysis of the ratio of the theoretically expected drive and drag voltages versus the Hall angle. The inset is a top view onto the Corbino ring and illustrates where the voltages are probed. The colors red and blue mark the Ohmic contacts to the top and bottom layer. Identical voltages should only be observable for Hall angles exceeding 85 degrees.

plied to define back gates. The wafer is cleaned using the FFP technique developed by Fronius, Fischer and Ploog [Fro1986] which will remove contaminations and generate a protective surface oxide. It is re-introduced into the MBE machine for the overgrowth of the remaining bilayer structure on top of the back gates. This overgrown-back-gate method was developed by Rubel *et al.* [Rub1997] to exploit the selective depletion technique engineered by Eisenstein *et al.* [Eis1990b] as explained later on. The double quantum well structure is sandwiched between several hundred nm of isolating buffer layers. The complete crystal structure can be found in the appendix. The 9.6 nm wide barrier consists of a superlattice of alternating layers of AlAs (1.70 nm) and GaAs (0.28 nm) which is used to improve the electron mobility. The electrons inside the quantum wells originate from volume-doped Si regions 300 nm above/below the upper/lower quantum well. The donor atoms energetically pull the conduction band towards the Fermi energy E_F. This will pull the quantum well conduction bands below E_F, leading to an electron population at low temperatures.

The details of the double quantum well structure and the doping are fairly relevant for the physics of the $\nu_{tot} = 1$ state. While the center-to-center separation d is a fixed value given by the epitaxy process, l_B scales directly with the magnetic field which can be manipulated in the experiment. As pointed out in chapter 3, to observe interlayer

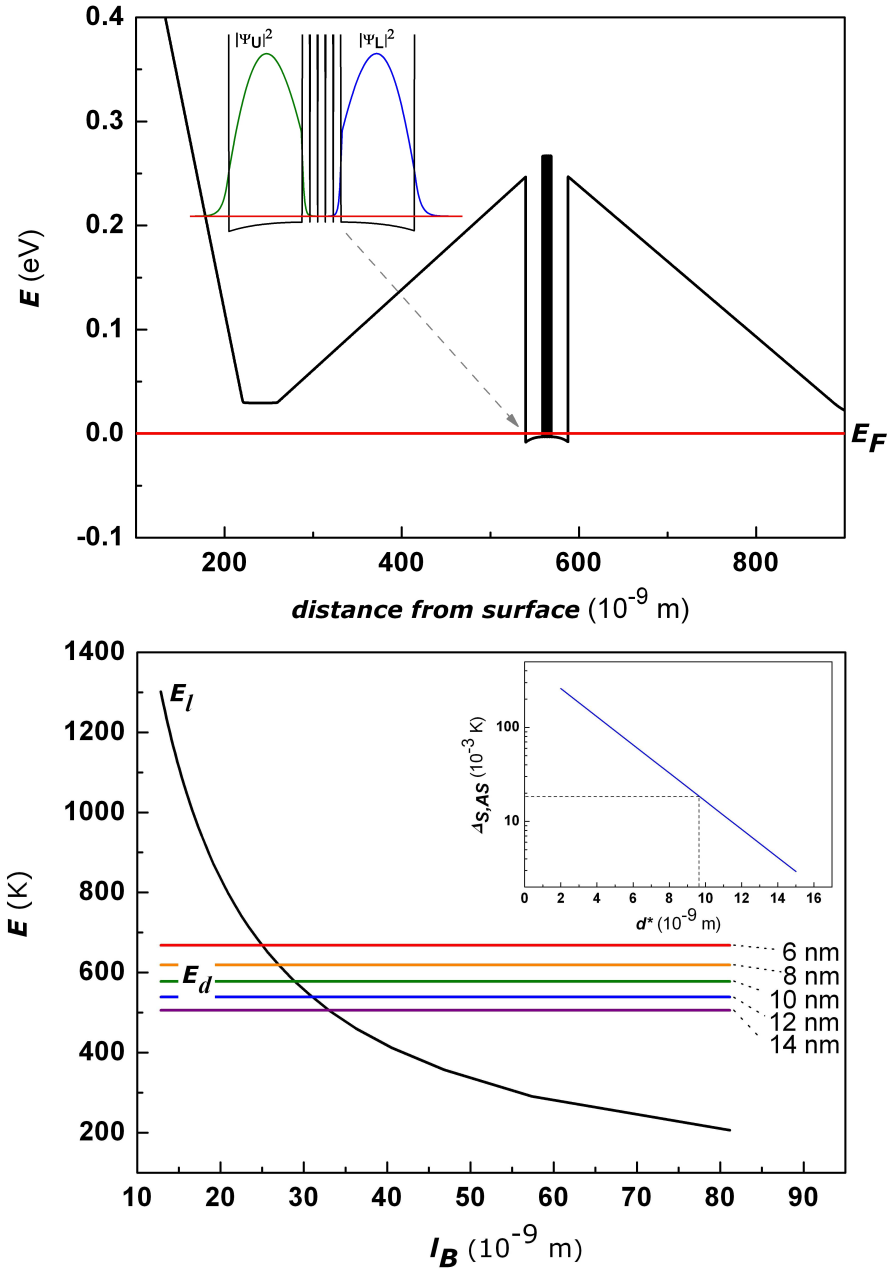

Figure 4.5: Top panel: band structure calculated with a Poisson solver as a function of the distance from the surface. Bottom panel: Coulomb energies for interlayer E_d and intralayer E_l interactions plotted versus the magnetic length (which is $\propto B^{-0.5}$) for a set of five different barrier widths $d^* \in \{6,\ 8,\ 10,\ 12,\ 14\}$ in $10^{-9}\ m$. Note that while the energies are plotted versus d^*, the energies were calculated with the center-to-center separation, i.e., $d^* = d - t_{QW}$, with t_{QW} as the quantum well width. Inset: with the barrier height from the top panel, the tunnel splitting $\Delta_{S,AS}$ was *estimated* with equation 4.3. As this estimate shows, the Coulomb energies are many orders of magnitude larger than the tunnel splitting. The dashed line shows the splitting energy for the double quantum well structure used in this thesis.

correlation effects, d/l_B must be smaller than 2. Since $l_B \propto B^{-0.5}$ and $\nu \propto n_e/B$ (see equation 2.12), the 2DES should have low densities n_e. Large *intrinsic* densities are not preferable as they require also a large gate voltage to reduce n_e to reach the required value of d/l_B.

The top panel of Figure 4.5 shows the band diagram for the a (19/9.6/19) nm double quantum well structure which was calculated with a a simple Poisson solver[2]. The estimated quantum well densities of $(5.0/4.7) \cdot 10^{10}$ cm^{-2} for the upper/lower quantum well agree within (10-15) % with the experimental data. With the calculated barrier height, the tunnel splitting can roughly be estimated assuming parabolic quantum Wells (and barrier) [Ens2000]

$$\Delta_{S,AS} \approx 2E_1 e^{-\frac{d}{2\hbar}\sqrt{2m^*V}}, \tag{4.3}$$

where $m^* = 0.067m_e$ is the effective electron mass in GaAs, $V = 0.27$ eV the calculated barrier height and $E_1 = 180$ K the energy of the lowest sub-band of a quantum well with width 19 nm (see equation 2.9). Since it is very difficult to prevent tunneling between the layers entirely when the two layers are close enough to exhibit interlayer phase coherence, real samples usually are *weakly* tunneling with a small estimated $\Delta_{S,AS}$ of the order $(100 \ldots 200)$ μK [Spi2000, Kel2004]. The bottom panel of Figure 4.5 compares the intralayer Coulomb energy E_l with the interlayer Coulomb energies E_d for five different barrier widths (which are constant in B or l_B), both independent of the particular shape of the barrier. These Coulomb energies are many orders of magnitude larger than the single tunneling splitting which was estimated with equation 4.3. Note that a) the simple 1D Poisson solver did not provide the required solution to obtain $\Delta_{S,AS}$ directly, and b) that this estimate of $\Delta_{S,AS}$ for a 9.6 nm barrier is about 130 times larger than the one obtained with a professional Poisson solver, as given in chapter 3. However, equation 4.3 assumes a barrier of different shape, which will largely effect the value of $\Delta_{S,AS}$.

The two sample structures used in this work are a ring geometry (see later for details) and a standard Hall bar (refer to [Wie2005]) which were defined by photolithography with a chromium on quartz mask and then wet chemically etched. Electrical contact to the two quantum wells is realized by evaporating 3216 Å gold, 1584 Å germanium, and 600 Å nickel onto the sample after contact regions where defined by photolithography and slightly wet chemically etched to reduce the distance to the two 2DESs and to remove surface oxides. When the sample is annealed[3] to 440 °C under a H_2/N_2 forming gas atmo-

[2] 1D Poisson/Schrödinger Band Diagram Calculator by Greg Snider [Sni2008].

[3] For the given concentration, Au and Ge form an eutectic alloy where both components simultaneously harden into a solid at a specific temperature. Ni is used as a diffusion enhancer.

sphere, the metals will diffuse into the structure connecting both 2DES *simultaneously*, i.e., each Ohmic contact will have electrical contact to both layers. However, to provide *independent* contact the layers, the overgrown back gates and additional front gates are used which cross the contact arm as shown in Figure 4.2. The front gates are produced by evaporating 50-100 $\mathring{A}$ of chromium as adhesive layer followed by 1250 $\mathring{A}$ of gold onto photolithographically defined areas on top of the crystal. When a sufficient negative voltage is applied to one of the gates, the 2DES in its vicinity will be depleted by the field effect. The voltage has to be large enough to completely cut off the nearby 2DES but has to remain small enough to not affect the other 2DES. The latter is usually screened by the 2DES nearest to the gate. This method is called selective depletion technique [Eis1990b].

The regions for the Ohmic contacts exhibit a "tooth pattern" as shown in Figure 4.2 owing to a dependence of the conductance on the crystal direction, i.e., the tooth pattern will provide interfaces for the [011] and [01$\underline{1}$] crystal direction. In the Landauer-Büttiker picture [Bue1988, Mue1990], the edge channels are injected into/reflected out of the Ohmic contacts. For that reason the contacts possess a rectangular recess at their head-sides which will assure that the edge channels run into the contact material even if the Ohmic area gets accidentally shifted inwards in the lithography process.

4.4 Cryogenics and Experimental Setup

Evaporation Cooling

Temperatures of approximately 1 K (using ^{4}He) or 0.25 K (using ^{3}He) can be achieved by reducing the pressure above the almost adiabatically confined liquid of either one of the two stable isotopes of Helium (evaporation cooling). The pumping process will remove high energy gas particles first, and to maintain an equilibrium state, particles with lower energy will undergo a transition into the gas phase. This will reduce the (mean) energy of the liquid and thus reduce its temperature. However, as T$\longrightarrow$ 0 K, the vapor pressure decreases exponentially as $\propto e^{-L/T}$ [Ens2000], where L is latent heat of evaporation which is *approximately* independent of the temperature for this range. Since pumps run with a constant pumping power, the mass flow across the phase boundary and consequently the cooling power will decrease exponentially with temperature (or with the vapor pressure). This limits the achievable temperature by evaporation cooling to 1 K (^{4}He)/0.25 K(^{3}He).

Dilution Refrigerator

A dilution refrigerator can provide continuous refrigeration to below 20 mK. The cooling principle is comparable to that of evaporation cooling, however, a dilution fridge exploits the quantum properties of a mixture of ^{3}He and ^{4}He which separate into two distinct phases at low temperatures as shown in Figure 4.6. ^{4}He has a nuclear/total spin of 0 and is thus a Boson. At low temperatures this Bose liquid of ^{4}He undergoes a Bose condensation in momentum space and becomes superfluid. After this transition, ^{4}He will act as an inert background (or vacuum) for the dissolved other isotope ^{3}He. ^{3}He, on the other hand, has a nuclear spin of 1/2 which makes it a Fermion that obeys the Pauli principle.

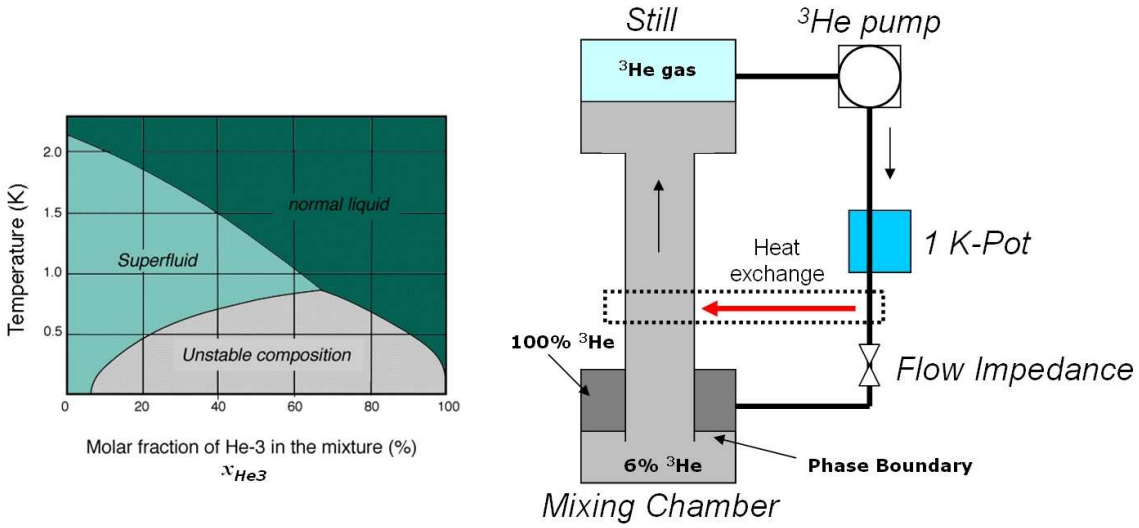

Figure 4.6: Left: phase diagram of a ^{3}He-^{4}He mixture (from [Cer2008]). Right: principle of a dilution fridge. Explanations in the text.

The phase diagram shows that at below approximately 0.9 K and a concentration of about 0.65, a phase separation takes place. The ^{3}He-rich phase is lighter which thus floats on top of the heavier ^{4}He-rich phase. As the diagram shows, even for T=0 K, both isotopes are not completely separated, there is instead a finite ^{3}He concentration of approximately 6 % in the ^{4}He-rich phase. The origin for this finite solubility which allows permanent cooling lies in the quantum properties of the mixture: since the ^{3}He atoms have a smaller mass, they have a larger zero point motion than the heavier ^{4}He atoms. Consequently, a ^{3}He atom can have a larger binding energy with a ^{4}He atom than with another ^{3}He atom, i.e., the effective binding energy in ^{4}He-rich phase is larger than in the ^{3}He-rich phase. If the temperature is low enough, the ^{3}He can be treated as a degenerate Fermi liquid, where the strength of interactions can be tuned by the concentration x_{He3}

of ^{3}He. The Fermi temperature T_F is defined by [Ens2000]

$$k_B T_F = E_F \propto x_{He3}^{2/3}, \tag{4.4}$$

where k_B is the Boltzman constant. This relation states that when more ^{3}He atoms are added, they will need to occupy states with larger and larger kinetic energy. At the same time the effective binding energy is lowered. At T=0 K and a concentration of about 6%, the binding energy and Fermi energy are identical and it is energetically favorable to have two distinct phases. Since there are fewer ^{3}He atoms the ^{4}He-rich than in the ^{3}He-rich phase, its Fermi energy is significantly lower. If E_F is smaller, the specific heat of this Fermi gas C_{He3},

$$C_{He3} \propto \frac{T}{T_F} \propto \frac{T}{x_{He3}^{2/3}}, \tag{4.5}$$

is larger. It depends linearly on the temperature and dominates over that for liquid ^{4}He with $C_{He4} \propto T^3$. The cooling power of the dilution refrigerator benefits from the large difference of the specific heats of the two phases owing to the different concentrations of ^{3}He. The cooling power can be calculated as proportional to [Ens2000]

$$\int_T \Delta C_{He3} dT \propto T^2 \tag{4.6}$$

and is thus more effective at low temperatures than evaporation cooling which vanishes exponentially with the temperature.

The dilution cycle is shown in Figure 4.6. The circulation is maintained by pumping on the *still* which is kept at approximately 0.7 K. Owing to the low vapor pressure of ^{4}He at this temperature, mainly ^{3}He is being pumped. After passing the external gas handling circuit (where the flow of the mixture can be controlled), the gas is sent through an *1-K Pot*[4] where it is pre-cooled. An impedance will increase the gas pressure to liquify the ^{3}He. In a multi-level heat exchange system, the liquified ^{3}He is further cooled and then reintroduced into the ^{3}He-rich phase (above the phase boundary) of the *mixing chamber*. The gas cycle is closed with the lines running from below the phase boundary up again to the *still*. Pumping ^{3}He from the ^{4}He-rich phase creates a gradient in the concentration so that ^{3}He atoms from the ^{3}He-rich phase pass the phase boundary which yields a cooling effect by "evaporation into the ^{4}He-rich phase". The sample that is being measured is located at the phase-boundary where this cooling effect is large, and where the magnetic field of the superconducting magnet can penetrate the 2DES perpendicularly. Not shown in the schematic diagram are the liquid ^{4}He and liquid nitrogen reservoirs (separated by a vacuum chamber) that enclose the dilution cycle to reduce thermal radiation.

[4]The 1-K Pot is cooled by evaporation cooling using liquid ^{4}He.

The Electron Temperature

The *base temperature* T_{base} is the lowest accessible temperature of the mixing chamber when it is in thermal equilibrium. Since the sample is in direct thermal contact with the mixture, T_{base} is close to the temperature of the crystal T_{sample}. The electron temperature T_e of the 2DES, however, is usually at a much higher temperatures than T_{base}. There are two different mechanisms for electrons to lose energy. Electrons can relax to lower temperatures via electron-phonon interaction. The cooling power is [Mit1996]

$$\propto \frac{A_{sample}}{\sqrt{n}}(T_e^5 - T_{sample}^5). \tag{4.7}$$

Below 1 K, this mechanism can be neglected but hot electrons can diffuse out to the cold Ohmic contacts and be replaced by cold electrons from the leads. The power flow by this mechanism is [Mit1996]

$$\propto \frac{1}{R_{2pt}}(T_e^2 - T_{sample}^2), \tag{4.8}$$

where R_{2pt} is the total resistance between two current contacts. Owing to these small cooling powers for the electrons, external sources can raise the electron temperature to above those of the crystal by coupling energy such as high frequency (HF) radiation into the system, either by the wiring or insufficient shielding.

Measurement Infrastructure

Low temperature measurements were performed with a Kelvinox TLM (top loading) system with a superconducting magnet (B_{max}=21.5 T). A cooling power of 600 μW provides temperatures of the mixing chamber of down to 12 mK, which was confirmed by nuclear thermometry on ^{60}Co. Alternatively, a ^{3}He system was used with a base temperature of approximately 0.25 K, where the sample was mounted on top of a cold finger.

Figure 4.7 shows a schematics of the experimental setup. A LabView-controlled computer is used for both data acquisition and controlling the power supply of the superconducting magnet. The computer is isolated from the GPIB network by a GPIB bus expander/isolator and from the serial RS232 cable that connects the magnet with an opto-bridge. All measurement equipment is isolated from the common AC power line by using isolation transformers. Pumping lines running into the cryostat are also electrically isolated from the pumps with non-conducting clamps and centering rings.

AC measurements were performed with Signal Recovery 5210 analog lock-in amplifiers which are connected to Keithley 2000 digital multimeters (DMM) for data acquisition. The internal oscillator of one lock-in provides the low frequency AC excitations voltage,

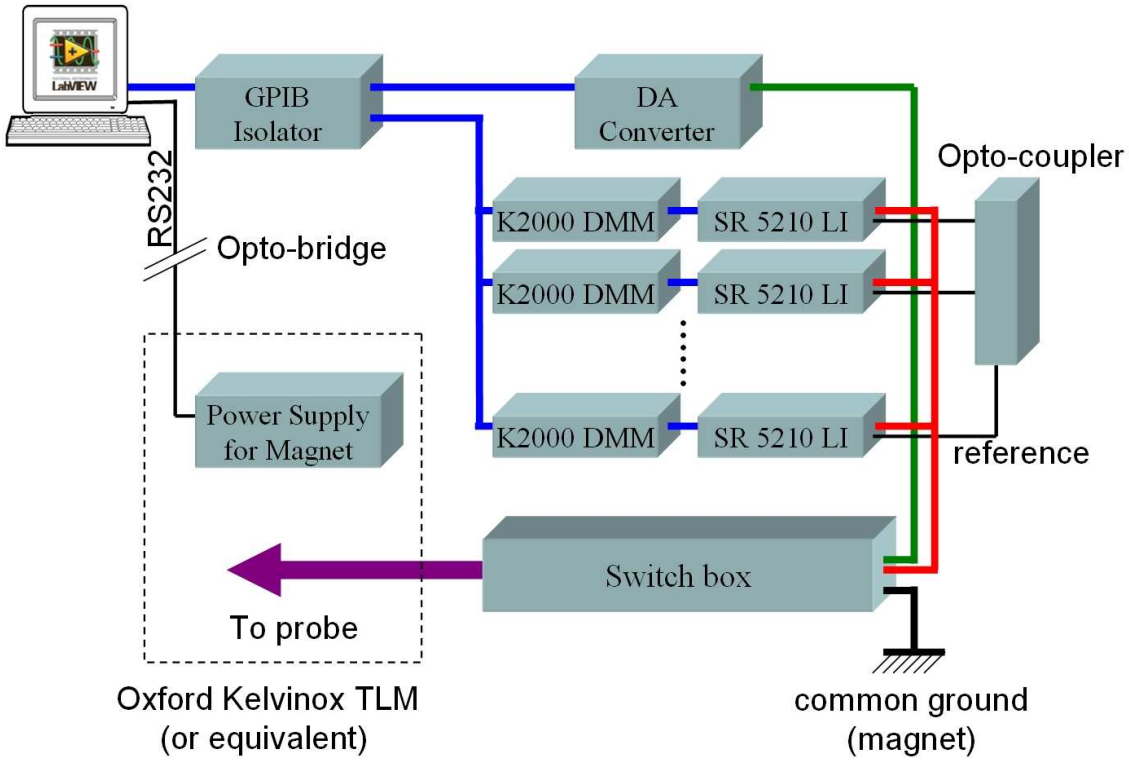

Figure 4.7: Schematics of the experimental setup. Experimental details can be found in the corresponding chapters. The digital-analog (DA) converter provide all DC voltages. AC measurements are performed with Stanford Research 5210 lock-in amplifiers (SR 5210 LI) connected to Keithley 2000 Digital Multimeters (K2000 DMM) which are read over the GPIB bus. The reference signal for the AC measurements is distributed with one/several opto-coupler/s.

and its reference signal is distributed with opto-couplers to avoid ground loops. All DC voltages (including gate voltages) were provided by an in-house built digital-analog (DA) converter with a voltage output range of ±10 V. For the DC measurements, the lock-ins were replaced by Stanford Research low noise preamplifiers SR560 (not shown in the diagram). The switch box is connected to the head of the probe via a doubly shielded cable (i.e., in addition to an outer shield, each individual wire is shielded as well).

While AC measurements allow a sensitive and straightforward detection of small voltages, problems with the phase of the lock-in can arise which are associated with capacitances (sample, cables, etc.) and the high resistances at large magnetic fields. Issues like these can be circumvented by doing DC measurements which however are more vulnerable to noise. Also, insufficient/loose wiring can lead to induced voltages in external magnetic fields, such as the terrestrial magnetic field or stray fields from the superconducting magnet.

Chapter 5

Interlayer Drag Measurements

5.1 Background: (Coulomb) Drag Experiments

*Intra*layer electron-electron Coulomb interactions in a single layer conserve the total momentum of the 2DES (assuming no inelastic scattering on impurities, etc.). If there is an isolated second 2DES close enough for *inter*layer electron-electron Coulomb interactions to occur while interlayer tunneling is negligible, momentum can be transferred yielding a build-up of charges that are swept along in current direction of this second 2DES. This results in a voltage which is opposite to the voltage in the current-carrying layer [Tso1992] to balance the momentum transfer. The current carrying layer is referred to as the *drive layer* and the adjacent layer, which is passive and kept as an open-circuit, called the *drag layer*. The drag effect relies on charge inhomogeneities in form of density fluctuations/undulations [Zhe1993] which push away electrons in the opposite layer (two completely flat density distribution would not couple). Theoretical calculations show that at zero field the drag voltage has a T^2 and d^{-4} dependence, where d is the layer separation. However, measurements [Gra1993] had shown deviations which can be explained by phonon-mediated electron-electron interaction [Tso1992] for larger d. At zero magnetic field, the interlayer interactions are owing to direct momentum transfer via Coulomb scattering. At filling factor 1/2, the drag effect is explained in terms of Coulomb interaction between composite fermions, where electrons minimize their interaction energy by binding to an even number of magnetic flux quanta (see chapter 2) which exhibit a $\propto T^{4/3}$ dependence [Lil1998, Joe2000, Mra2004]. This simple drag model cannot explain the observations at $\nu_{tot} = 1$ where the behavior of drag changes dramatically [Lil1998], i.e., where the drag does not disappear with $T \longrightarrow 0$ K but instead exhibits a Hall drag with the same sign and magnitude as the Hall drive [Kel2002] being quantized to h/e^2 (in Hall bars). The existence of a quantized Hall drag at $\nu_{tot} = 1$ can be explained by making an analogy between Laughlin's wave function (equation 2.19) and the superconducting

vortex problem [Yan1998, Gir2002].

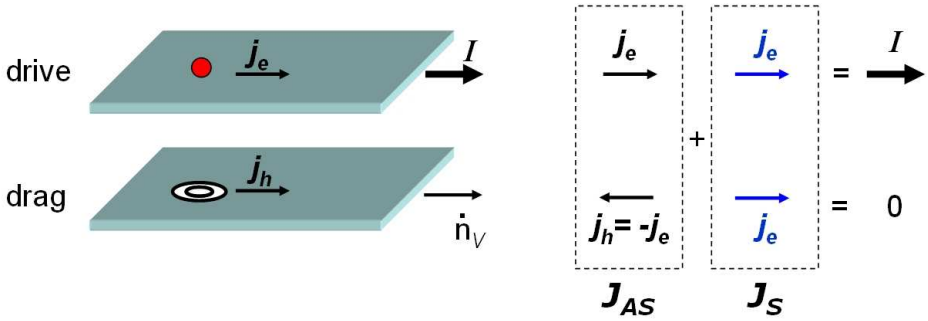

Figure 5.1: Cartoon of the bilayer at $\nu_{tot} = 1$. Left-hand side: an electron in the drive layer drags along a vortex in the adjacent layer (as each electron is attached to one flux quantum at $\nu_{tot} = 1$). Here I is the total drive current and $\dot{n}_v$ the flux of vortices. Right-hand side: as a vortex is equivalent to a missing charge (=hole), this means that this hole current j_h is equivalent to an oppositely directed electron current $-j_e$. The current j_e in the drive layer and the current $-j_e$ in the drag layer constitute the antisymmetric (exciton) current J_{AS}. Since no net current is allowed to flow through the drag layer, $-j_e$ is compensated for by a $+j_e$ which is present in both layers.

As described in chapter 3, in a single 2DES at filling factor 1/2 there are twice as many flux quanta/vortices (complex zeros of the wave function) as electrons. In the (bilayer) $\nu_{tot} = 1$ ground state, each electron is attached to one flux quantum, regardless in which layer the electron resides, so all electrons (i.e., independent of the layer index) strongly avoid one another. Thus, an electron in the drive layer will drag along a vortex in the drag layer (left-hand side of Figure 5.1). The electric current along the sample in the drive layer is then $I = e \cdot \dot{n}_e$, where $\dot{n}_e$ is the flux of electrons. The Josephson relation says that the voltage drop is given by $V = (\hbar/e)\dot{\phi} = (\hbar/e)2\pi\dot{n}_v$, where the Cooper pair charge $2e$ was replaced by e and the quantum phase of the system can wind by 2π. Since the flux of vortices $\dot{n}_v$ is identical to the flux of electrons $\dot{n}_e$, this yields the universal quantized Hall resistance h/e^2 (like for regular filling factor 1).

In a drag experiment no *net* current is allowed to flow in the drag layer. However, as charges are being dragged along, it violates this boundary condition. Thus there has to exist a mechanism to compensate for the net current in the drag layer. The exciton current that consists of an uniform electron-hole flow is referred to as the *antisymmetric current* J_{AS}[1]. The current that cancels the charge transfer in the drag layer is referred to as the *symmetric current* J_S which also exists in the drive layer owing to symmetry

[1] "Antisymmetric" because it corresponds to an electron-hole flow in one direction, or to two oppositely directed electron currents in the two layers.

reasons. The drag experiment is thus analyzed in terms of the symmetric J_S and the antisymmetric currents J_{AS} as shown on the right-hand side of Figure 5.1. The antisymmetric current is just the supercurrent from equation 3.6, i.e., $J_- = J_{AS}$, which produces no Hall field [Gir2002], and the symmetric transport channel is the one that can produce the quantized Hall plateau.

In the pseudo-spin picture the quantum Hall effect at $\nu_{tot} = 1$ can be viewed as follows: if the layers are uncoupled, the lowest Landau level of each layer is half filled, also only half of all pseudo-spin states are filled. However, for sufficiently strong coupling, the system is a pseudo-spin ferromagnet, i.e., the bilayer has a full pseudo-spin Landau level where the Fermi energy is in a pseudo-spin localized region and displays a quantum Hall effect.

5.2 Drag Measurement Setup

In an experiment with a real Corbino disk, a constant voltage is applied between the source and drain contact and only the current through the annulus is measured. As pointed out in chapter 4, the current in a Corbino ring consists of two parts (i.e., circular and radial), where the radial part oscillates between a finite value and zero as a function of the magnetic field. Hence, the radial voltage dropping across the annulus changes in response to that radial part of the current I_r as well. In a quantum Hall regime, I_r is zero and the entire voltage drops across the highly resistive annulus. If the resistance of the annulus is always large compared to other resistances in the circuit (such as the internal resistance of the voltage source), this does not pose a problem. However, in a quasi-Corbino ring at a non-integer filling factor its resistance might be comparable to those of the contacts arms, which are not entirely covered by the front and back gate leaving them at higher densities than the annulus itself. Since in this situation a large portion of the voltage might drop across the contact arms (which are not in a correlated state), the voltage across the annulus was monitored with a lock-in amplifier using a separate pair of contacts in a quasi four-terminal geometry. This will exclude the effect of the finite resistances of the Ohmic contacts and the contact arms.

Prior to all (drag) measurements, sufficient gate voltages are applied to the front and back gates as to provide separate contacts to both layers. At zero field interlayer tunneling experiments (see chapter 6) were performed and/or DC I/V characteristics were measured to check layer separation and obtain the interlayer resistances (details on each sample are found in the appendix).

All drag measurements were performed by using the internal oscillator of a lock-in to provide the low-frequency (2-5) Hz excitation voltage which is sized down to below

about 60 μV with a (50k:50) Ω voltage divider. This voltage was applied radially across the designated drive layer through an 1:1 isolation transformer, and a ground position is defined. The current through this layer was detected by measuring the voltage drop across a (1-10) kΩ resistor connected in series. In the diagrams of the experimental setup which are given with each measurement, for simplicity the current measurement is represented by the electric symbol for an ampere meter. The voltage across the drag layer was measured simultaneously. The drag layer is kept as an open circuit, however, to prevent it from floating it is either directly put to common ground or kept quasi-floating, i.e., put to ground over a large resistor. This resistor is chosen to be be at least one magnitude larger than the interlayer resistance in resonance, i.e., $>$ 10 MΩ. Initial investigations of the grounding position were performed which had shown that the experiment is indifferent to which perimeter the drag layer is grounded as long as it is in a quasi-floating geometry. Putting the drag layer directly to ground had initially shown to be indifferent of which perimeter is chosen as well. However, as some contacts/samples might become highly resistive at larger fields, direct grounding will not differ from having the layer quasi-floating. Especially the inner, smaller contacts are more resistive under strong magnetic fields than the outer ones (and may dissipate more energy).

The choice of which layer is the designated drive and drag layer is arbitrary. However, it was found that generally if the lower layer is used as drive layer, the currents at higher fields are lower and the $\nu_{tot} = 1$ regime is less pronounced. These differences may be attributed to the different mobilities and qualities of the two quantum wells (also contact resistances) which are strongly influenced by the properties of the interface to a quantum well in growth direction. Despite these obvious differences, the drag resistance $R_{Drag} = V_{Drag}/I_{Drive}$ will yield nearly the same value regardless of which layer is used to pass a current.

5.3 Interlayer Drag at Elevated Temperatures

Figure 5.2 shows a drag measurements performed on sample 81653:247C at ^{3}He temperature, i.e., $T_{bath} \approx 250$ mK. The densities in both layers were reduced simultaneous to be equal ($n_{upper} = n_{lower} \approx 2.12 \cdot 10^{14}$ m^{-2}) and producing a $d/l_B = 1.48$ at a total filling factor of one. The top panel shows the (radial) current through the drive layer and the lower panel the drive and drag voltage as a function of the magnetic field B. The inset illustrated the measurements setup. The current and voltages oscillate anti-cyclically as a function of B. At all integer filling factor, the current is zero and the drive voltage equals the excitation voltage. At total filling factor 1, a small minimum in the current is observable while peaks in the drive and drag voltage can be seen. While the current

hardly changes when the total filling factor moves across a value of one, the dissipation in the drive layer (marked by the voltage peak) is yet nearly doubled which indicates increased interlayer scattering. The longitudinal conductance of the drag layer must be small, or else the potential difference which exists between the inner and outer perimeter would be shortened.

Depending on the sample and the measurement setup, it was found that at all integer filling factors, features in the drag voltage can be found[2]. These feature show a very different characteristic if compared with the feature at $\nu_{tot} = 1$ and can be a lot smaller or even larger than the excitation voltage or the voltage peak at $\nu_{tot} = 1$. Figure 5.2 shows these features split up in their x-(in-phase) and y-(out-of phase) components. At all integer filling factors (where no drag is expected), the annulus is is highly resistive. Since the electron bilayer is in fact a capacitor, the relatively big out-of phase component is a signature of this large $R \cdot C$. However, tunneling will become important if the bulk resistance is magnitudes larger than the interlayer resistance.

All further drag measurements will be displayed in the more common notation where the calculated conductance $G = I_{Drive}/V_{Drive}$ is plotted versus B instead of voltages and currents separately. Figure 5.3 thus shows a contour plot of the drive layer conductance and drag voltage as a function of B and the single layer density $n = n_{upper} = n_{lower}$. With increasing density, the ordinary integer quantum Hall states shift to higher fields but do not change. The $\nu_{tot} = 1$ state, on the other hand, evolves smoothly and can be tracked to a $d/l_B > 1.76$ (at these elevated temperatures). With increasing density, screening effects become more relevant and the fermionic state of the single layers are dominating the transport regime.

To see how the $\nu_{tot} = 1$ quantum Hall state progresses, the data from Figure 5.3 can be re-analyzed by determining the conductance G at the minimum (center) at $\nu_{tot} = 1$ and the ratio of drag and drive voltage and plotting them versus d/l_B. The top panel of Figure 5.4 thus illustrates the conductance of the drive layer versus d/l_B and the bottom panel the ratio of drag and drive voltage. For (very) large values of d/l_B, the conductance appears to go into saturation, i.e., current and voltage approach values of a single layer at filling factor $\nu = 1/2$. While moving from high to low d/l_B, the conductance decreases slowly without showing a phase-transition with a critical behavior, before G appears to saturate again. The ratio of drag and drive voltage also displays a monotonic decrease from 1 beyond $d/l_B \approx 1.60$, i.e., the amplitudes of both voltage maxima diverge, indicating a breakdown of the correlated state.

[2]The usage of room temperature π-filters in addition to RL and RLC filters inside the probe at temperature below 4.2 K have shown to completely suppress these features (Cryostat provided by J. Smet).

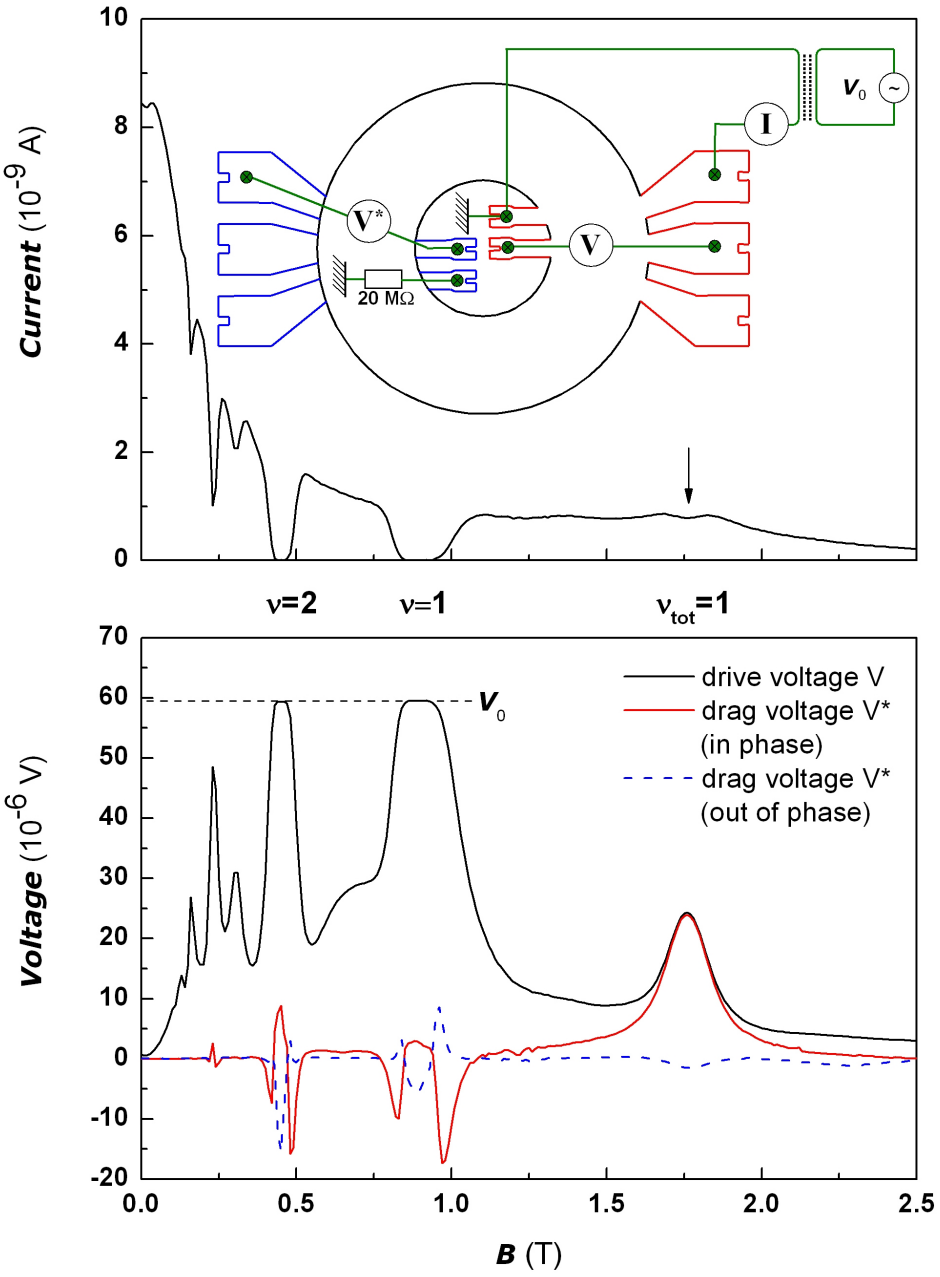

Figure 5.2: Results of a drag measurement at T_{bath}=250 mK for $n \approx 2.12 \cdot 10^{14}$ m^{-2}, i.e., d/l_B=1.48 at $\nu_{tot} = 1$. Top panel: current through the drive layer, measured as a voltage drop across a known resistance (see text for details). For simplicity the current measurement is represented by the symbol for an ampere meter. Inset: measurement setup, where red contacts are connected to the top and blue contacts are connected to the bottom layer. The voltage probe V measures the drive voltage V_{Drive} and V^* measures the drag voltage V_{Drag}. Bottom panel: drive and drag voltages. The latter is split up in its in-phase and out-of-phase components for clarity. Sample 81653:247C.

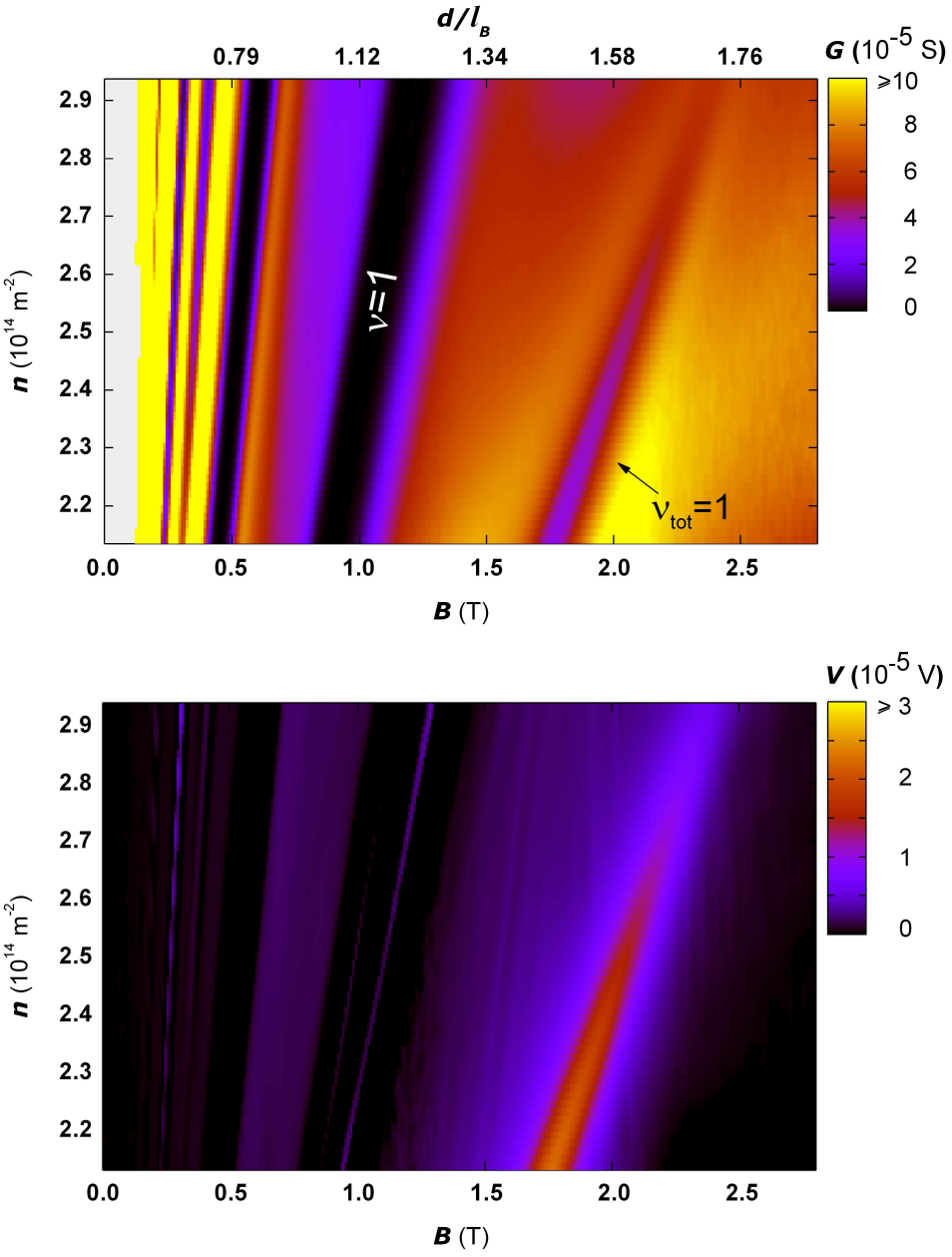

Figure 5.3: Contour plots of the conductance $G = I/V$ of the drive layer (top panel) and the drag voltage V^* (bottom panel) as a function of the magnetic field B (and d/l_B) and the density n of the single layer. Sample 81653:247C. T_{bath}=250 mK.

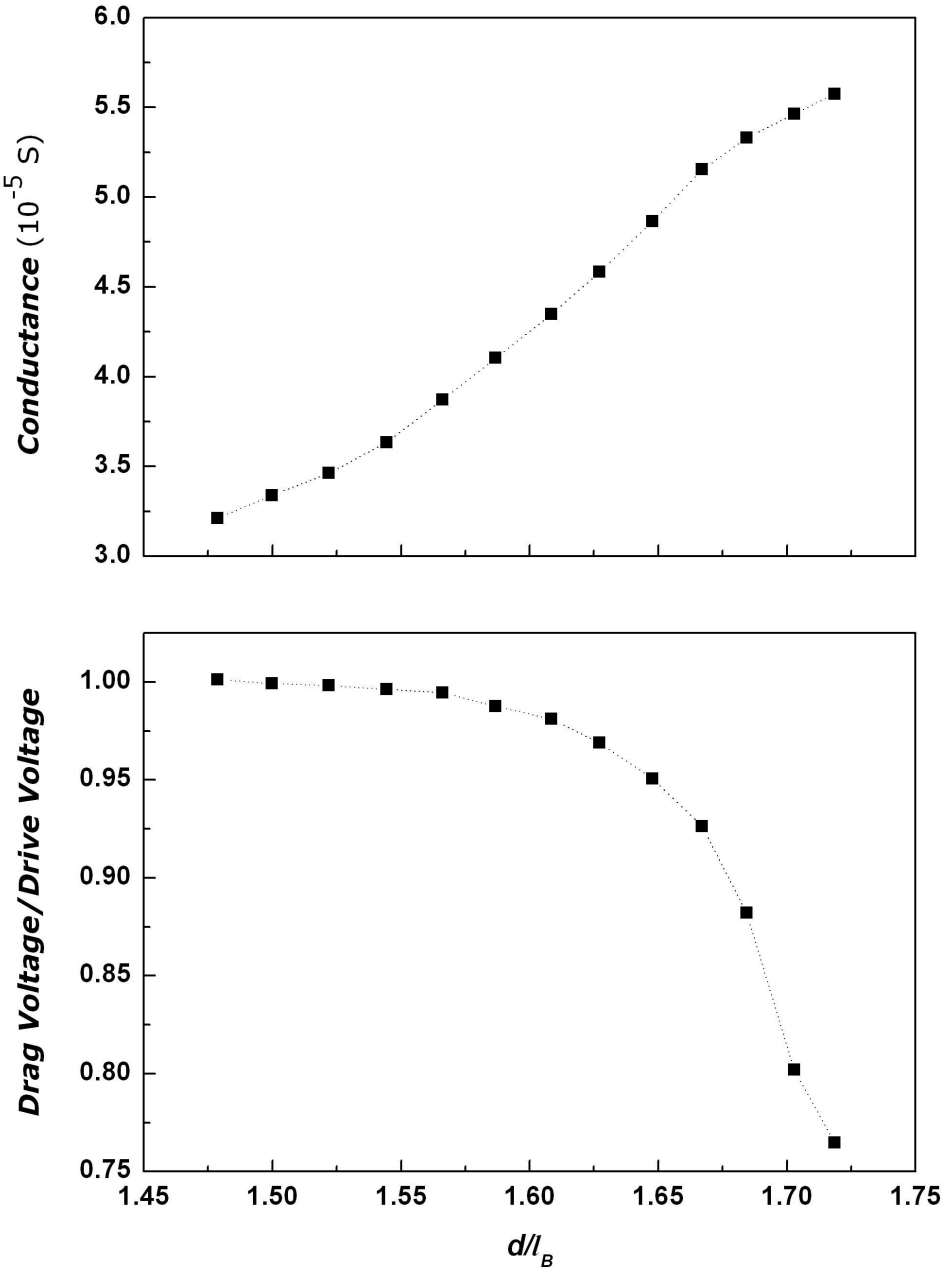

Figure 5.4: Re-analyzed data from Figure 5.3 where the top panel shows the conductance and the bottom panel the ratio of drag and drive voltage at a total filling factor of one plotted versus the corresponding d/l_B. Sample 81653:247C. T_{bath}=250 mK.

5.4 Interlayer Drag at Lowest Temperatures

At the lowest accessible temperatures of a dilution fridge, i.e., T_{bath}=15 mK, the conductance at a total filling factor of one vanishes nearly completely as shown in Figure 5.5. Drive and drag voltage are identical, and they are only about 1 % smaller than the excitation voltage V_0 which drops over the sample at the regular filling factor 1. These data were produced on sample 81653:248C. The single layer density is $n \approx 2.36 \cdot 10^{14}$ m^{-2}, which yields d/l_B=1.58 at $\nu_{tot} = 1$.

In chapter 4 the potential distribution for a Corbino device was simulated, which had shown a circular potential distribution when the Hall angle is at 90 degrees (see Figure 4.3). This is the case at all ordinary integer quantum Hall states. In analogy to these ordinary quantum Hall states at larger fillings, the behavior of the $\nu_{tot} = 1$ quantum Hall state may imply a circular potential distribution in the drive layer as well, or the existence of an azimuthal, i.e., circling, current. Owing to the excitonic coupling, this current would trigger an azimuthal current of the same magnitude in the drag layer, leading to identical voltages across both layers. However, as excitons are charge-neutral, they should be indifferent to the presence of the magnetic field so that this circular current should be carried by uncoupled electrons in a symmetric transport channel as discussed at the beginning of this chapter. However, from the magneto-transport data at hand it cannot be concluded whether this circling current model is correct, or if it is correct, where the current may flow. It could be homogeneously distributed throughout the bulk or rather concentrated at the sample edges. Circling currents could explain why drive and drag voltages are identical even though the corresponding voltages probes are located at opposite sides of the ring, approximately 1 mm apart. If the product of the scattering time and the cyclotron frequency is much larger than 1, i.e., $\omega_C\tau \gg 1$, then the Hall angle is close to 90 degrees. Rewriting equation 2.6 $\sigma_{xx} = \frac{\sigma_0}{1+\omega_C^2\tau^2}$ to $\omega_C\tau = \sqrt{\sigma_0/\sigma_{xx} - 1}$ yields[3] $\omega_C\tau = 168$ at $\nu_{tot} = 1$ for the low temperature measurement in Figure 5.5. The Hall angle Θ is connected with this product by $\Theta = arctan(\omega_C\tau)$ which then is 89.5 degrees. For the high temperature data in Figure 5.2 at $\nu_{tot} = 1$ it is found that $\omega_C\tau = 22$ and $\Theta = 87.4$ degrees. This suggests that the Hall angle is close enough to 90 degrees to observe identical voltages across opposite sides of the annulus, as shown in chapter 4. Note that this calculation implies a homogenous current distribution.

Despite the similarities between $\nu_{tot} = 1$ and the other regular integer filling factors in magneto-transport experiments, the observation of a transport gap and identical voltage across both layers at $\nu_{tot} = 1$ (regardless whether this is the case in Corbino rings or Hall bars) already demonstrates that the voltage drop *across the barrier* must be -at least- very

[3]The ratio of the conductivity is identical to the ratio of the conductances, because $G = \sigma \cdot A$, where A is a geometrical factor.

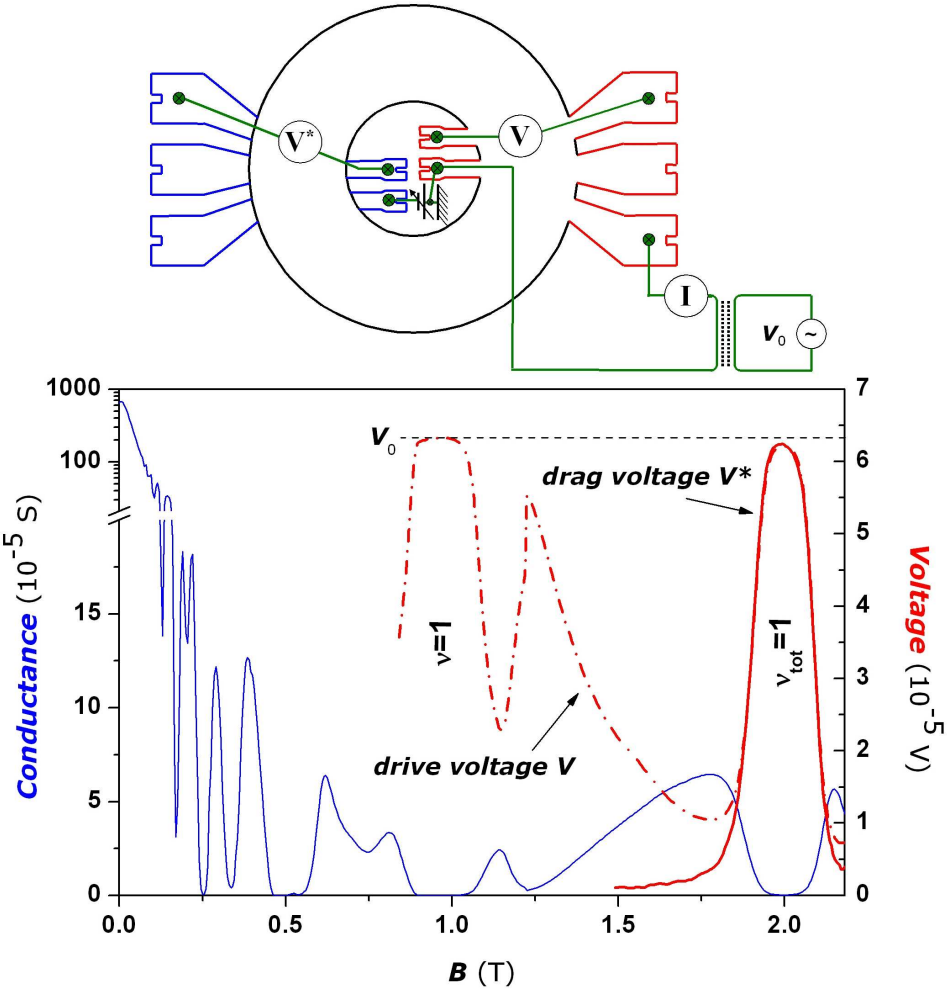

Figure 5.5: Combined plot of the conductance of the drive layer (blue, left vertical axis) and drive and drag voltage (red, right vertical axis) at T_{bath}=15 mK as a function of the magnetic field. At $\nu_{tot} = 1$ (d/l_B=1.58), the conductance vanishes like in the other integer quantum Hall regimes. The drive voltage is only shown to the single layer filling factor 1 to indicate the excitation voltage V_0. Data points of the drag voltage were omitted below 1.5 T. In this setup, the front gate plus an interlayer bias was used to tune the densities. Sample 81653:248C.

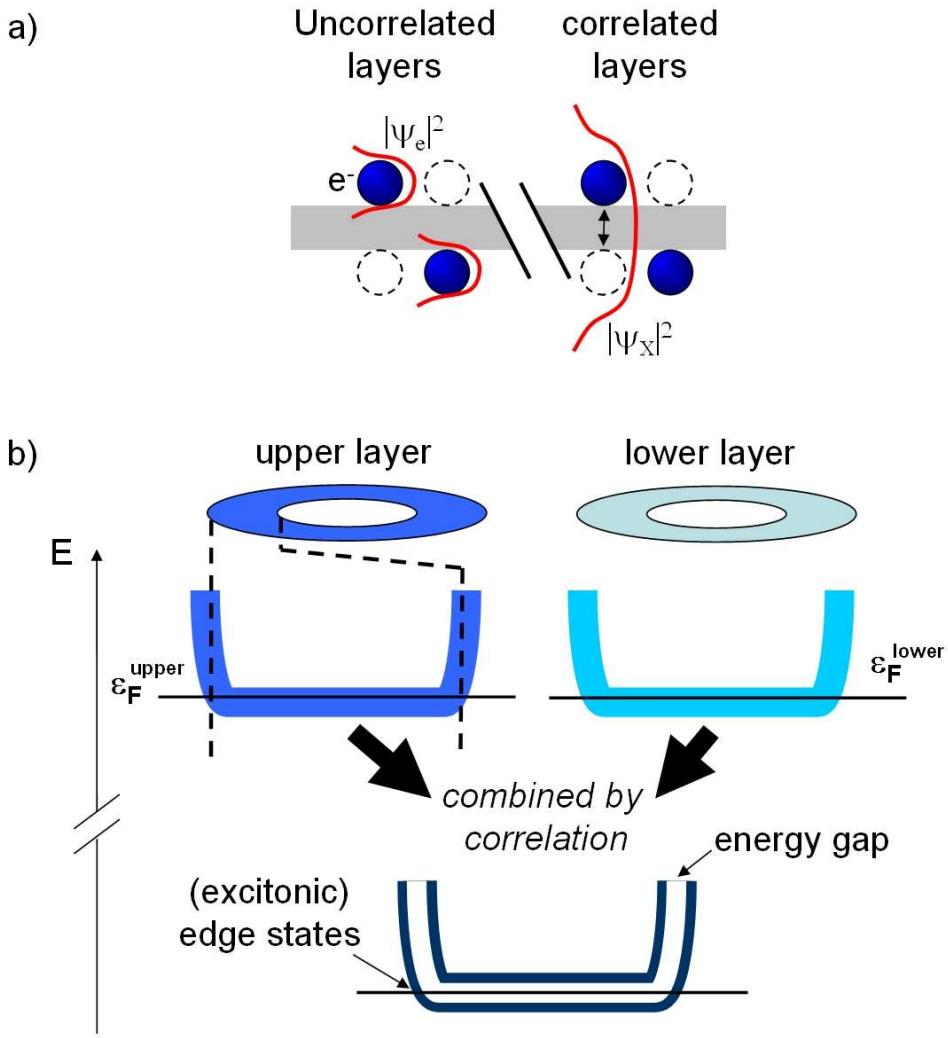

Figure 5.6: Model of excitonic edge state formation. a) while in two uncorrelated layers there is no overlap of the electronic wave functions, an excitonic wave function would have to exist across the barrier making it impossible to determine in which layer the electron/hole is in. b) at filling factor 1/2, the Fermi energy ε_F lies in the center of the lowest Landau level (for two uncorrelated layers), where the edges are of no particular relevance. In the correlated state, however, an energy gap will open up around ε_F, leading to a situation where available states only intersect ε_F at the sample edges.

small. Thus, identical voltages can equivalently be attributed to (condensate) electrons which are coherently spread between the layers and equilibrate any potential difference at $\nu_{tot} = 1$ (see chapter 3). Figure 5.6 tries to motivate a naïve model of the formation of excitonic edge states as suggested by Allan H. MacDonald. For two uncorrelated layers the single electron wave functions show no overlap, and the Fermi energy lies in the center of the lowest Landau level where the edge states are of no particular relevance. In the correlated regime, on the other hand, excitons will form, and it will require a finite amount of energy (i.e., energy gap) to break them apart and excite quasiparticles. This energy gap will open up around the Fermi energy ε_F which still lies in the center of the lowest Landau level. Since in this situation the only available states are those close to the sample edges, the situation is comparable to that at all ordinary integer filling factors. The wave function which is associated with the interlayer excitons, exists *across* the barrier and will equilibrate the interlayer potential to zero because the electron or hole (that participate in the correlated state) can be present in either one of the two layers. That means there is no chemical potential difference at $\nu_{tot} = 1$ between the two layers, and this is the same situation as in resonant tunneling which will be discussed in chapter 6. Thus, as the bulk of the correlated system is impenetrable for any current, it may as well be that the edges are in a state like the regular integer quantum Hall effect of single layer filling factor 1. It should also be emphasized that towards the edges the individual Landau levels bend upwards and progressively depopulate.

At some finite temperature, the collapse of the excitonic condensate can be observed, and the magnitude of the energy gap can be investigated via temperature activation. Generally, the activation energy is interpreted as the energy difference between the Fermi energy and the mobility edge [Sta1985], i.e., the boundary between localized and extended states. Figure 5.7 indicates that below 0.25 K, the conductance $G = I/V$ is well described by thermal activation, i.e., $G \propto exp(-E_{gap}/T)$, with an activation energy gap of approximately 0.5 K for d/l_B=1.58. The magnitude of this energy gap is in good agreement with earlier reports on comparable double quantum well structures [Kel2002,Kel2004,Wie2005] where the activation energy was extracted from measurements of the temperature dependence of the longitudinal resistance in Hall bars.

Like in Figure 5.4 for elevated temperatures, the onset of the $\nu_{tot} = 1$ state at lowest temperatures was investigated. The experiments is performed on sample 81653:146C by simultaneously reducing the (matched) densities n in both layers, adjusting the magnetic field to $B_{\nu_{tot}=1} \propto n$ and measuring drive current, drive and drag voltage, and in addition, the interlayer voltage with a separate pair of contacts. Figures 5.8 and 5.9 illustrate the results of this experiment. The top panel of Figure 5.8 thus shows the conductance of the drive layer versus the coupling parameter d/l_B. While moving from high to low

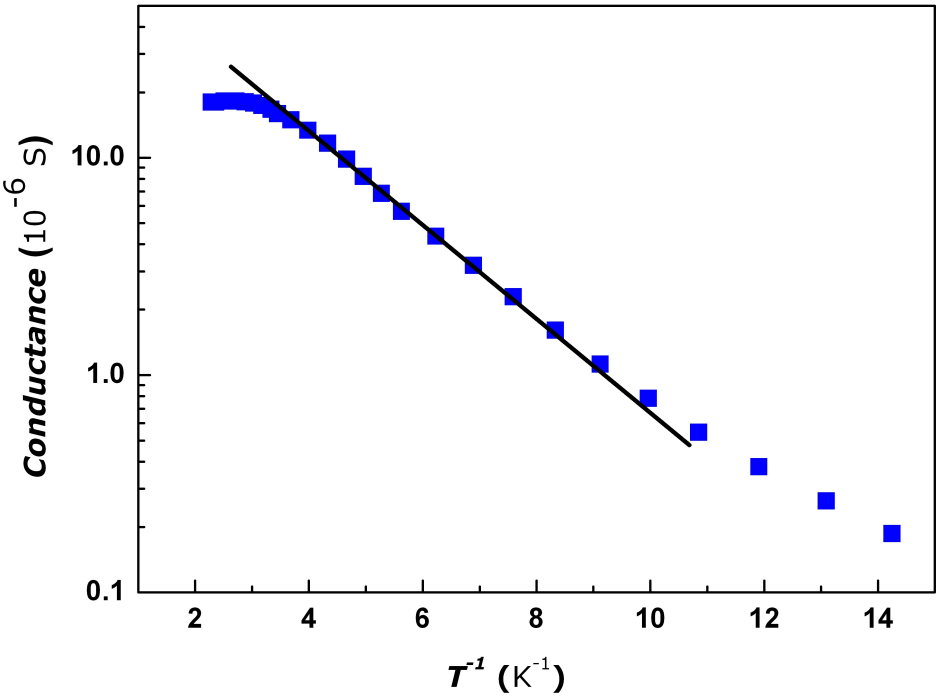

Figure 5.7: Temperature dependence of the conductance G versus the inverse temperature at $\nu_{tot} = 1$ (d/l_B=1.58). The black solid line is a fit using $G \propto exp(-E_{gap}/T)$. Sample 81653:248C.

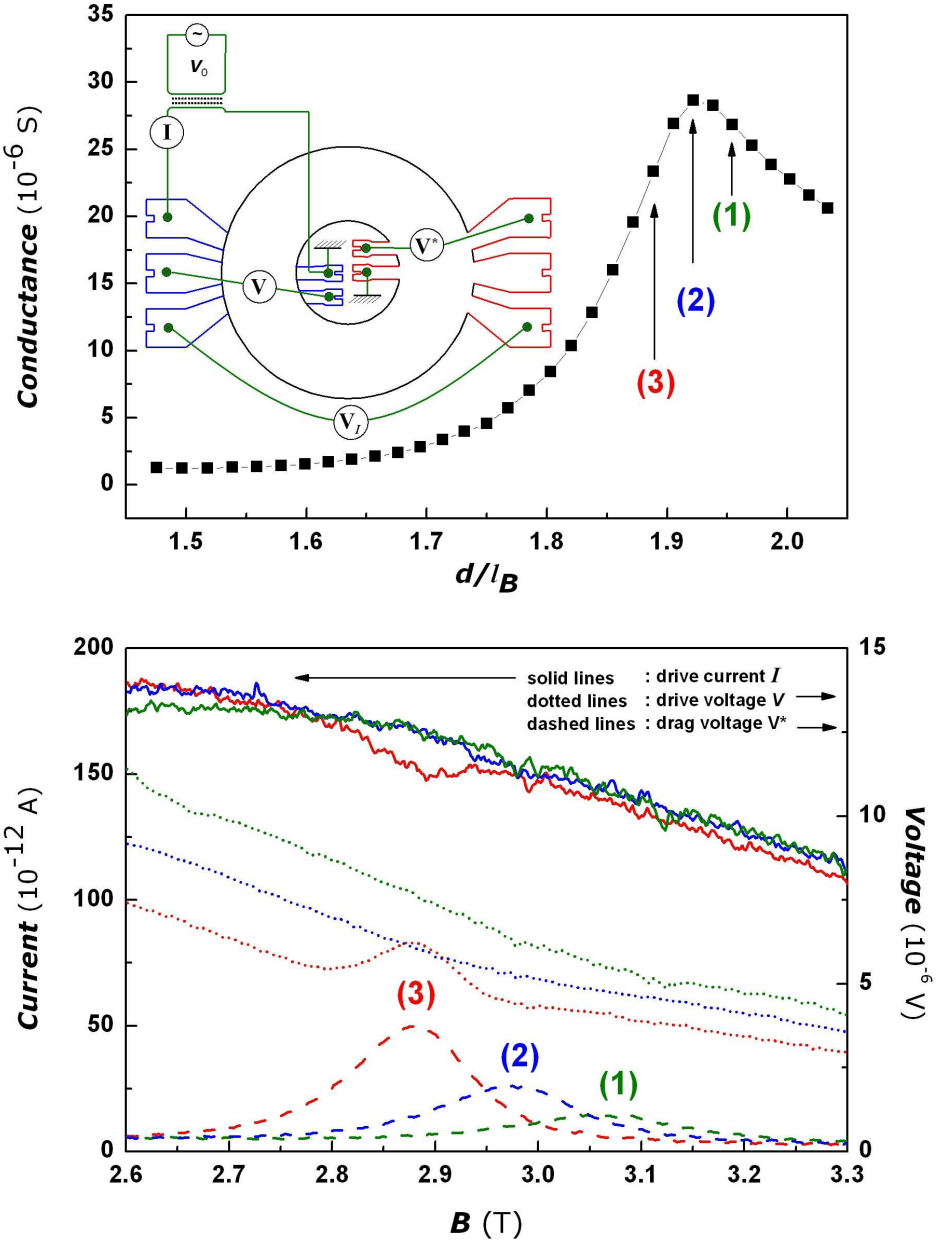

Figure 5.8: The top panel illustrates the conductance of the drive layer versus d/l_B. To investigate the elevation in the conductance around $d/l_B = 1.92$ with a $G_{max} \approx 30$ μS, the bottom panel shows magneto-transport sweeps around $\nu_{tot} = 1$ for three different d/l_B that lie in the vicinity of G_{max}. Solid lines show the current through the drive layer with the corresponding axis on the left-hand side, and the dotted/dashed lines the drive/drag voltage with the corresponding axis on the right-hand side. The interlayer voltage V_I is shown in Figure 5.9. Sample 81653:146C.

values of d/l_B, the conductance first exhibits an elevation before it slowly vanishes to nearly zero. To account for this unusual increase, three magneto-transport plots (1), (2) and (3) are shown on the bottom panel with the corresponding d/l_B=1.89, 1.92, 1.95. These three plots show that while the drive current is hardly affected, the drive voltage undergoes a significant change which, however, is not limited to the direct vicinity of filling factor 1/2. As the voltage appears to change "on a global scale" it suggests that the increase in G around d/l_B=1.90 may not be a relevant characteristic of the correlated state itself. Instead, the maximum may be the result of a competition between the increasing conductance $\sigma_{xx} = \frac{\sigma_0}{1+\mu^2 B^2}$ at $\nu = 1/2$ (no correlation) and the commencing interlayer correlation which suppresses scattering between the inner and outer edge and induces the gap at $\nu_{tot} = 1$. Yet, Figure 5.9 shows a very strong characteristic which is reminiscent of a phase transition point at about the same d/l_B. The behavior in the weak coupling limit differs from that observed at elevated temperatures, where the conductance at $\nu_{tot} = 1$ does not show a maximum. However, for 250 mK, the thermal energy is comparable to the energy gap as shown in Figure 5.7 which will lead to thermal fluctuations and a smearing of the effect.

In Figure 5.9 the ratio of drag and drive voltage is plotted versus d/l_B, which is 1 below $d/l_B = 1.75$, i.e., both voltages are identical. The same measurement on a different sample had shown that the ratio of both voltages is already 1 when the maximum in the conductance occurs. It is not clear if this difference is of a certain physical significance or not, or if the results of either of these two measurements is owing to a peculiarity of the sample that was used. However, in contrast to the previous sample, in this experiment the drive layer is more conductive. The inset shows the measured interlayer voltage which is compared to the calculated) difference between drive and drag voltage. Very significant is the sharp peak in the measured voltage which might indicate the phase transition between the correlated and uncorrelated state. At large coupling parameters these two values diverge but appear to re-approach another again.

The smooth transition from a vanishingly small conductance and identical voltages across both layers to two uncorrelated layers with a finite conductance and no drag voltage suggests that the model of a uniform Bose condensate of interlayer excitons might not be the physical reality. Rather, the system could be a fragmentation of single condensates as suggested by Stern and Halperin [Ste2002]. In their theoretical analysis, the electron bilayer system at high d/l_B ratios is composed of puddles of strong interlayer correlation incorporated in the compressible fluids of the individual layers. Their model, albeit addressing specifically Hall bar geometries, appears to be connected with our observations as well. As long as these puddles are small in number and/or unrelated, a sizable current could flow between these puddles through the bulk from source to drain. As

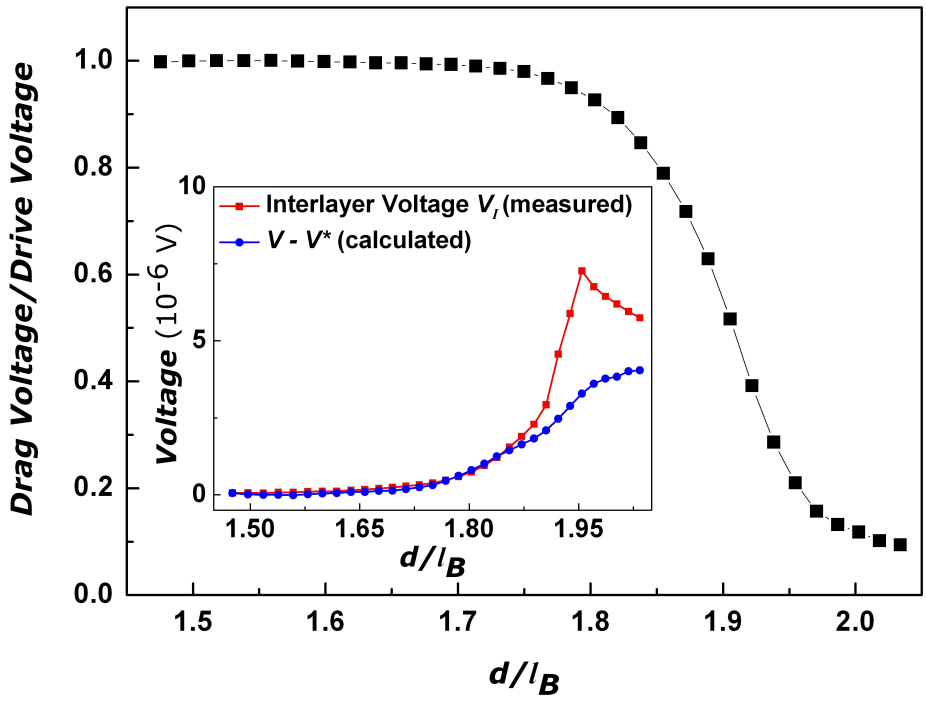

Figure 5.9: Ratio of drag and drive voltage versus d/l_B. Below $d/l_B < 1.75$ both voltages become identical. For the lowest $d/l_B = 1.47$, drive and drag are about 25 % smaller than the excitation voltage $V_0 = 35$ μV. The inset compares the interlayer voltage measured with probe V_I with the calculated difference between drive and drag voltage, i.e., $V - V^*$. For small coupling parameters both values are identical. The peak in the measured interlayer voltage could be reproduced in repeated measurements and might indicate the critical phase transition, where both layers become uncorrelated. Sample 81653:146C.

d/l_B is decreased, their number and/or size will increase until they eventually percolate, while the current through the bulk slowly diminishes. The smooth transition in Corbino samples from a compressible to a nearly fully incompressible state upon decreasing the temperature and/or the parameter d/l_B appears to signify such a percolation.

5.5 Separated Layers at $\nu_{tot} = 1$?

As previously demonstrated, identical drive and drag voltages mean that both layers are at the same potential and that the interlayer voltage is zero. Although, both layers are believed to be still electrically isolated, empirically the same result could be obtained if both layers were directly connected. The following experiment shows several magneto-transport sweeps between the ordinary $\nu = 1$ integer quantum Hall effect and the total filling factor one quantum Hall state. With each sweep of the magnetic field the voltage to the layer separation gate for the drag layer was reduced. This means that the Ohmic contacts of the drag layer will progressively (re-)connect to the drive layer. Figure 5.10 shows the drag voltage for this experiment. While the voltage to the two separation gates is progressively turned off from the value where the contacts are electrically separated from the drive layer, the drag voltage at $\nu_{tot} = 1$ does not change whereas at all other filling factors the drag voltage increases from zero to the value of the drive voltage. This experiment directly illustrates that at $\nu_{tot} = 1$ both layers appear to be directly connected, presumably in the vicinity of the edges.

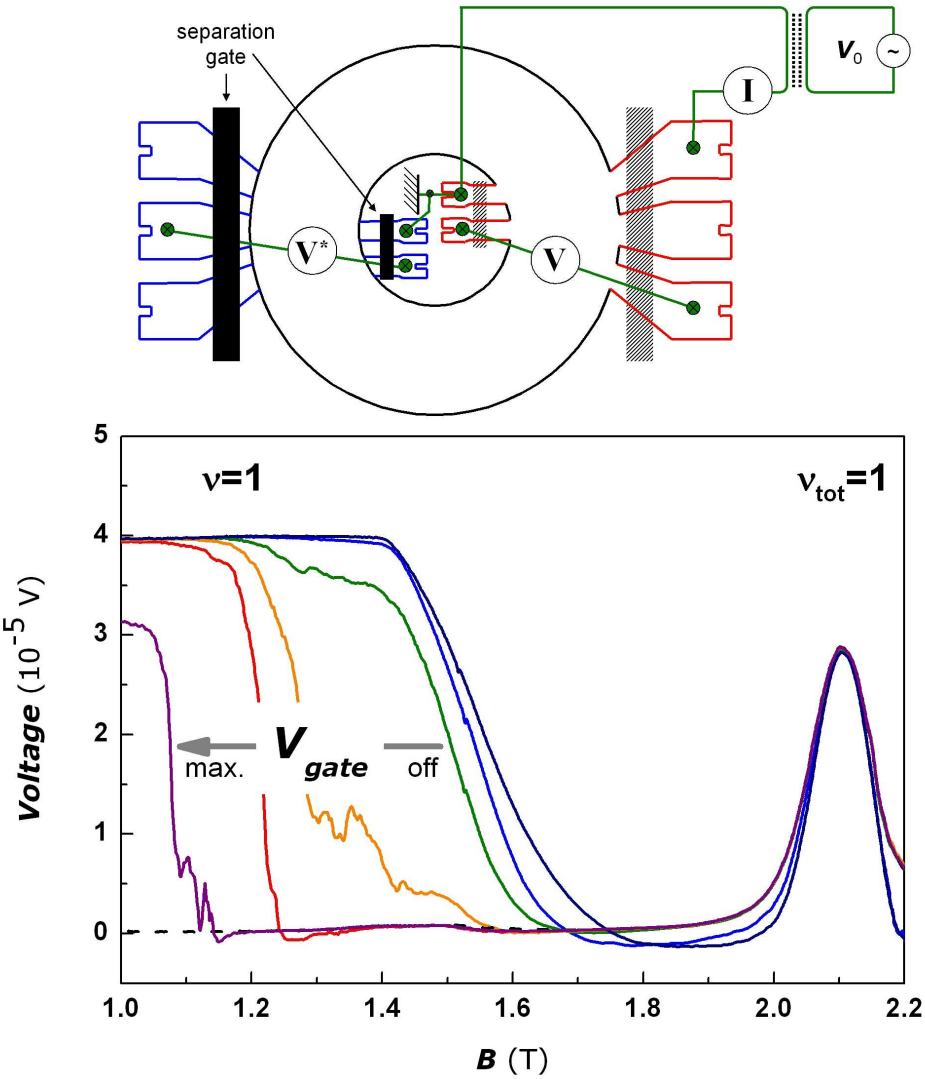

Figure 5.10: Voltage V^* across the drag layer versus the magnetic field for 7 different separation gate voltages. While the voltage to the black separation gates is progressively turned off (from the value where the contacts are electrically separated to 0 V), the drag voltage at $\nu_{tot} = 1$ does not change, suggesting its indifference to layer separation. However, at all other filling factors a (drag) voltage appears. For V_{gate}=0 V, the drive voltage (measured with probe V) and drag voltage (measured with probe V^*) are identical for all values of B. The dashed line shows the magneto-transport sweep for full contacts separation. The voltage to the shaded gates was not manipulated in this experiment. Sample D050803A:267C.

5.6 Additional Remarks

The transport properties of the $\nu_{tot} = 1$ quantum Hall state can further be investigated by imposing an imbalance on the systems electron density. Such a density imbalance refers to a density increase by -Δn in one layer and +Δn in the other one, leaving the total electron density n_{tot} unchanged. This has the consequence that the regular quantum Hall states will shift to lower/higher fields, due to a higher/lower density in the respective single layer. The $\nu_{tot} = 1$ quantum Hall state on the other hand depends only on n_{tot} and thus does not shift to a different magnetic field. It can be demonstrated that with increasing imbalance, the $\nu_{tot} = 1$ state will become broader with respect to the magnetic field in magneto-transport experiments. Very strong imbalances > 10 % will even merge $\nu_{tot} = 1$ with the regular $\nu = 1$ integer quantum Hall effect yielding a single very broad and undistinguishable quantum Hall state. The physics behind this is difficult because screening effects in one layer are increased which might lead to an intermixing of a Fermi gas-like system (in one layer) with the excitonic bilayer ground state. It was also shown that at large d/l_B, where there is no trace of the $\nu_{tot} = 1$ state, an imbalance can induce the correlated state [Spi2004]. Drag experiments conducted by Wiersma *et al.* [Wie2004, Wie2005] which compared the activation energies at different density imbalances had shown an asymmetry depending on in which layer the activation energy was measured.

A detailed discussion on density imbalances will not be given, however, imbalances become also relevant in interlayer tunneling experiments which will be discussed in the following chapter. These tunneling experiments will be able to account for the results of the interlayer drag experiments presented above.

5.7 Chapter Summary

The interlayer drag experiments on a Corbino device have shown that at a total filling factor of 1 an additional quantum Hall state appears and amplifies with decreasing temperature and decreasing coupling parameter d/l_B. This new $\nu_{tot} = 1$ quantum Hall state is characterized by a minimum in the drive layer's conductance and a drag voltage which is identical in sign and magnitude to the voltage across the drive layer. The smooth transition from a weak to a firmly established quantum Hall state with a vanishing conductance suggests the formation and percolation of correlated areas within the uncorrelated rest. Since for lowest temperatures and low d/l_B, this $\nu_{tot} = 1$ quantum Hall state displays a vanishing conductance like any other regular quantum Hall state, it implies the existence of a circular potential distribution. On the other hand, the identity of drive and drag voltages is argued to be the result of a Bose condensation where the electrons are coherently spread between both layers. In such a situation it would be absurd to refer to the two layers as being electrically isolated, at least in the common sense.

Chapter 6

Interlayer Tunneling

6.1 Background: Coherent and Incoherent Tunneling

An important technique to investigate the properties of a double quantum well is the differential tunneling conductance[1] $dG = dI/dV$. Measuring dG is very useful in non-linear devices, or in devices of reduced dimensionality, where the resistance is not a constant (i.e., Ohmic behavior) but changes along the I/V curve. A differential conductance curve can be obtained by directly measuring the I/V curve (i.e., apply a tunable bias voltage V and measure the current I) and calculate its derivative. However, in this direct DC measurement any noise might be amplified. Alternatively, the modulation of a tunable DC bias V_{DC} with a low amplitude AC sine wave V_{AC} which is applied between the two layers is a convenient and commonly used method to determine the differential conductance dI_{AC}/dV_{AC} experimentally. Since the AC modulation is very small compared to V_{DC}, it can be viewed as a perturbation. Thus the current $I = I(V)$ with $V = V_{DC} + V_{AC} \cdot sin(\omega t)$ can be approximated in a Taylor series as

$$I(V) \approx I(V_{DC}) + \left(\frac{dI}{dV}\right)_{V_{DC}} V_{AC} \cdot sin(\omega t) + \dots . \tag{6.1}$$

The AC amplitude is chosen to be (a lot) smaller than the Fermi energies of both 2DES which are in the meV range, so only electrons at the Fermi level will participate. The AC modulation method has the advantage of allowing a sensitive low-noise measurement of the second term $dI = dI_{AC}$ of the equation above. On the other hand, during the measurement with a lock-in amplifier, problems with the phase might arise under strong magnetic field conditions (due to capacitances and large resistances). An I/V character-

[1] Also referred to as *tunneling spectroscopy*.

istic can be deduced by integration, i.e., $I_{AC} = \int dG \cdot dV_{DC}$.

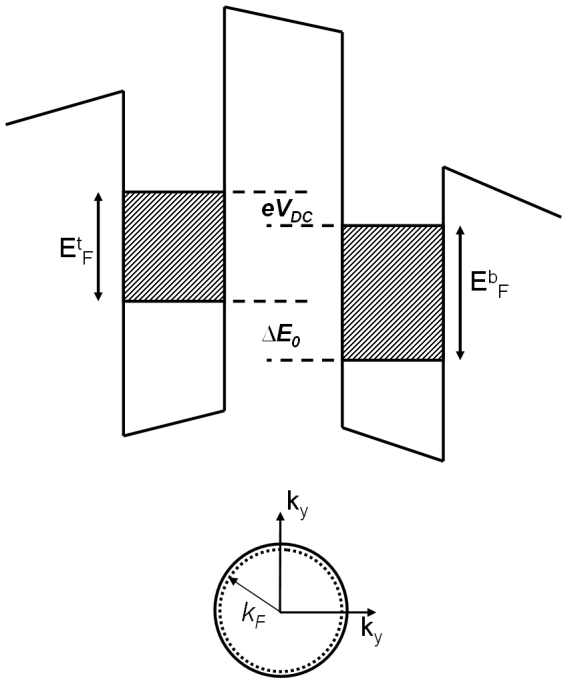

Figure 6.1: Top: band diagram of the double quantum well with an applied interlayer bias V_{DC}. The densities in the two quantum wells are slightly imbalanced, and the two Fermi energies are shifted by eV_{DC}. Bottom: Fermi surface $k_F = \sqrt{k_x^2 + k_y^2} \propto \sqrt{n}$. Only when the momentum k_F for both quantum wells or the respective energies $\propto k_F^2$ are conserved, resonant tunneling can occur. Dotted line is for the upper quantum well which has a slightly smaller density. After [Eis1991, Eis1992].

At zero magnetic field, tunneling between two 2DES can be explained in terms of a simple single-particle picture [Eis1991, Eis1992] depicted in Figure 6.1: the Fermi energy in the top and bottom quantum well is given by $E_F^{t,b} = n^{t,b}/D_0$ (see equation 2.15, with $n^{t,b}$: electron density, D_0: density of states). It is assumed that $k_B T \ll E_F$ while both quantum wells are identical and the barrier is free of impurities so no electron scattering occurs. Application of a finite DC voltage $V_{DC} \neq 0$ will yield a static counter-shift of these two Fermi energies by eV_{DC}. Due to the capacity of the double quantum well system[2], the electron densities in both quantum wells will then be imbalanced, i.e., the density in one quantum well is decreased by the same amount as it increased in the other quantum well. Tunneling is possible when the sub-band edges of the two quantum wells align and ΔE_0 is nearly zero [Eis1991]

[2]In the appendix, an estimate for the capacity of our bilayer systems can be found.

$$\Delta E_0 = eV_{DC} + (n^b - n^t)/D_0 \approx 0. \tag{6.2}$$

For small V_{DC} this condition is equivalent to $n^t = n^b$, so a $V_{DC} \approx 0$ V will allow tunneling. In this condition, (in-plane) momentum and energy is conserved because the energetic states of both quantum wells are $\frac{\hbar^2 k_F^2}{2m^*}$ with $k_F^2 = k_x^2 + k_y^2 \propto n$. This process is referred to as *resonant tunneling*. The AC voltage dV_{AC} which weakly modulates the DC voltage, creates a small AC (tunneling) current dI_{AC} which can be detected by a lock-in amplifier. The differential conductance dI_{AC}/dV_{AC} plotted versus V_{DC} thus shows a sharp peak centered around $V_{DC} \approx 0$. The presence of a tunneling current of course requires the bare Δ_{SAS} to be non-zero. The tunneling Hamiltonian can be written in a pseudo-spin language as [Par2006]

$$H_{tl} = \Delta_{S,AS} \sum_k (c_{k,\uparrow}^\dagger c_{k,\downarrow} + c_{k,\downarrow}^\dagger c_{k,\uparrow}), \tag{6.3}$$

where it is assumed that momenta are conserved, i.e., there is no tunneling between different k-states.

In real samples, the tunneling peak is not singular as implied above, rather, tunneling peaks possess a finite width which results from scattering (breakdown of momentum conversion) on static disorder inside the barrier. Also interface defects such as fluctuations in the width of the quantum well, which will produce a sub-band energy shift [Eis1991], can yield a broadening. Yet, it is difficult to quantify the disorder. However, the broadening by disorder is always influenced by the finite life-time of electrons τ within the wells [Zhe1993b, Mur1995]. Thus, the experimentally measured full width at half maximum (FWHM) Γ of the tunneling peak is directly proportional to the average life-time of the electrons, i.e., $\Gamma = \hbar/\tau$. The width of the tunneling peak increases with the temperature due to electron-phonon and electron-electron scattering at higher temperatures, and not by thermal smearing as one might expect since the constraint of momentum-conservation is indifferent to the thermal population of the momentum states [Mur1995].

Under the application of a perpendicular magnetic field B, the density of states changes as a function of B and at large enough fields the kinetic energy is quenched while Coulomb correlations dominate the dynamics of the system. The high field localizes the electrons on a length scale of the magnetic length l_B. An electron designated to tunnel, must first be extracted from one correlated liquid and then (re-)injected into an interstitial position of the other liquid which both times requires a finite energy $eV_{DC} \sim E_C$ of the order of the Coulomb energy E_C. After the tunneling process, the electrons in both systems will relax. These energy penalties suppresses tunneling at the Fermi level which creates a pseudo-gap (Coulomb blockade) [Eis1992].

This pseudo-gap is also expected for tunneling between two quantum wells each at filling factor 1/2. However, when the coupling factor d/l_B is sufficiently small to exhibit the total filling factor 1 quantum Hall state, tunneling experiments instead shows a dI/dV anomaly with a sharp zero bias tunneling peak as shown first by Spielman *et al.* [Spi2000]. This strongly enhanced conductance peak, which for low d/l_B has a much higher amplitude than the peak at B=0 T, is believed to be the direct indication of the macroscopic phase coherence. The (integrated) I/V characteristic has an astonishing resemblance to the one of the Josephson effect of superconductivity which originates from the phase coherence between two superconductors. Even though the ground state of the bilayer system can be mapped onto the BCS-type wave function as shown in chapter 3, the bilayer at $\nu_{tot} = 1$ is only partially analogous to a Josephson junction [Ros2005, Par2006]. In fact, it is important to recognize the experiment as tunneling between two electron systems that only as a whole form the correlated state [Par2006]. This also explains why no true DC supercurrent at zero bias has been observed so far (details later in the text). The enhanced conductance peak in bilayers is directly related to the presence of interlayer phase coherence of the Bose condensation which equilibrates any chemical potential difference as shown in Figure 6.2. Since small interlayer voltages cannot induce any chemical potential difference, the sub-band edges of both Fermi energies remain aligned (as in resonant tunneling at zero field). In the ground state, the total net interlayer current is zero, since any charge-transfer will be in both directions. That means it is hard to prevent tunneling between the layers when they are close enough to exhibit interlayer phase coherence. However, a potential difference that breaks the balance can be imposed by the external leads [Par2006, Su2008].

The observables in any of these measurements performed on the bilayer $\nu_{tot} = 1$ state are the currents and voltages in the (uncorrelated) leads [Su2008], so there is no direct access to what is happening within the correlated bulk. As shown in chapter 3, the ground state of the bilayer system in the correlated regime can be described by the Halperin (111) state, as the Laughlin wave function describes the ground state of the fractional quantum Hall effect. And like in the fractional quantum Hall effect, it is convenient to introduce the quasiparticle concept [Fog2001, Ros2005, Par2006, Su2008]. The quasiparticles in the bilayer system arise at the interface where the single particle electron current from the leads meets the correlated $\nu_{tot} = 1$ phase. This interface is located at the sample edges, so when the $\nu_{tot} = 1$ quantum Hall effect is firmly established, any quasiparticle transport will occur near the edges of the system. Every incident single electron from the leads is changed into a quasiparticle of the Bose condensate which can then be easily transferred and exits into the leads in the adjacent layer. This process which conserves total charge in both layers is analogous to Andreev reflection [Mac0708]. The constant flow of quasiparticles

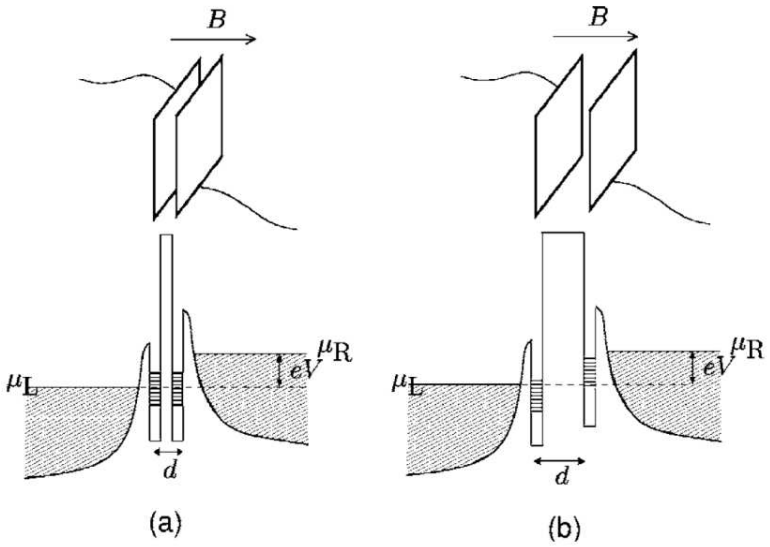

Figure 6.2: For coherent quasiparticle tunneling between correlated layers at $\nu_{tot} = 1$ there is no chemical potential difference between the two layers, as shown on the left-hand side. When d or d/l_B is sufficiently large (right-hand side), the two layers are independent and regular single electron tunneling is taking place. From [Par2006].

(across the barrier) is the process that will be referred to as *quasiparticle tunneling*, as the quasiparticle Hamiltonian of a real superconductor has pair creation and annihilation terms. Like regular zero field resonant tunneling requires that the bare $\Delta_{S,AS}$ to be non-zero, also the tunneling at total filling factor 1 needs a small but finite $\Delta_{S,AS}$ (which is constant since it depends on the layer separation d only). Thus, to observe the $\nu_{tot} = 1$ quantum Hall state in tunnel experiment with *spontaneous* interlayer phase coherence, i.e., with $\Delta_{S,AS} \longrightarrow 0$, is unrealistic. In fact, the finiteness of $\Delta_{S,AS}$ appears to be a vital component. The reported independence of the Hall drag (in Hall bars) from an interlayer bias [Kel2002] was used as counter-evidence for the relevance of tunneling in magneto-transport experiments. However, it was assumed that an interlayer bias will suppress resonant tunneling, like it would do at zero magnetic field. At total filling factor 1, however, this is not the case (anymore) as the measurements in this chapter will demonstrate!

In the pseudo-spin picture presented in chapter 3, tunneling in quantum Hall bilayers is an example of pseudospin transfer, where the planar pseudo-spin orientation φ in the xy-plane is in fact the phase difference between the two layers. And as pointed out, the (small) single particle tunneling amplitude $\Delta_{S,AS}$ selects this phase difference [Ros2005]. The exciton condensate can carry an interlayer current by adjusting its (macroscopic) phase difference φ. This phase is analogous to the phase of the order parameter in a

conventional superconductor. It can be shown [Par2006] that the expectation value of the interlayer current is given by

$$\langle \widehat{I}_{Interlayer} \rangle = 2e\Delta_{S,AS}(\langle S \rangle sin(\varphi)), \tag{6.4}$$

where $\langle S \rangle$ is the expectation value of the pseudo-spin vector in the xy-plane of the pseudo-spin field. Hence, when there is (spontaneous) coherence, the range of currents over which there exists a large conductivity is proportional to $\Delta_{S,AS}$, so that the tunneling peak gets narrower and narrower as $\Delta_{S,AS}$ goes to zero [Ros2005, Par2006]. There exists a maximal current that can be carried by the coherent state [Eza1993] which is given by [Par2006],

$$\langle \widehat{I}_{Interlayer} \rangle \leqslant I_{critical} = 2e\Delta_{S,AS}\langle S \rangle. \tag{6.5}$$

This termination of the coherent quasiparticle tunneling beyond a critical value which depends on $\Delta_{S,AS}$ is the reason why the tunneling conductance has a narrow peak near zero bias, i.e., the tunneling conductance is coherent (i.e., carried by quasiparticles) only within a small window of the effective interlayer bias voltage. Once this bias voltage gets large enough, the tunneling current will become too large to be carried by quasiparticles. The then commencing regular electron tunneling has a low conductance as tunneling occurs between regular composite Fermion seas [Par2006]. However, below $I_{critical}$, the bilayer system does not show a DC Josephson effect in the conventional sense with infinite tunneling conductance. As all experiments indicate, the tunneling anomaly always displays a finite height and width [Spi2000, Spi2001, Spi2004, Chm2008]. Several mechanisms are considered to limit the "bilayer Josephson effect", such as topological defects in the pseudo-spin field. These merons (introduced in chapter 3) whose motion destroy the long-range order, constitute a dissipative environment [Ste2001, Bal2001]. The (differential) conductance can be calculated to be finite, i.e., $I \propto |\langle \widehat{T} \rangle|^2 \cdot V$ [Par2006], where $\langle \widehat{T} \rangle$ measures the phase coherence between the states from opposite layers.

Despite several theoretical approaches there is no unifying theory which is able to account for both the Josephson effect-like behavior and the observation in magneto-transport experiments. The model of quasiparticle tunneling induced by a process comparable to Andreev reflection is a very powerful tool and appears to agree well with the empirical data that will be presented below, however, it still lacks definite experimental proof.

6.2 Interlayer Tunneling Experiments

In the tunneling measurements about to be shown, identical densities in the two layers were produced by using the top and bottom field gates. With this method both quantum wells remain at the same Fermi energy since both layers are connected to the same (ground) potential by at least one Ohmic contact. Applying an interlayer bias on the other hand, will counter-shift the Fermi energies and consequently the density of states of both layers. Owing to a capacitor effect, electrons will redistribute from the quantum well at the higher potential to the one at the lower potential. That means that when the interlayer bias is swept during a tunneling experiment, a (varying) density imbalance is imposed onto the bilayer. The bias-induced imbalance for the standard Hall bar geometry is about 4 % for an interlayer bias voltage of 500 μV. This imbalance was both measured with magneto-transport experiments and confirmed by estimating the bilayer's capacitance ($\approx$ 250 pF, see appendix) and calculating the charge transfer upon applying a voltage. However, by using the Shubnikov-De Haas oscillations in magneto-transport experiments in the low field regime (i.e., filling factor > 1), it is possible to adjust the voltages to the front and back gate while sweeping the interlayer bias to keep the electron density in each of the two layers constant. While this adjustment has a negligible effect around zero bias, it can alter the details of the tunneling characteristic at large biases. Details can be found later in the text. However, in all tunneling experiments presented here, the front and back gates are not adjusted while sweeping the interlayer bias to account for the density imbalance in both layers, unless it is specifically mentioned.

The notation for the voltages is as follows: any *applied* 2-terminal voltages are referred to as V_{DC} and V_{AC}, optionally the abbreviation "2pt" may be added. All *measured* 4-terminal voltages always include the superscript "4pt", i.e., V_{DC}^{4pt} and V_{AC}^{4pt}, to clearly distinguish between 2- and 4-terminal/point measurements.

6.3 AC Modulation of a DC Interlayer Bias

The contour plot of Figure 6.3 shows the 2-point (2pt) differential tunneling conductance dI_{AC}/dV_{AC} plotted versus the magnetic field B and the 2pt voltage V_{DC}, because it is assumed that the interlayer resistance is still much larger than any other (contact) resistances. The differential tunneling conductance was measured as previously described. The AC voltage from the internal oscillator of a lock-in amplifier and DC voltage from an external voltage source were reduced and added, resulting in a $V_{AC} \approx 17\mu V$ (3 Hz) for this experiment. The virtual ground (VGND) of the same lock-in amplifier was used to detect the AC current. On the top panel on right-hand side, a (rotated and mirrored)

magneto transport sweep of the conductance in a drag experiment is shown (for the same density) which allows direct comparison with the different regimes and filling factors when the magnetic field is varied. The bottom panel shows several cross sections of the contour plot. These measurements were performed on sample 81653:247C at $T_{bath} \approx 250$ mK with balanced carrier densities of $n \approx 2.12 \cdot 10^{14}$ m^{-2} in each layer.

While at zero field, we can observe the zero bias tunneling peak, the magnetic field will suppress tunneling around zero bias at all integer filling factors due to the Coulomb blockade. At total filling factor 1, on the other hand, a tunneling anomaly appears. Owing to the interlayer phase coherence the electrons can easily tunnel without being submitted to the Coulomb blockade. However, unlike prior reports which had shown this anomaly to be very sharp [Spi2000, Spi2001, Spi2004], the anomaly shown in Figure 6.3 is very broad instead. Its FWHM is roughly 7 times larger than the one at zero field. As pointed out, disorder greatly influences the width of the tunneling peak. Yet, this strong increase in width does not appears to be related to disorder, and as Figure 6.4 suggests, the width of the tunneling anomaly further increases with decreasing d/l_B. Since from high to low values of d/l_B, the full width at half maximum in these three cases is about (60, 160, 200) μV, the origin of this behavior must be found somewhere else. These latter measurements were performed on sample 81653:210H at $T_{bath} \gtrapprox 25$ mK[3] and $\nu_{tot} = 1$ with balanced carrier densities in the two layers leading to three different d/l_B which are compared to the one at zero magnetic field. Even though, these data were produced on a Hall bar, the results do not qualitatively differ from data obtained on a Corbino ring. The tunable DC bias was modulated with a small (≈ 7 μV) AC voltage (5 Hz). The AC current was detected by measuring the voltage drop across a 10 kΩ resistor connected towards common ground, instead of using the virtual ground of a lock-in amplifier as in the previous experiment. However, in the diagram of the experimental setup, for simplicity the current measurement is represented by the electric symbol for an ampere meter.

Plotting the measured 4pt voltages V_{DC}^{4pt} and V_{AC}^{4pt} versus the 2pt DC voltage V_{DC} as shown on the top panel of Figure 6.5 illustrates that both the AC and DC voltage break down when the coupling parameter is reduced. At zero magnetic field, on the other hand, it is hardly affected at all. As pointed out at the beginning of this chapter, once interlayer phase coherence is established it is difficult to impose any electrochemical potential difference on the two layers (Figure 6.2). With increasing phase coherence, i.e., with decreasing d/l_B, it becomes progressively harder to impose such electrochemical potential difference, so the 2pt voltages need to become larger and larger, resulting in their strong reduction around zero bias. This means that 2pt measurements should generally

[3]Owing to a technical problems with the cryostat, the bath temperature was larger than in prior experiments.

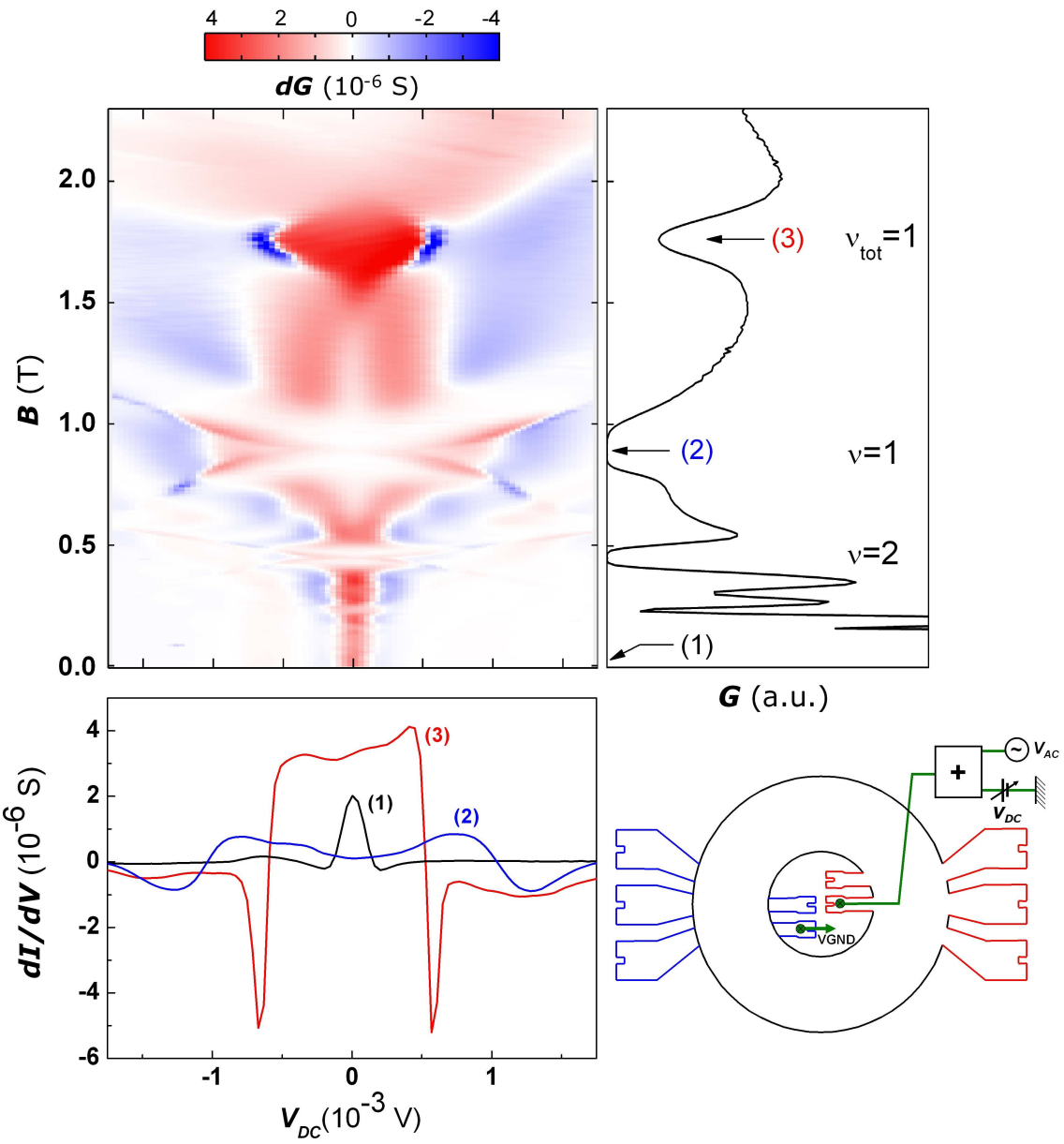

Figure 6.3: Differential conductance $dG = dI/dV$ versus the magnetic field and the 2pt DC interlayer bias at T_{bath}=250 mK (top left) for $n_{upper} = n_{lower} \approx 2.12 \cdot 10^{14}$ m^{-2}. To locate the different filling factors, a rotated and mirrored magneto-transport sweep is shown (top right). The bottom panel shows cross-sections at B=0 T, filling factor 1 and total filling factor 1 (both color-coded and marked with (1), (2) and (3)). A broad zero bias tunneling anomaly at total filling factor 1 is observed, while at the regular filling factor 1, tunneling is suppressed at zero bias. The measurement was set up as shown (bottom right) and explained in the text. Sample 81653:247C.

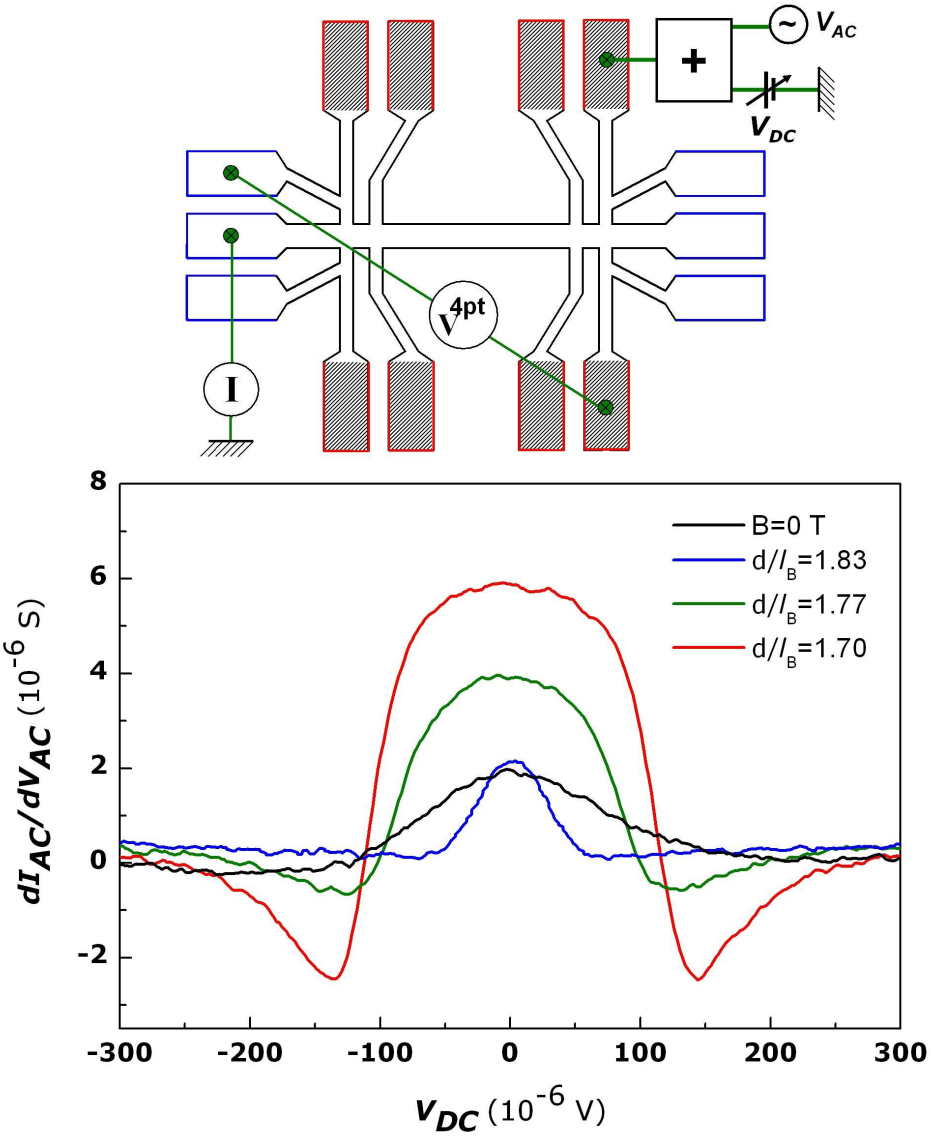

Figure 6.4: Differential conductance $dG = dI/dV$ for three different values of $d/l_B = \{1.70,\ 1.77,\ 1.83\}$ and at zero magnetic field versus the 2pt DC interlayer bias at $T_{bath} \gtrapprox$ 25 mK. With decreasing d/l_B, the FWHM increases. The top panel shows the schematics of this experiment. Red contacts (shaded) connect to the upper layer and blue ones to the lower layer. The AC and DC voltage were reduced and added. The current was measured as the voltage drop across a known resistance (see text for details). However, for simplicity the current measurement is represented by the symbol for an ampere meter. The measured 4pt interlayer voltage V_{DC}^{4pt} and V_{AC}^{4pt} will be shown in Figure 6.5. Sample 81653:210H.

not be used in interlayer tunneling experiments at $\nu_{tot} = 1$ because it cannot be assumed that the interlayer resistances is much larger than other resistances anymore. The strong elevation of V_{AC} prior to its vanishing is not accompanied by an out of phase component. This behavior at the flanks remains unaccounted for, however, it explains the largely negative conductance of the dI/dV curve at the flanks of the tunneling anomaly around zero bias. The largely reduced 4-terminal voltages mean that the differential conductance dG curve, which assumes that $dV_{AC} \approx 7$ μV to be constant and $V_{DC} \approx V_{DC}^{4pt}$, is incorrect. A largely reduced dV_{AC} will increase the height of dG and if plotted versus V_{DC}^{4pt} instead of V_{DC} its width will decrease. Figure 6.6 thus shows dG for a single representative value of $d/l_B = 1.70$ which uses the measured 4-terminal voltages V_{DC}^{4pt} and V_{AC}^{4pt} from Figure 6.5. The full width at half maximum thus reduces from about 200 μV to less than 30 μV.

As all these measurements already indicate, while moving deeper into the correlated total filling factor 1 state, the bilayer changes from two layers which are separated by a (large) interlayer resistance comparable to that at zero field to two layers which appear to be electrically connected, i.e., the interlayer resistance becomes much smaller than other series resistances.

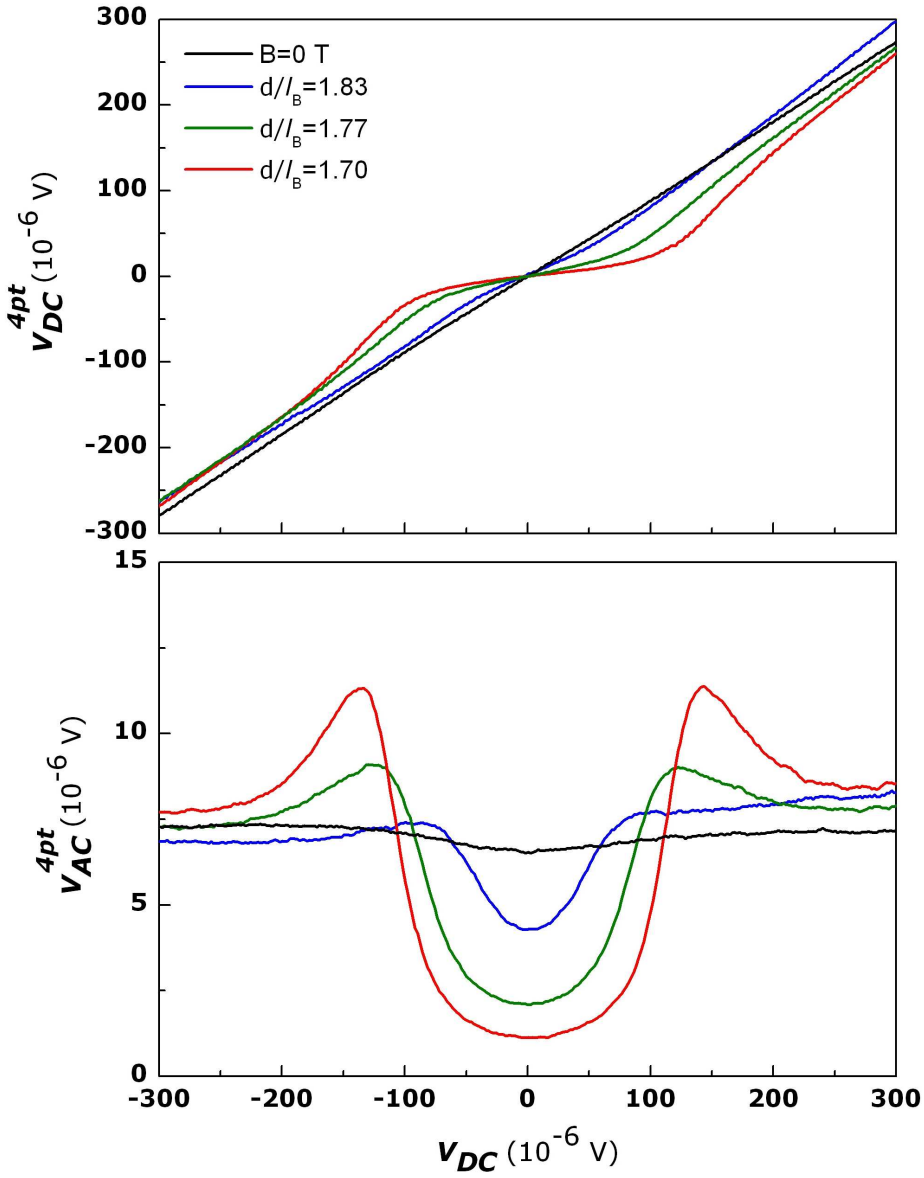

Figure 6.5: Measured 4-terminal AC and DC voltages plotted versus the 2-terminal (2pt) voltage V_{DC}. These voltages were simultaneously measured with the data presented in Figure 6.4. Further explanations can be found in the text. Sample 81653:210H.

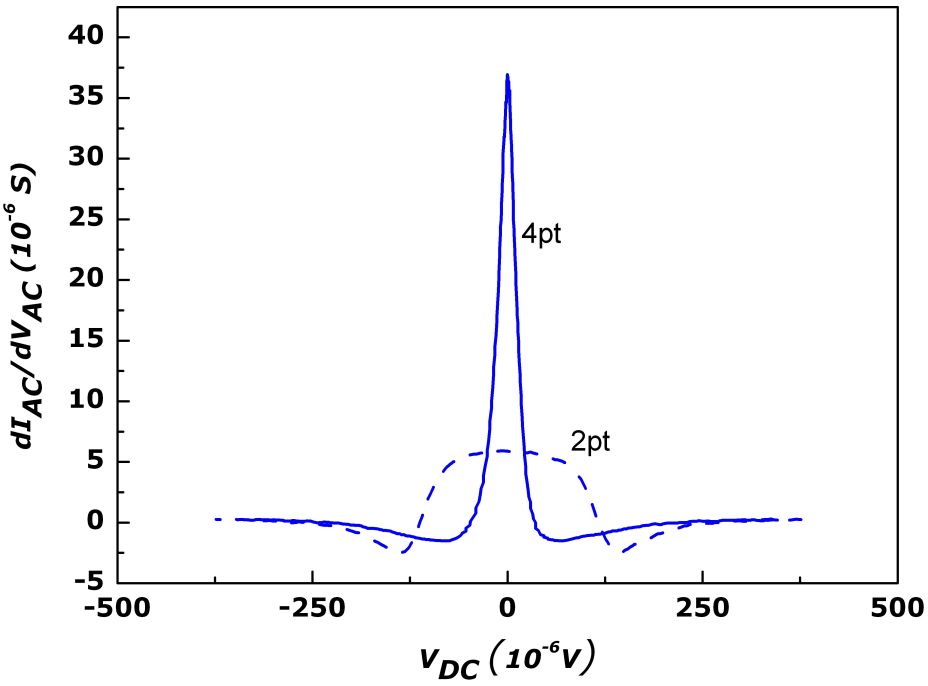

Figure 6.6: Differential conductance for $d/l_B = 1.70$ in a 2-terminal (2pt) and 4-terminal (4pt) representation. The 2pt curve shows dI/dV plotted versus the 2pt DC voltage V_{DC} as shown in Figure 6.4. For the 4pt curve, however, dV_{AC} is identical to the measured 4-terminal voltages V_{AC}^{4pt} from Figure 6.5. The resulting dI/dV is plotted versus V_{DC}^{4pt}. For simplicity the label to the x-axis remains unchanged. Sample 81653:210H.

6.4 Unmodulated DC Measurements

Using a sufficiently sensitive DC measurement setup, the tunneling experiment can be simplified by measuring the DC current directly. This DC current was detected by probing the voltage drop across a 10 kΩ resistor connected towards the common ground with a Stanford Research low noise preamplifier. The interlayer voltage was detected with an additional preamplifier or by repeating the interlayer bias sweep with the same amplifier which is then connected across the barrier. Note that rerunning a bias sweep usually alters the curve at large biases, i.e., the width of the curve around zero bias may slightly change. The DC voltage originates from an in-house built (low noise) ±10 V digital-analog converter and is sized down with a voltage divider.

Figure 6.7 shows an unmodulated DC measurement performed on sample 81653:146C at $d/l_B = 1.68$. The top panel illustrates the DC current as a function of the 2pt DC voltage. Consistent with the prior observation of an enhanced tunneling conductance dI_{AC}/dV_{AC} at small bias voltages, the DC current displays a relatively steep slope around zero bias which abruptly terminates when the current exceeds values of approximately -3.4 nA or +5.8 nA. The bottom panel of Figure 6.7 reveals a plateau in the probed 4-terminal DC voltage of nearly zero which accompanies the region where the current flow is enhanced. The most striking features in this plot are the existence of a critical voltage or current below which the 4pt interlayer resistance V_{DC}^{4pt}/I is very small and the prominent asymmetry. This asymmetry has occurred in all measured samples, however, it was especially strong in Corbino samples. This asymmetry will be discussed later in this chapter, however, it is owing to a hysteretic behavior.

For now, the focus will be on the observation of what appears to be a *critical current* rather than a critical voltage. The lack of prior experimental evidence of critical currents in bilayers at $\nu_{tot} = 1$, which had already been predicted by theory [Ros2005,Par2006], may be related to the AC modulation itself. In an AC modulated measurement when the DC voltage is large enough to obtain $I \approx I_{critical}$, the AC voltage will wobble the total current around $I_{critical}$ may lead to a smearing effect. Even though direct comparison between different samples is difficult (because it includes sample specifics and also temperature effects), comparing Figures 6.5 and 6.7 already indicates that even a small AC modulation alters the characteristics of the 4-terminal DC voltage.

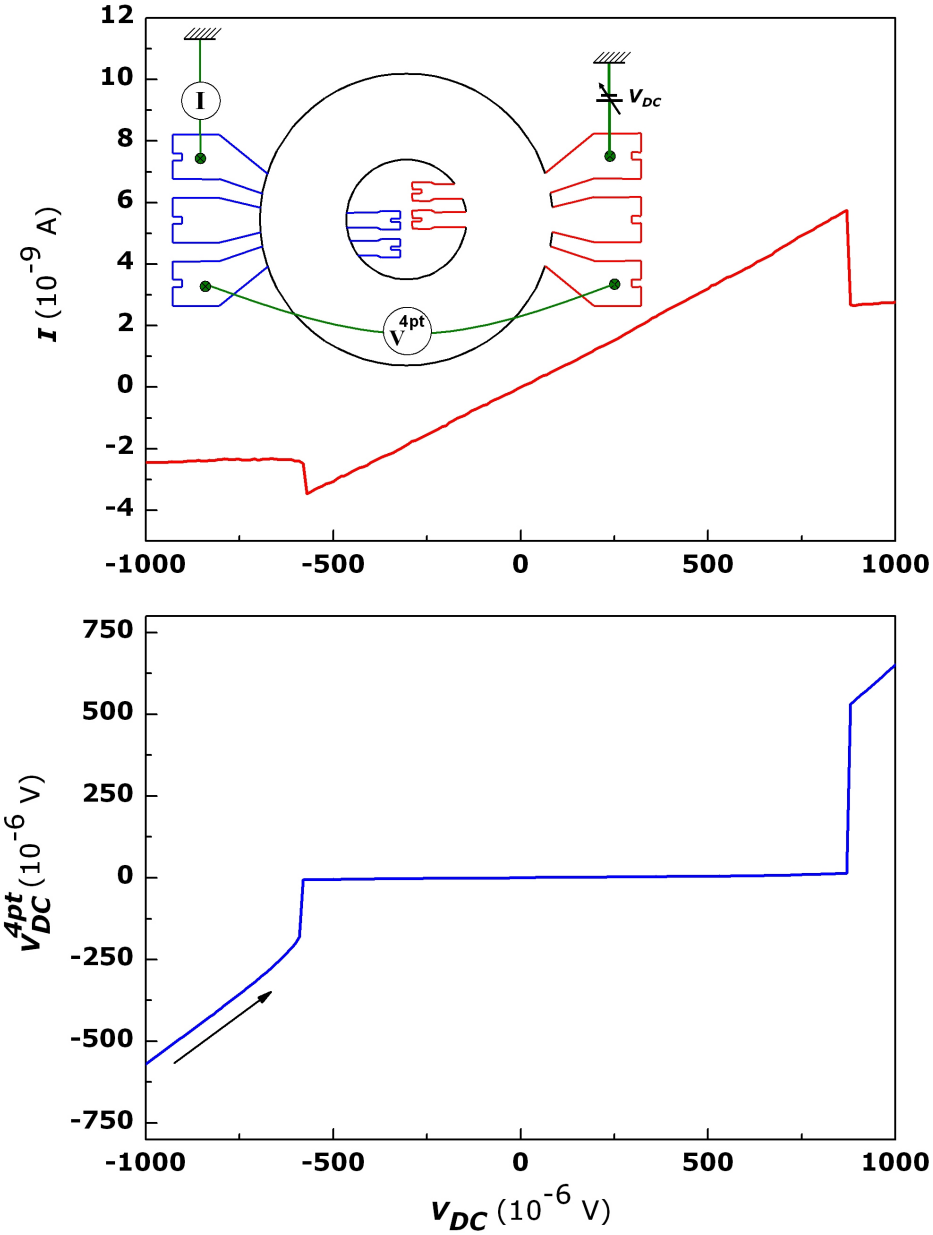

Figure 6.7: Current (top panel) and 4pt interlayer voltage (bottom panel) from an unmodulated DC measurement at $d/l_B = 1.68$ and T_{bath} ≈15 mK, on sample 81653:146C (I and V not measured simultaneously). Below a critical current of -3.4 nA or +5.8 nA, the interlayer voltage nearly vanishes. The arrow indicates the sweep direction of the 2pt voltage, i.e., from negative to positive values.

The Critical and Relevant Parameters

A naïve question is whether it is the current or the small but finite[4] four-terminal voltage which is "critical", i.e, which triggers the "quenching" of the tunneling enhancement? As the 4pt voltage remains small, the critical behavior appears to be related to the current which exceeds a threshold value. It should be noted that the critical behavior strongly depends on the temperature and probably also on external sources of interference such as HF radiation which may prematurely induce the quench. This means that repeated interlayer bias sweeps can yield slightly different critical values, making a direct comparison difficult. Nevertheless, when additional series resistances are introduced into the electrical circuit, the plateau which was found in Figure 6.7 will increases in width, however, it hardly affects the 4-terminal interlayer voltage or the current. This means that the 2pt DC voltage V_{DC} is in fact not a physical relevant parameter since the resistances cannot be controlled in experiment. Especially contact resistances may become fairly large under strong perpendicular magnetic fields and at low densities. Plotting the measured current and 4pt voltage as a function of 2pt DC voltage V_{DC} however allows to clearly resolve and indicate the critical currents and the regime of interlayer phase coherence. For that reason, this notation (while not physically relevant) will be used occasionally for some of the following experiments. Figure 6.8 presents the I/V curve from Figure 6.7 in its physical relevant representation of the current versus the 4-terminal voltage V_{DC}^{4pt}. This plot show a Josephson effect-like characteristic. The slope around zero bias is not infinite, its full width between $-I_{Critical}$ and $+I_{Critical}$ is about 18 μV.

These data resemble earlier reports [Spi2001] where however the maximal current was of order 20 pA instead. Depending on the sample and d/l_B, this is between 100...1000 times smaller than the critical current in the data presented in this thesis. The I/V characteristic in [Spi2001] was deduced from integrating the differential tunneling conductance data which may have masked the critical current behavior reported here. Even though the sample characteristics differ only marginally (QW/barrier/QW width in [Spi2001] is (18/9.9/18) nm which yields a comparable value of $\Delta_{S,AS}$, the effective single particle tunneling amplitude in our samples appears to be larger. Hence, it can be assumed that the different magnitudes of the maximal currents can be attributed to a different bare interlayer tunneling which strongly influences the tunneling anomaly at $\nu_{tot} = 1$ as discussed at the beginning of this chapter.

[4] Its value depends on the value of d/l_B and the temperature. For Figure 6.7 it is approximately $<$5...10 μV.

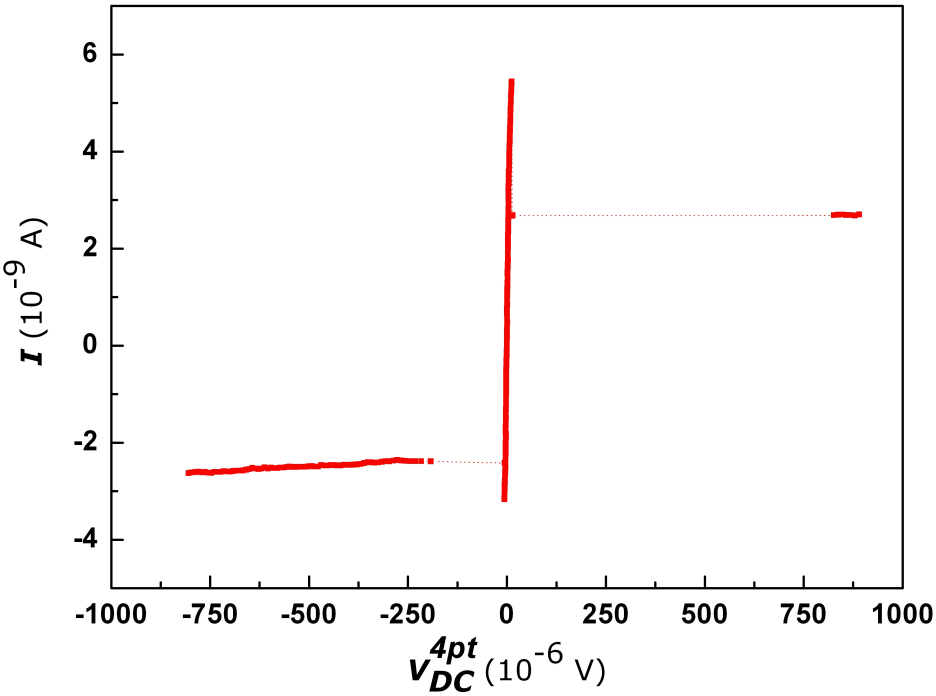

Figure 6.8: The current versus the 4-terminal voltage V_{DC}^{4pt} (data from Figure 6.7). The curve shows a Josephson-like characteristic. Only filled symbols are actual data points, the dotted lines are used to guide the eye.

Hysteresis and Asymmetry

The aforementioned prominent asymmetry in the data is related to a strong hysteresis[5] as shown in Figure 6.9 for $d/l_B = 1.56$. To distinguish between the critical points for both sweep directions, they are marked with u_1/u_2 (for the **u**psweep) and d_1/d_2 (for the **d**ownsweep). As Figure 6.9 shows, the hysteresis requires to compare the critical values at u_1 and d_1 and at u_2 and d_2 rather than within each sweep. The critical currents are then found to be nearly identical, i.e., -5.8 nA and +5.5 nA at u_1 and d_1 and -10.7 nA and +10 nA at u_2 and d_2. The origin of the hysteresis might be owing to a density effect[6] or energy dissipation/heating. When the interlayer bias is increased to values above zero (coming from negative values for instance) the quasiparticle flow from one layer to the other layer increases. Even though both layers are in near chemical potential equilibrium, an incident single electron which is transferred into a quasiparticle will leave a defect in one layer and has to find a interstitial position in the other layer, which is "easy" owing to the interlayer phase coherence. However, with increasing interlayer bias, when more and more quasiparticles tunnel, the system cannot relax rapidly enough to minimize the total Coulomb energy. This process may eventually dissipate enough energy to destroy the quasiparticle tunneling altogether. Dissipation also could originate from the incident single electrons coming from the leads. Since the contact arms are a regular quantum Hall system, they might exhibit "hot spots" [Kla1991] at the interface to the correlated phase. If the filling factor of the contact arms is close to the regular filling factor 1, the Joule heating at these hot spots is about $\rho_{xy} \cdot I^2$, where $\rho_{xy} = h/e^2$ is the Hall resistivity of the contact arm. The inset in bottom panel of Figure 6.9 shows a blow-up around zero 4pt voltage. As this inset indicates, the 4pt interlayer bias increases linearly only exactly between the points u_1 and d_1. Beyond these two points, the measured voltage increases with (what appears to be) a quadratic dependence before at even higher 2pt bias voltages, the enhanced tunneling quenches. Strongly reducing the sweep rate of the bias voltage can flatten the curve at points u_2 (d_2). As previously pointed out, if a bias-sweep is repeated without having changed any other parameter, the critical points $u_{1/2}$, $d_{1/2}$ generally may lie at larger or lower 2-terminal voltages, however, changes were found to be usually stronger for u_2 (or d_2) than for u_1 (or d_1).

[5] This hysteresis was found to be very pronounced in the Corbino device 81653:146C as shown here and weak in Hall bars. However, since only one Corbino sample was examined in these tunneling experiments, it may as well be sample-specific rather than geometry-dependent.

[6] If density inhomogeneities exist, some parts of the ring may be more strongly correlated than others. Depending on the sweep direction, these areas may induce a quench of the enhanced tunneling.

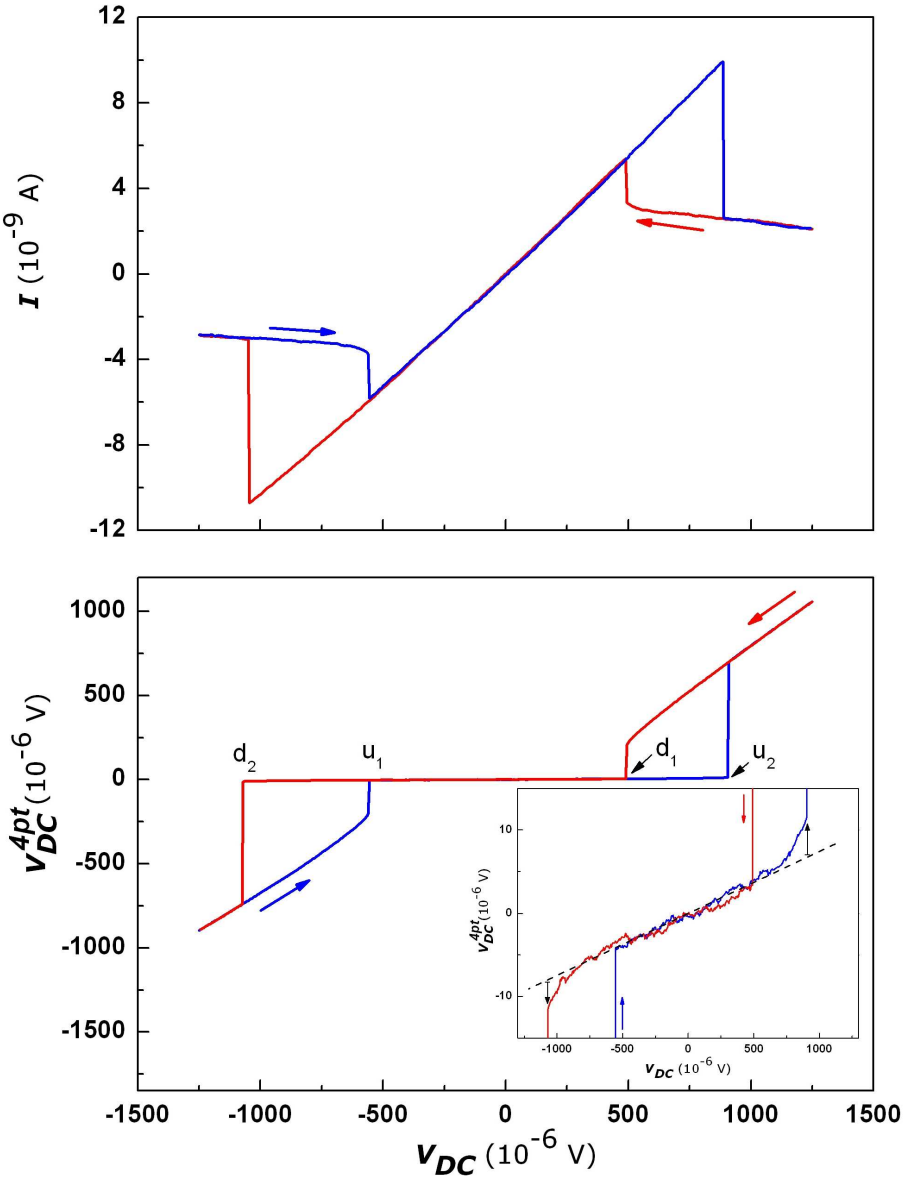

Figure 6.9: The observed asymmetry is owing to a large hysteresis. The top panel shows the current and the bottom panel the voltage for both sweep directions (current and voltage were not measured simultaneously). The critical currents at u_1 and d_1 (-5.8 nA and +5.5 nA) and at u_2 and d_2 (-10.7 nA and +10 nA) are nearly identical. The inset is a blow-up around zero 4-terminal voltage. Prior to reaching points u_2 and d_2 the 4-terminal voltage increases quadratically. Sample 81653:146C. Same measurement setup as in Figure 6.7, however at $d/l_B = 1.56$.

The Evolving $\nu_{tot} = 1$ State

After having discussed the properties of the tunneling characteristic, Figure 6.10 now demonstrates how the tunneling process evolves upon reducing the ratio d/l_B from high to low values, i.e., upon reducing the electron densities in both layers simultaneously and adjusting the magnetic field correspondingly. These data were produced on sample 81653:146C where the interlayer bias was again applied between the two outer circumferences of the upper and lower layer. Moving from high to low values of d/l_B, plateaus in the 4pt voltage appear which progressively take on lower values and become broader. At the same time, the critical currents grow. As pointed out earlier, with decreasing d/l_B, it becomes progressively harder to impose any electrochemical potential difference between the layers owing to the growing interlayer phase coherence. So it requires progressively larger 2pt voltages to induce a quench of the enhanced tunneling. This behavior is reminiscent of the data on interlayer drag that were presented in chapter 5. A puddle model was introduced which assumes a fragmentation of single condensates in the active region for large and intermediate values of d/l_B. Thus, if there are areas which display no or only weak interlayer phase-coherence, they will thus dissipate energy in interlayer tunneling experiments and yield a large 4pt interlayer resistance $R^{4pt} = V_{DC}^{4pt}/I$. For the lowest d/l_B, however, the phase-coherence has seized the entire sample so that the 4pt interlayer resistance R^{4pt} has a value of only about 200 Ohms at $T_{bath} \approx 15$ mK. When the critical current is exceeded, R^{4pt} is nearly of the same magnitude for all d/l_B. This suggests that the condensate is destroyed and the current is maintained by bare electron tunneling given by $\Delta_{S,AS}$ which is independent of the coupling parameter. However, it is not clear if the condensate and its phase coherence is destroyed entirely or only in certain areas of the sample, such as the edges where the current is expected to flow. Note that the observed asymmetry is particularly pronounced for low d/l_B. This is owing to the previously discussed hysteretic behavior. The enhanced noise around $V_{DC} = 0$ originates from the noise in detecting small voltages, as the voltage drop across a 10 $k\Omega$ resistor is measured.

Figure 6.11 re-evaluates the data from Figure 6.10. The top panel plots the current versus the 4-terminal voltage for three representative values of d/l_B to indicate how the characteristic changes from a Josephson-effect like curve to a regular linear I/V characteristic. The bottom panel shows the value of the critical currents plotted versus the coupling parameter d/l_B. Since the bias sweeps were performed only in one direction, the critical currents display an asymmetry (owing to the hysteresis). Although there are small deviations, the trend is linear as indicated by the dashed lines (best linear fits). When extrapolated the intersection of the dashed lines with the dotted horizontal line (i.e., no current) should indicate the phase transition point which lies between a d/l_B of

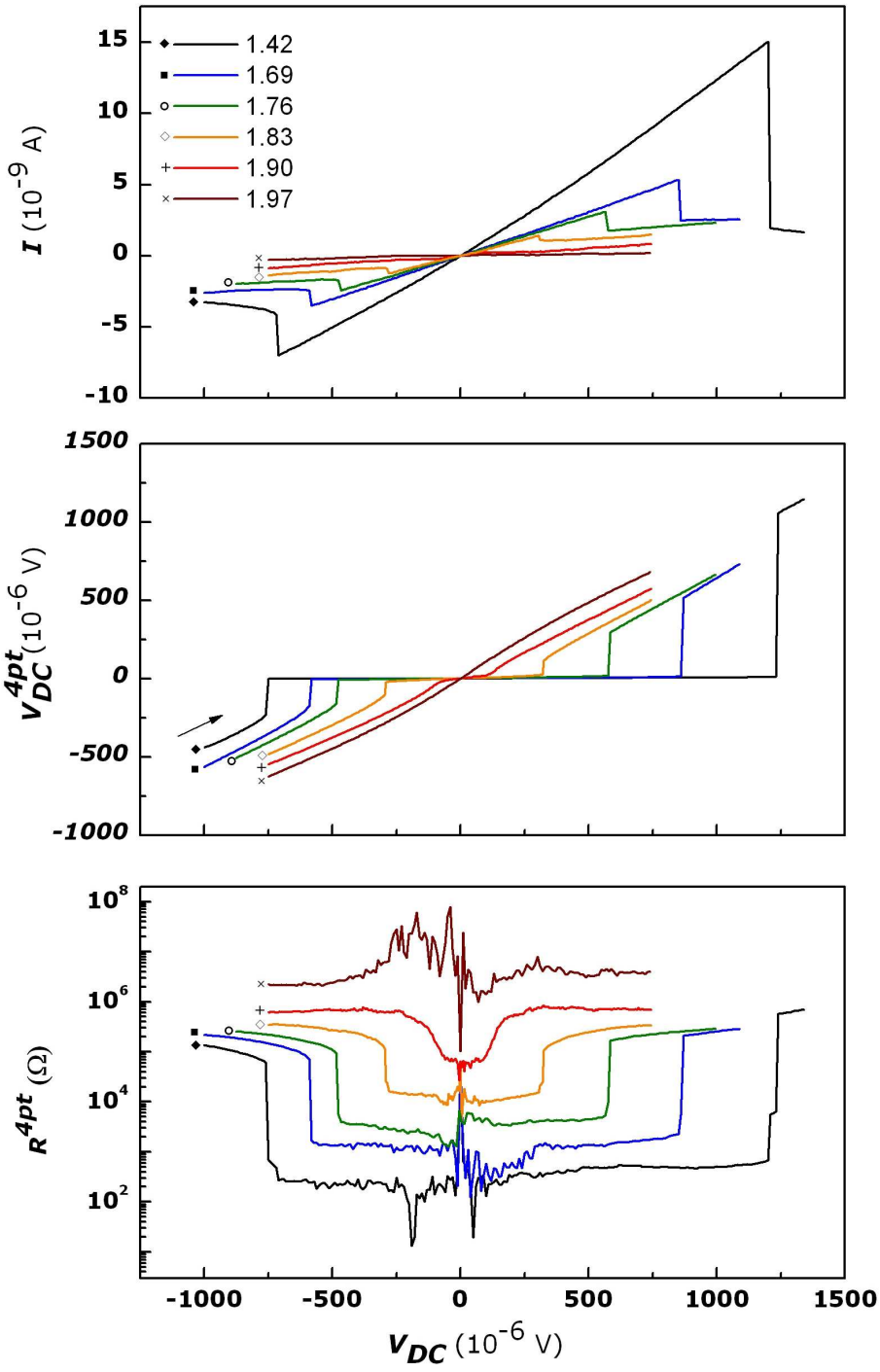

Figure 6.10: The top panel plots the measured tunneling current versus the 2pt interlayer bias V_{DC} for a set of six different d/l_B. The mid panel shows the probed 4pt voltage V 4pt which was not measured simultaneously, and the bottom panel illustrates the calculated 4pt interlayer resistance. Same setup as in Figure 6.7, however, current and voltage contacts were exchanged. Sweep direction always from negative to positive values. Sample 81653:146C.

approximately 1.85 and 1.90. However, as very small tunneling currents may flow between both layers in the uncorrelated state the curve should saturate at larger $d/l_B \gtrsim 2$.

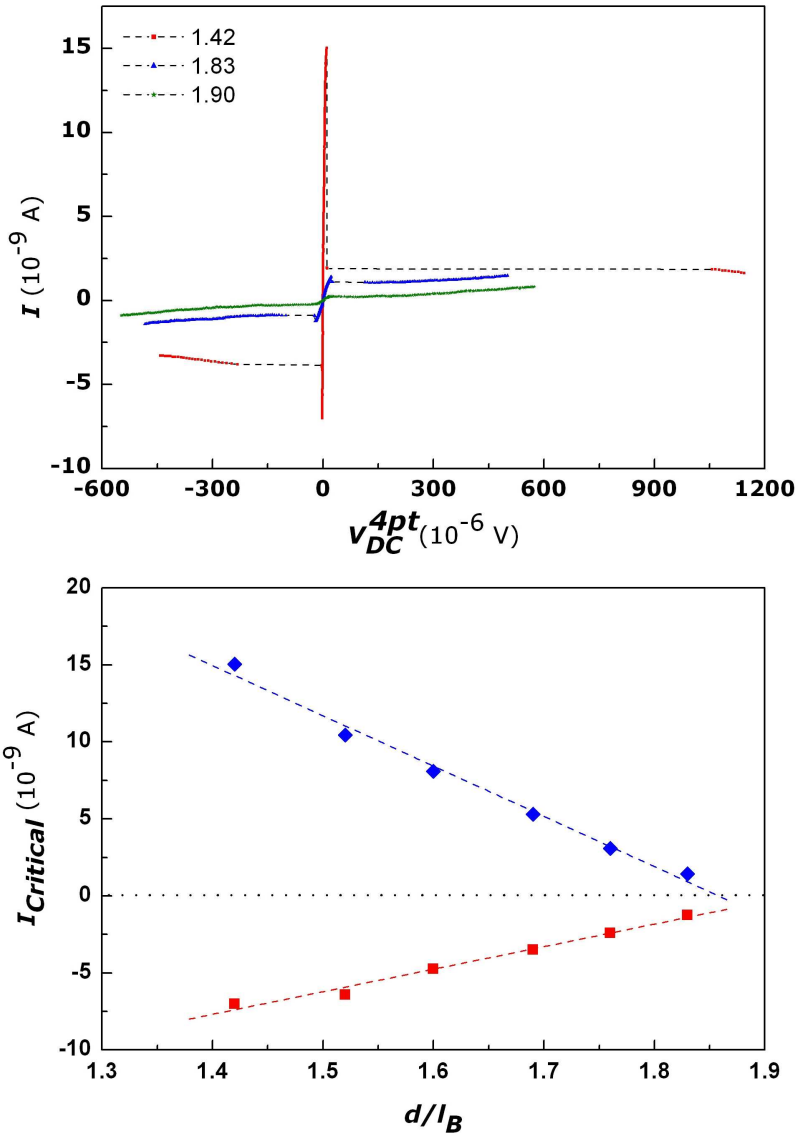

Figure 6.11: Top panel: current versus 4-terminal voltage for three representative d/l_B. With decreasing coupling parameter, the characteristic changes from Josephson-like to Ohmic. Bottom panel: critical currents versus the coupling parameter d/l_B. The dashed lines are best linear fits. Their intersection with the horizontal (dotted) axis may indicate the phase transition point. This plot uses the data presented in Figure 6.10 along with additional measurements (not shown), i.e., here the sweep direction is from negative to positive values as well. Sample 81653:146C.

Tunneling Peculiarity at $\nu_{tot} = 1$

As Figure 6.3 already implies, which had shown only 2-terminal (AC modulated) measurements, the tunneling anomaly is a peculiarity and only occurs close to a total filling factor of 1 and at no other filling factor. Figure 6.12 shows a DC measurement for a constant electron density $n_{tot} \approx 3.94 \cdot 10^{14} m^{-2}$ ($d/l_B = 1.42$ at $\nu_{tot} = 1$), performed on sample 81653:210H, i.e., a Hall bar, at $T_{bath} \approx 25$ mK. It plots the current versus the 4-terminal interlayer voltage and the inverse total filling factor. As this Figure demonstrates, the strong reduction of the 4-terminal interlayer voltage along with the current increase (which yields a Josephson-effect like characteristic) is only occurring in the direct vicinity of a total filling factor of 1. At all other filling factors, the Coulomb blockade suppresses/reduces the current flow around zero bias, and even at zero magnetic field, the maximal current is still about 14 times smaller than at $\nu_{tot} = 1$.

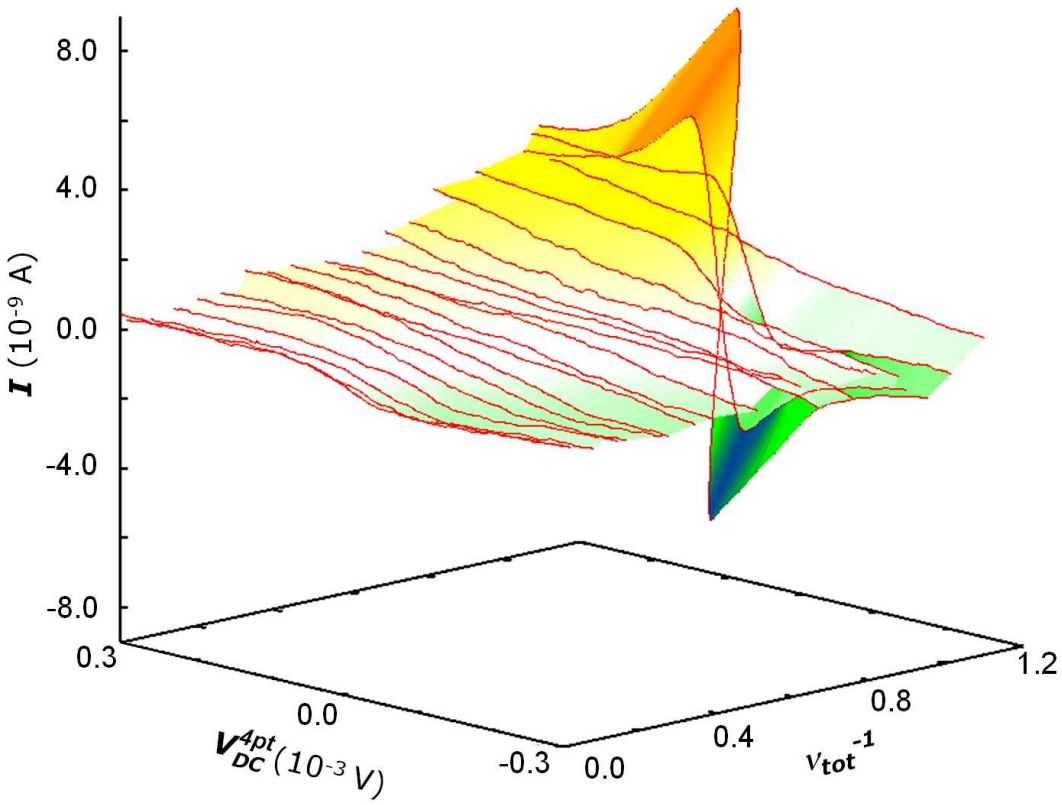

Figure 6.12: 3D plot of the current versus the 4-terminal interlayer voltage V_{DC}^{4pt} and the inverse total filling factor. Only close to total filling factor 1, a Josephson-effect like characteristic emerges. Sample 81653:210H.

Identifying the Tunneling Region

The question where exactly the enhanced tunneling may take place can be addressed by performing the tunneling experiment on a Corbino geometry when a current is sent from the outer perimeter of one layer to the inner perimeter of the adjacent layer, as shown in the inset of Figure 6.13. The experimental data confirm the results of the magneto-transport experiments presented in chapter 5 which had demonstrated an energy gap at total filling factor 1. Unlike tunneling between the same sample perimeter, now the 4-terminal interlayer voltage does not vanish anymore, i.e., 2-terminal and 4-terminal voltage are nearly identical, and no critical currents can be found. These data imply that the strongly enhanced quasiparticle tunneling process must occur in the vicinity of the sample edges as the gapped bulk does not permit any quasiparticle/electron transport across the annulus.

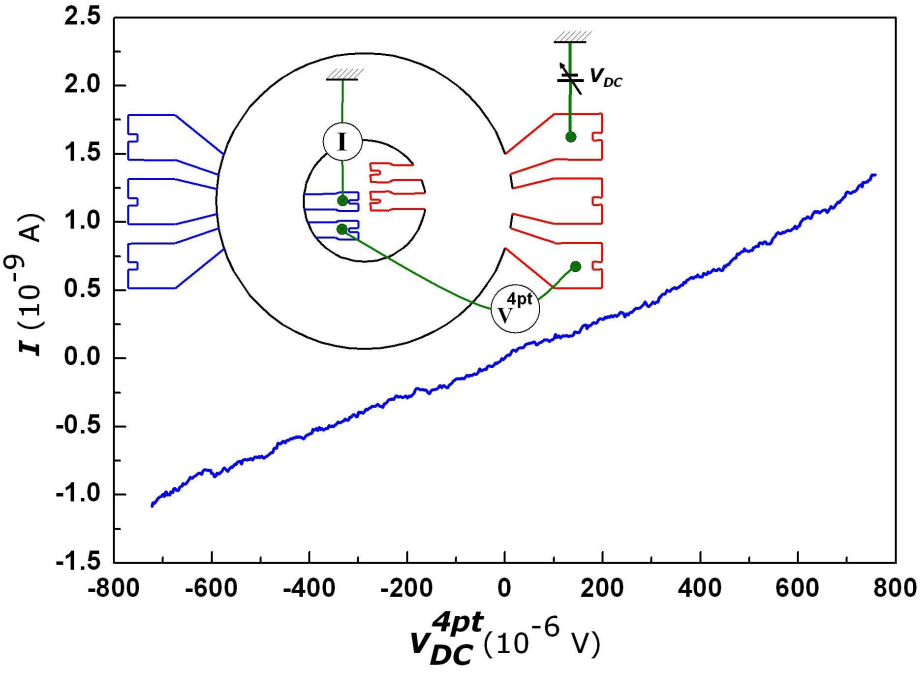

Figure 6.13: I/V characteristic (current versus V_{DC}^{4pt}) for tunneling between opposite perimeters at $d/l_B = 1.56$. Current and voltage were not measured simultaneously. No transport across the gapped bulk is possible. Sample 81653:146C.

If this quasiparticle tunneling is occurring in the vicinity of the sample edges, then the question is if there should be a dependence of tunneling conductance on the length of the edges. This possibility will be discussed as an outlook in the last part of this chapter.

Residual Interlayer Voltage

The question of the lowest obtainable 4pt resistance and/or its accuracy is directly related to the question which factors or parameters influence the 4-terminal voltage. In addition to the temperature-activated behavior, it is relevant where exactly the potential is probed because residual resistances from ordinary quantum Hall systems might come into play. These ordinary quantum Hall systems can either be the contacts arms or even parts of the active region which are only weakly coupled (puddle model). Any current I that crosses the boundary of such a two-dimensional electron system under quantum Hall conditions will produce a voltage difference across the contact of the order of the Hall voltage $h/e^2 \cdot I$ ($\approx$25 μV at $I = 10^{-9}$ A). Probing the voltage between opposite edges of the two layers should thus generally include a Hall component to the interlayer voltage as Figure 6.14 suggests. Since the sign of the Hall voltage depends on the sign of the magnetic field B, it should be possible to account for its influence by inverting the magnetic field. This effect can best be seen in the Hall bar geometry.

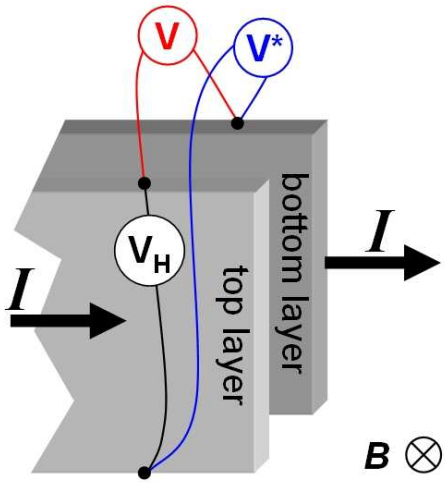

Figure 6.14: Cartoon of different interlayer potential probing in a pseudo 3D view. The voltage probe V_H will directly measure the Hall voltage $V_H = \frac{h}{e^2} \cdot I$. The probe V^* will measure this Hall component as well, since it probes the interlayer voltage across the Hall bar, whereas only V directly yields the interlayer voltage.

Figure 6.15 shows the result of a systematic investigation of this potential probe dependence, performed on sample 81653:210H at $d/l_B = 1.42$ and $T_{bath} \gtrapprox 25$ mK. On the left-hand side, the simplified setup is shown, where **S** and **D** mark the source (voltage source) and drain (ground) contacts. The right-hand side shows the current plotted versus the 4-terminal voltage.

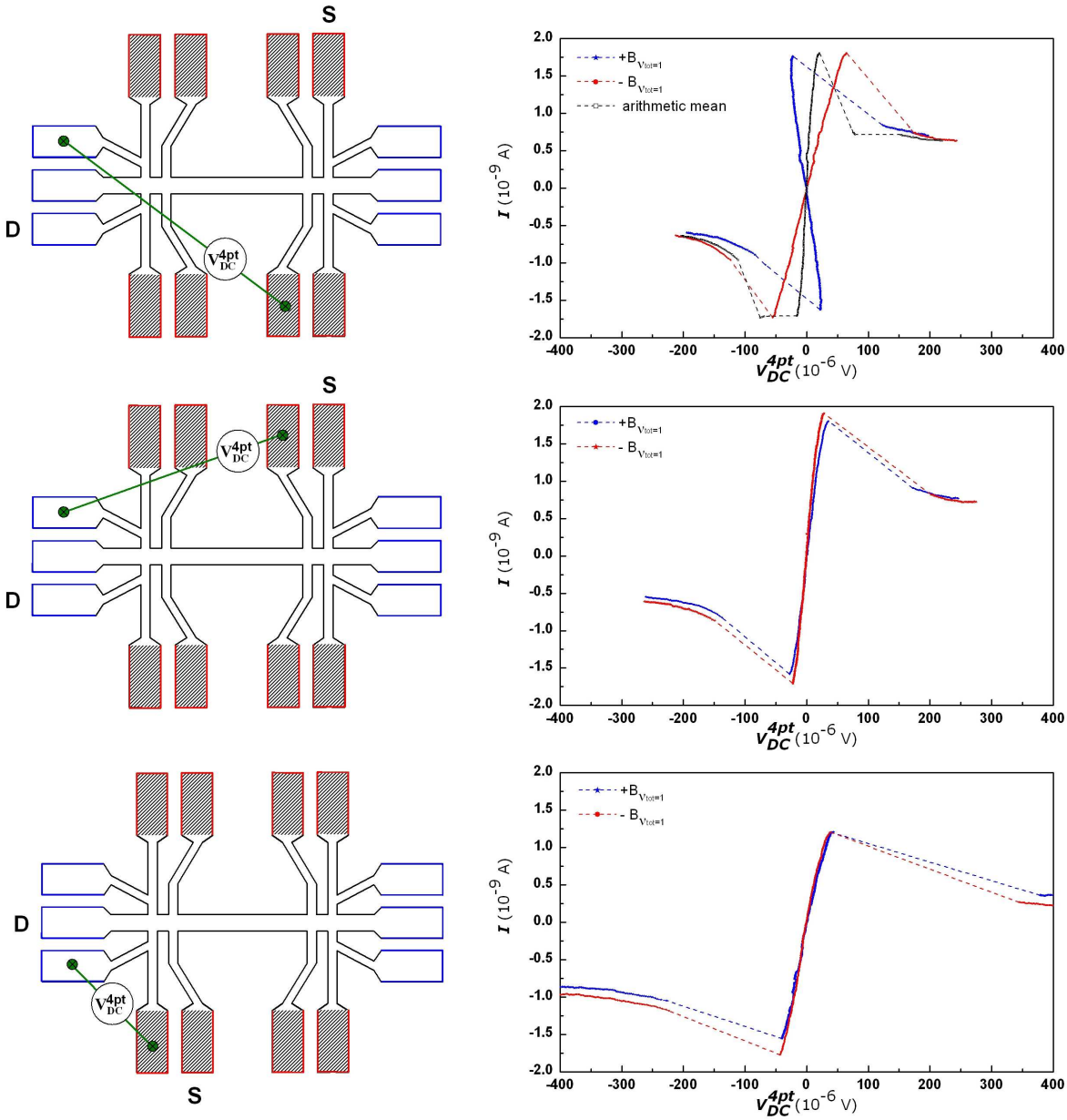

Figure 6.15: Dependence of the 4-terminal voltage on the potential probes. The left-hand side shows the experimental setup, where **S** and **D** mark the **s**ource and **d**rain contacts. On the right-hand side, the 4-terminal voltage is shown. When the voltage is probed on opposite sample edges, the slope around zero bias depends on the polarity of the magnetic field. Sample 81653:210H at $d/l_B = 1.42$ and $T_{bath} \gtrapprox 25$ mK.

As the top-panel clearly shows, when the interlayer voltage is probed between opposite (Hall) edges, the 4-terminal voltage for $I < I_{critical}$ is not only strongly reduced but also sign-inverted. The current, on the other hand, does not display any significant dependence on the polarity of the magnetic field in all cases. Changing the polarity of the magnetic field from $+B_{\nu_{tot}=1}$ to $-B_{\nu_{tot}=1}$ inverts the slope around zero bias again. Nevertheless, the mean value calculated from the two curves at $+B$ and $-B$, does not completely cancel out V_{DC}^{4pt} as one may expect. This might be caused by longitudinal resistance components, if the current flows through dissipative regions. The dissipation could originate from finite temperature effects. The occurrence of dissipative regions would indeed explain the larger 4-terminal voltage in these data (<50...100 μV), but not the behavior of its slope around zero bias.

On the mid panel of Figure 6.15, the interlayer voltage was probed on the same side of the sample but spatially separated. This measurement shows that the 4-terminal interlayer voltage at $\nu_{tot} = 1$ is *B-invariant*, i.e., it does not depend on the polarity of the magnetic field. Even probing the voltages directly atop of each other (bottom panel) yields a finite 4-terminal interlayer voltage. This could be an intrinsic property of the system or directly related to a temperature-effect.

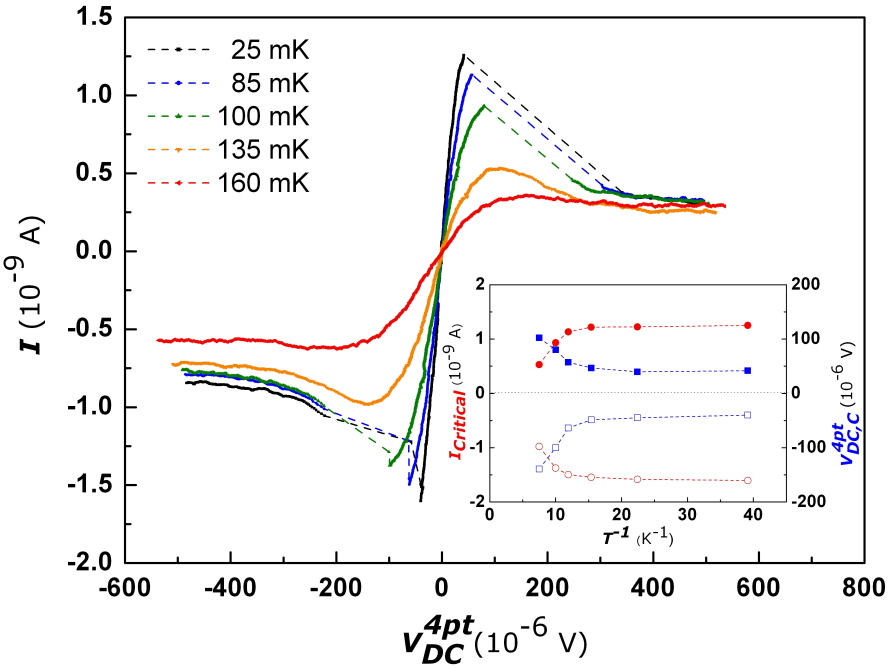

Figure 6.16: Temperature-dependence of the 4-terminal voltage and current (measured simultaneously). The insets show the critical currents and the residual voltages $V_{DC,C}^{4pt}$ measured at $\pm I_{Critical}$ versus the inverse temperature. Sample 81653:210H at $d/l_B = 1.42$.

However, by increasing the temperature it can be observed how the slope around zero

bias flattens as it would be for increasing the coupling parameter d/l_B. Figure 6.16 shows how the tunneling characteristic changes upon increasing the temperature. As the bottom panel indicates, the residual voltage does not seem to change much below 50 mK, so it is questionable if it will vanish altogether for $T \rightarrow 0$ K. The insets illustrate the re-analyzed data by plotting critical currents and the voltage $V_{DC,C}^{4pt}$ versus the inverse temperature, where $V_{DC,C}^{4pt}$ is the 4-terminal voltage at $I_{Critical}$. It should be noted that in contrast to the Corbino measurements the asymmetry in the critical behavior appears to be reversed, i.e., the negative critical current is larger than the positive one for a bias upsweep. Whether this a sample-specific behavior or owing to some density fluctuation effect is not clear.

Champagne *et al.* [Chm2008] have investigated the tunneling characteristic of the strongly correlated $\nu_{tot} = 1$ quantum Hall state as a function of the layer separation, temperature, and interlayer charge imbalance. They found strong evidence for a finite temperature phase transition. The transition temperature is dependent on both the layer spacing and charge imbalance between the layers. Experiments typically show a *continuous* transition between the two phases. However, it is possible that disorder (e.g., static density fluctuations) might smooth out weakly discontinuous observables via phase separation near the critical point [Chm2008].

As pointed out at the beginning of this chapter, identical densities in the two layers were produced by using the top and bottom field gates. These matched densities, however, are imbalanced upon imposing an interlayer bias, which was not compensated for in the measurements presented above. Since the effective 4-terminal interlayer bias was found to nearly vanish for $I < I_{critical}$ at $\nu_{tot} = 1$, no dramatic differences in the tunneling characteristic are to be expected around zero bias anyway. Nevertheless, it is possible to adjust the voltages to the front and back gate while sweeping the interlayer bias to keep the electron density in each of the two layers constant. Originally, these adjustments were performed on a Corbino device, where aside from a reduction of the plateau width[7] by ca. (10-15) % and slightly reduced critical currents (< 2 %) no significant changes were found. As discussed above, in Hall bars the 4-terminal voltage depends on the location of the voltage probes. When the voltages are probed between opposite sample edges and the gate voltages are adjusted, then the same observation as in Corbino samples was made while the (inverted) slope around zero bias (see Figure 6.15) remained nearly unchanged. However, when the voltages are probed at the same edge while adjusting the gate voltages, the 4-terminal interlayer voltage nearly vanishes completely like in Corbino devices. Figure 6.17 compares the 4-terminal I/V characteristics of an adjusted and unadjusted measurement on sample 81653:210H at $d/l_B = 1.42$. The voltages were

[7]The plateau that appears if the 4-terminal voltages (and currents) are plotted versus the 2-terminal voltage.

probed as shown on the mid panel of Figure 6.15. For the adjusted measurement the 4-terminal voltage remains below the noise level, which is about 2 μV, until the current exceeds about 0.5 nA (in sweep direction).

Even though the imbalance should not disrupt the total number of excitons because the number of holes and electrons remains constant, it does disrupt other parts of the system which may explain the differences between adjusted and unadjusted measurements. It should be kept in mind that the interlayer bias is not directly applied to the active region that exhibits interlayer phase-coherence but to contacts arms which are at some other filling factor (certainly close to 1). The interlayer bias will thus shift the filling factors of these two contacts arms, one to higher and the other one to lower fillings. This may have some effect at the boundary to the active region. On the other hand, a density imbalance may introduce dissipation because now there are more electrons in one layer than in the other. When an electron is designated to tunnel it comes from an initial state of high energy from a layer where there is "much space" to a final state of lower energy where

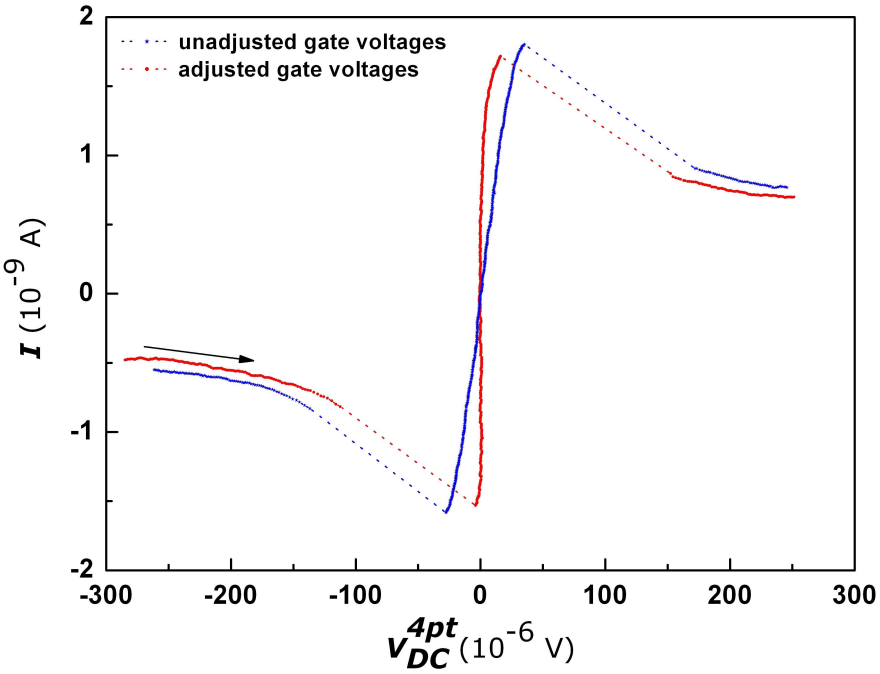

Figure 6.17: Comparison of the 4-terminal I/V characteristic for a tunneling measurement where the gate voltages were adjusted while sweeping the interlayer bias and a measurement where the gate voltages were kept constant (current and voltage were measured simultaneously). For the adjusted measurement the 4-terminal voltage remains below the noise level (about 2 μV) until the current exceeds about 0.5 nA. The dashed lines connect actual data points. Sample 81653:210H at $d/l_B = 1.42$.

there is "not so much space anymore" which may make it much more difficult for this system to relax, *despite* the existence of interlayer phase-coherence. Also, an imbalance can be associated with an out-of plane pseudo-spin and the formation of merons (vortices in the pseudo-spin field) which dissipate energy [Roo2008].

6.5 Magneto-Transport versus Interlayer Tunneling

The previously investigated temperature-dependence is of certain relevance. If at lowest temperatures (and low d/l_B) the 4-terminal interlayer resistance is largely reduced, then identical voltages across both layers are trivially explainable, whether it is the case in Corbino rings or Hall bars.

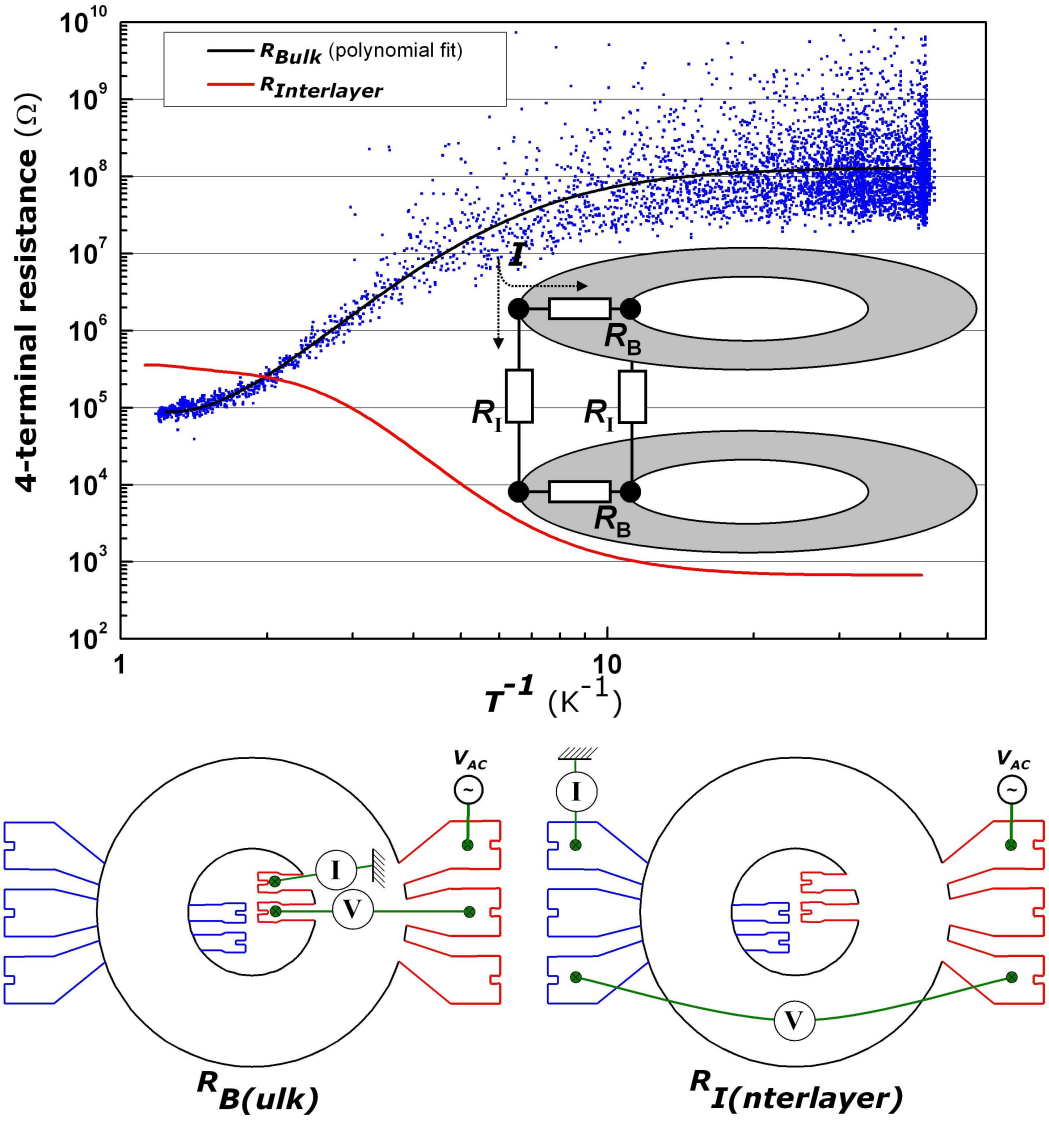

Figure 6.18: Comparison of the 4-terminal intralayer (bulk) and interlayer resistance versus the inverse temperature. For temperatures below 500 mK, the interlayer resistance is smaller than the resistance of the bulk. The inset shows a simple resistor model to account for the data. Details can be found in the text. At the bottom, the two setups are shown that were used to determine R_I and R_B. Sample 81653:146C at $d/l_B = 1.56$.

Figure 6.18 compares two temperature-dependent AC measurements performed on a Corbino device at total filling factor 1 with $d/l_B = 1.56$. The first measurement shows the 4-terminal resistance of the bulk (the intralayer resistance) as a function of the inverse temperature T^{-1}. Owing to the large noise in the data (blue dots are actual data points), the black curve is a polynomial fit to emphasize the trend of the data. The second measurement which was performed directly afterwards illustrates the 4-terminal interlayer resistance. The corresponding measurement setups are schematically shown below. The inset in Figure 6.18 shows a simplified resistor model, where the intralayer resistance R_B and the interlayer resistance R_I are represented by their electric symbols. This model is not to be taken literally, since it implies that transport and tunneling is only occurring in a certain region. More correctly, these resistors should be distributed all over the annulus. At lowest temperatures, the bulk is highly resistive, i.e., $R_B \gg R_I$, so any current I fed in by the current contact at the outer edge will simply flow across the barrier. Probing the voltages between inner and outer edge thus yields the same voltage for drive and drag layer as shown in the drag experiments discussed in chapter 5. It should be emphasized that the magneto-transport properties are influenced by the large enhancement of the quasiparticle tunneling and not by regular electron tunneling.

With increasing temperature, however, this quasiparticle tunneling slowly subsides and the (excitonic) energy gap at the Fermi level diminishes. This will fundamentally change the transport properties of the system because it progressively allows regular electron transport to occur across the annulus while quasiparticle transfers across the barrier decreases. As quasiparticle tunneling remain a dominant process up to about 500 mK, where both curves cross, it is not surprising that identical voltages were found in magneto-transport experiments up to 250 mK as shown in chapter 5. Between approximately 200 mK and 50 mK, the 4-terminal interlayer resistance decays nearly exponentially, where $e^{-0.7/T}$ gives a fairly good fit to the data within this temperature range. The energy of 0.7 K is essentially identical to the (temperature-activated) gap energy that can be deduced from the longitudinal resistivity ρ_{xx} in Hall bars [Wie2005] from another wafer. Since in Hall bars V_{xx} is measured at the edge as well (only in one layer, though!), the energy gap deduced here does not differ.

6.6 Alternative Tunneling Experiments

The magneto-tunneling and magneto-transport experiments presented so far have shown that at a total filling factor of one, the 4-terminal interlayer resistance is fairly small. However, largely enhanced tunneling appears to be limited to the vicinity of the edges. Using the notion of a Bose condensation of excitons as a base, a rudimentary model of the potential $\Phi(r)$ which is experienced by the quasiparticles and the interlayer excitons (which open up a correlation gap) can be developed. In this model, the excitons are confined to the bulk and experience an infinite potential towards the edges, the quasiparticles on the other hand cannot (completely) penetrate the bulk. These ideas are considered in Figure 6.19.

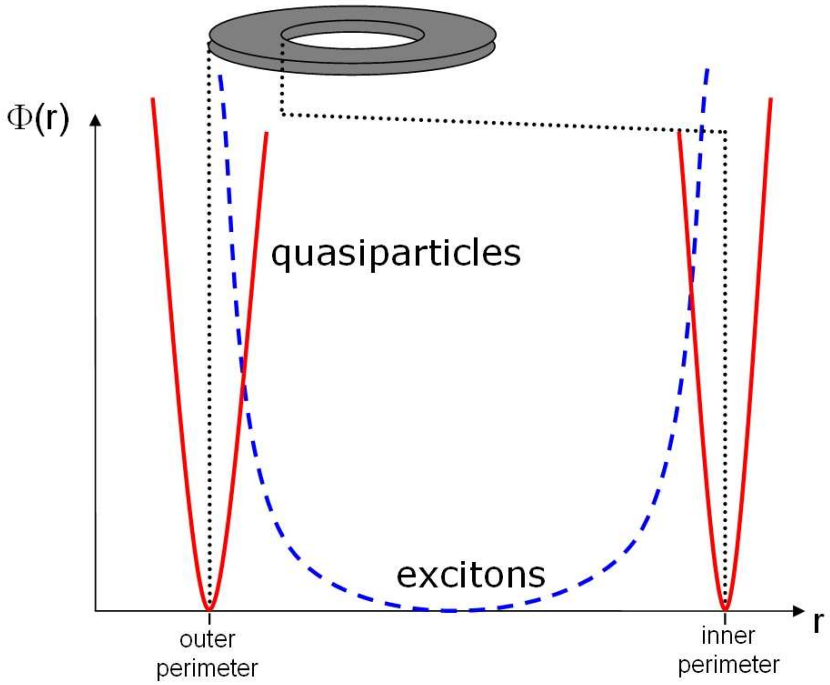

Figure 6.19: Rudimentary model of the potential $\Phi(r)$ which is experienced by the quasiparticles near the edges and the excitons in the bulk. While the excitons are confined to the bulk and experience a large potential near the edges (blue dashed line), the quasiparticles cannot penetrate the bulk (red solid line).

The question thus is if the excitons in the bulk are completely inert or if they can be excited to a steady state excitonic (super)current? Even though the inner and outer edges of a Corbino ring are separated by the bulk, quasiparticle tunneling at both circumferences should occur coherently as phase-coherence should exists across the active sample area. Keeping this in mind, tunneling can simultaneously be investigated at both perimeters of a Corbino ring when the system is set up as in a drag experiment. In this alternative

approach to tunneling at $\nu_{tot} = 1$, a variable resistor R_{Load} is applied between the same contacts that are used to measure the drag voltage, i.e., both edges of the drag layer are connected via a resistive bridge. For future reference, this setup is referred to as *the load configuration/setup*. For $R_{Load} \to \infty$ the system behaves as in a regular drag experiment. However, upon slowly decreasing R_{Load} from ∞ to 0 Ohms, a current I^* begins to flow through the bridge. This current $I^* = V^*/R_{Load}$ is identical to the current I which simultaneously starts to flow in the circuit of the drive layer. The results of this experiments are shown in Figure 6.20 for d/l_B=1.58. The top panel illustrates the current in the drive and drag circuit and the bottom panel the drive voltage as a (log) function of R_{Load}. Note that for $R_{Load} \to 0\ \Omega$, $V^* \to 0$ V, however, the drag voltage itself, if measured across another pair of contacts, remains finite and identical to the drive voltage (not shown here).

The limiting factor in this load configuration are the contact resistances which are in series to R_{Load}. Low densities (and consequently low d/l_B) may lead to larger series resistances, which then limit the current through the resistive bridge and consequently the current in the drive circuit and the reduction of the corresponding voltages. Note that if the grounding to the bottom layer is removed, the behavior does not significantly change. However, since the drag layer would float at an arbitrary potential once the correlation is broken, it is kept grounded at all times.

The quasiparticle tunneling at both edges is argued to induce excitonic condensate current in the bulk [Su2008]. Figure 6.21 tries to account for this model. Every incident single electron on the left side of the top layer is changed into a quasiparticle. This quasiparticle will launch an exciton in the bulk, and to conserve total charge in both layers a quasiparticle is reflected back into the leads of the bottom layer in an Andreev reflection-like process. Here it is assumed that quasiparticle flow across the sample is negligible. In this picture, it follows that $I_L = I_{TL} + I_{BL}$ is the exciton supercurrent emitted from the left side of the sample. If the inner and outer circumference of the bottom layer are physically connected over a sufficiently small resistance, it offers a short cut path across the gapped bulk for reflected single electrons. Once having passed that bridge, each electron will by itself undergo the same process of quasiparticle tunneling at the right side of the sample where $I_R = I_{TR} + I_{BR}$ is the exciton supercurrent absorbed on the right side. That means that condensate currents are induced by *quasiparticle counterflow currents* as they are of opposite direction on the two sample edges. The large potential difference between inner and outer edge imposed by the leads between TL and TR is the driving force for this exciton current. The steady state condensate currents are possible only when the two quantities of emitted and absorbed currents are equal [Su2008], i.e., $I_L = I_R$.

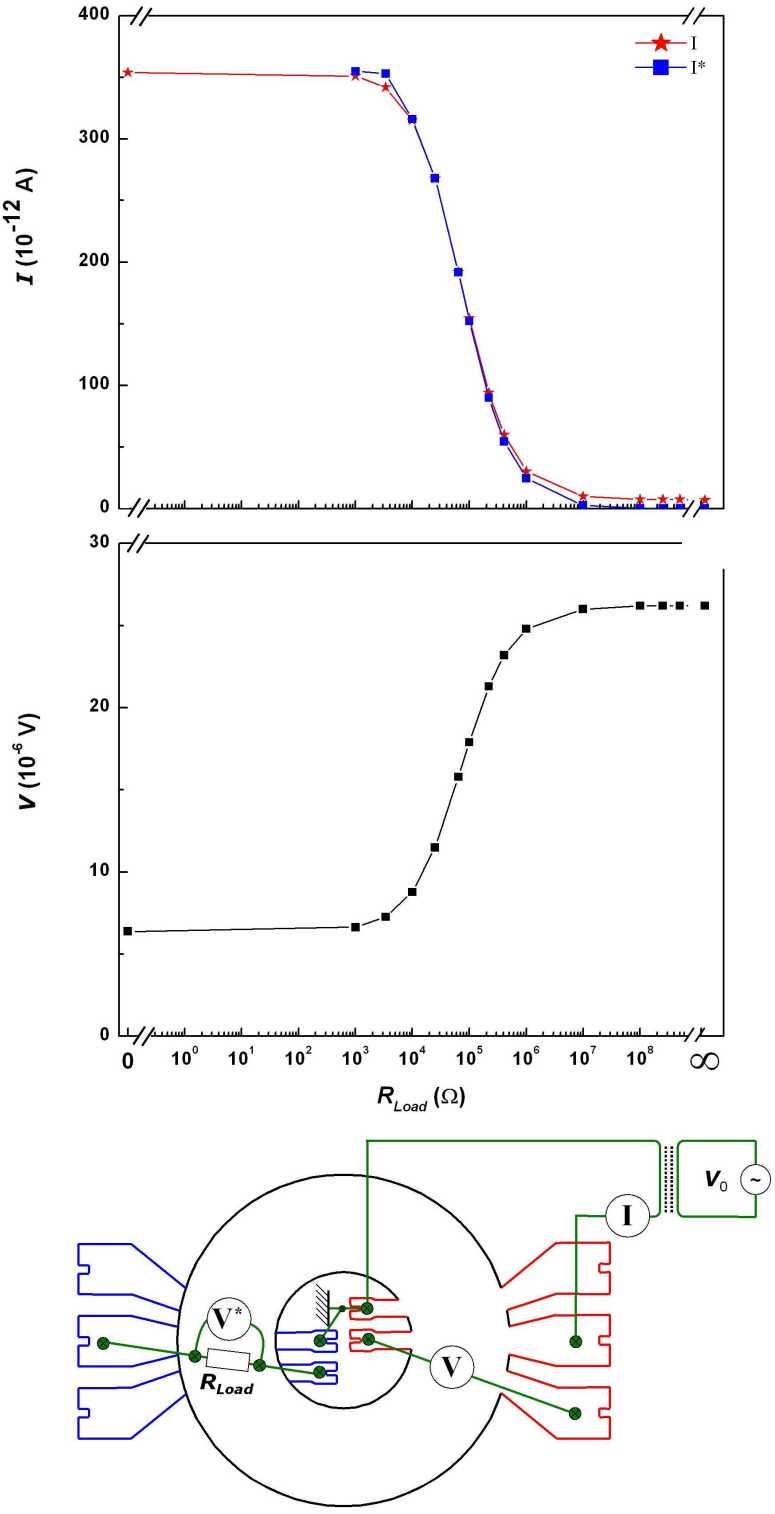

Figure 6.20: Experimental results of a load configuration experiment. The top panel shows the current I through the circuit of the drive layer and the current $I^* = V^*/R_{Load}$ through load resistance as a (log) function of R_{Load}. The mid panel shows the current across the drive layer. The bottom panel illustrates the experimental setup. Sample 81652:146C at d/l_B=1.58 and $T_{bath} \approx 14$ mK.

While the quasiparticle tunneling by itself is able to account for the data presented in Figure 6.20, it cannot *directly* demonstrate that this configuration really triggers such an excitonic current through the bulk of the $\nu_{tot} = 1$ quantum Hall state or not. It may also be possible that the bulk excitons remains completely inert and some additional tunneling process is taking place.

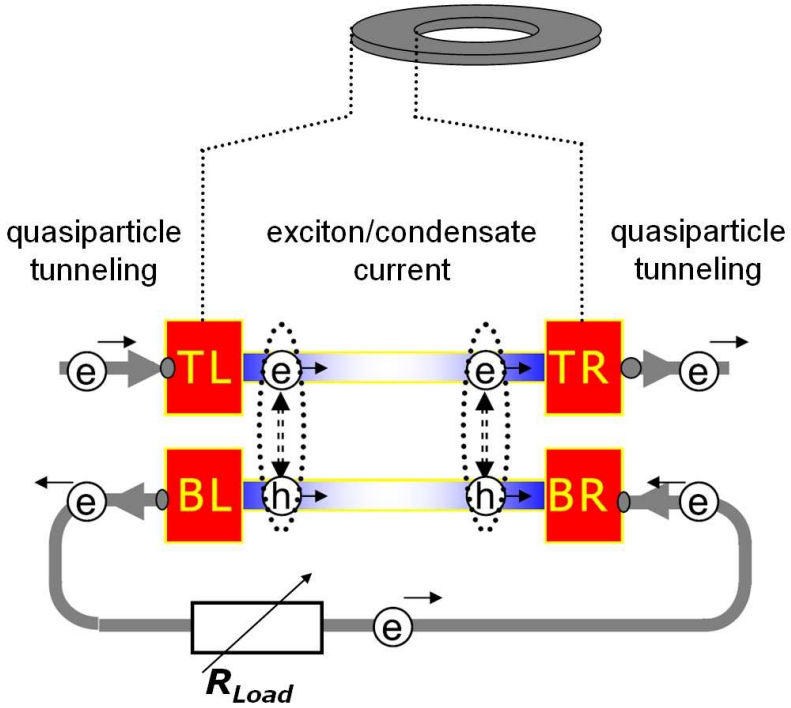

Figure 6.21: Load configuration. An incident single electron at the outer top-left (TL) perimeter is changed into a quasiparticle which launches an exciton/condensate current in the bulk. To conserve total charge, an electron is reflected back into the leads at the outer bottom-left (BL) perimeter. When the outer (L) and inner (R) perimeter are connected via a resistive link, the electron can flow across this bridge and undergo the same process at the other edge, where the condensate current is absorbed. Modified from [Su2008].

All experimental anomalies associated with bilayer exciton condensation require only that the quasiparticle tunneling amplitude be dramatically enhanced compared to the bare regular single electron tunneling splitting $\Delta_{S,AS}$. The single electron interlayer tunneling however is responsible for creating and annihilating excitons and it thus determines the length scale over which steady state collective currents can exists and the value of the critical current. The bare electron tunneling is also expected to be the dominant process which fixes a preferred phase[8]. It however has little effect on the transport properties [Su2008].

[8]It determines "how" spontaneously phase-coherence is established.

6.7 Chapter Summary

Interlayer tunneling experiments were performed in three different configurations. The commonly used 2-terminal AC modulation technique had shown inconsistencies with earlier publications where the $\nu_{tot} = 1$ tunneling anomaly increased in width which led to a simplified 4-terminal DC experiment. These DC measurements could for the first time clearly demonstrate the existence of critical currents $I_{critical}$. As long as the total current is below $I_{critical}$, the 4-terminal interlayer voltage/resistance is strongly reduced. The small interlayer voltage was able to account for the observation in the modulated experiments. The value of the 4-terminal voltage below $I_{critical}$ depends on temperature, the coupling parameter d/l_B and the choice of voltage probes. If these factors are taken into consideration and if the gate voltages are adjusted while sweeping the interlayer bias, the 4-terminal interlayer voltage on Hall bars becomes vanishingly small so that the I/V characteristic resembles the one from the Josephson-effect of superconductivity. Tunneling in the load configuration on Corbino rings is believed to trigger an exciton supercurrent inside the bulk of the $\nu_{tot} = 1$ system.

6.8 Outlook

As previously mentioned, if the quasiparticle tunneling is occurring in the vicinity of the sample edges, then one would expect a dependence of tunneling conductance on the length of the edges. Unlike Hall bars, the Corbino device allows direct investigation of such a dependence on a single sample since inner and outer perimeter differ in length. A simple model can be used to evaluate a dependence of the tunneling on the length of the two perimeters. In the first naïve approach, the tunneling conductance G is directly related to the (one-dimensional) circumference of the ring $U = 2r\pi$, i.e., the ratio U_o/U_i of the outer (o) and inner (i) circumference should correspond to the ratio of the tunneling conductances G_o/G_i for tunneling between either inner or outer edges (see left-hand side of Figure 6.22). However, a better approximation can be found by assuming a strip of constant width w near each sample edge, over which tunneling is enhanced (shaded area on the right-hand side of Figure 6.22). The area of this strip for the inner edge is then $A_i = \pi((r_i + w)^2 - r_i^2) = \pi w(w + 2r_i)$ and for the outer strip $A_o = \pi(r_o^2 - (r_o - w)^2) = \pi w(2r_o - w)$. The ratio of both tunneling conductances $C \equiv G_o/G_i$ is an empirical value. Thus, the equation $C = \frac{2r_o - w}{w + 2r_i}$ can be solved to find w which is

$$w = -2\frac{Cr_i - r_o}{1 + C}. \tag{6.6}$$

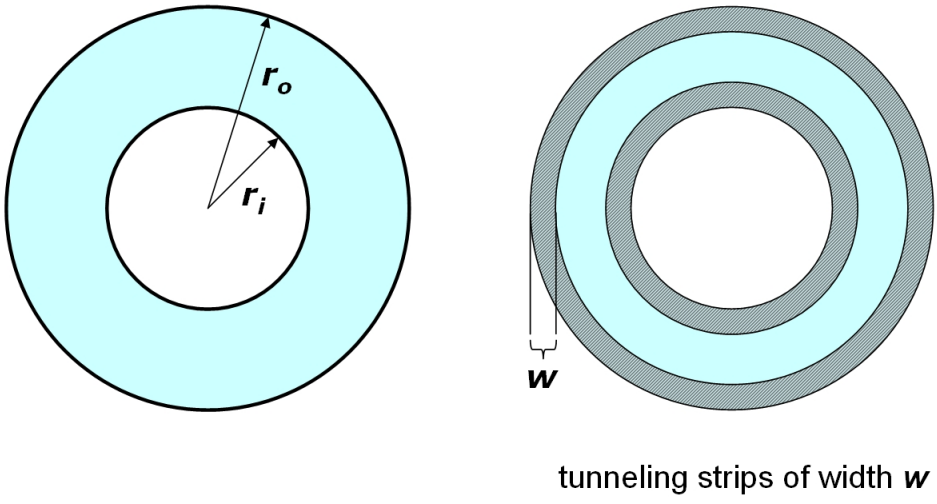

Figure 6.22: Left-hand side: tunneling is directly proportional to the one-dimensional circumference $U = 2r\pi$ of the inner and outer edge. A better approximation assumes that tunneling occurs over a strip of with w near each sample edge (right-hand side). This width w is assumed to be identical for inner and outer edge.

If no apparent dependence on the length of the perimeters is to be found, this could

simply mean that the width w of the strips is not constant for both edges. Thus, instead of having an uniform w, there exists a $w_i > w_o$ which satisfy the condition $A_i \approx A_o$. This however is equivalent to the statement that tunneling depends on the area of the sample. If this is the case, then equating both strip areas yields

$$w_i = -r_i + \sqrt{r_i^2 + 2r_o w_o - w_o^2}, \tag{6.7}$$

where there exists the boundary condition (as given by the empirical data) that both strips cannot overlap, i.e., $r_i + w_i < r_o - w_o$. Assuming a sample with $r_o = 430$ μm and $r_i = 160$ μm (such as sample 81653:146C) then Figure 6.23 shows how the width of the inner strip w_i depends on the width of the outer strip w_o if $A_i = A_o$. Only below the black dotted line the boundary condition that both strips cannot overlap is met.

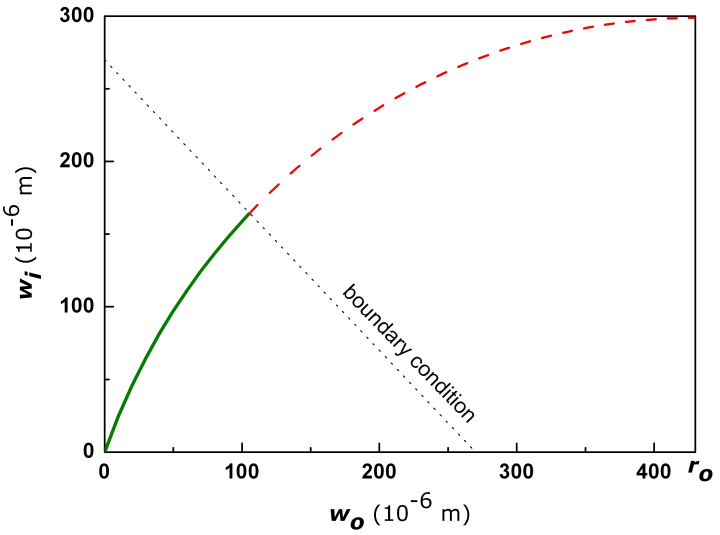

Figure 6.23: Dependence of the width of the inner strip w_i on the width of the outer strip w_o (green solid and red dashed line). Only below the black dotted line both strips do not overlap.

Experiments have to show whether these models reflect the physical reality.

Chapter 7

Summary and Conclusion

The total filling factor one quantum Hall state occurs between two two-dimensional electron systems (2DES). When the separation between the two 2DES is sufficiently small, electron correlation effects can lead to an energy gap which would not occur in an individual 2DES. This correlated state can be viewed in terms of a Bose condensate of interlayer excitons which exhibits interlayer phase-coherence, and a spatial variation of its order parameter ϕ is associated with a dissipationless flow of excitons, comparable to the superfluidity of Helium. However, this (possible) exciton condensate in quantum Hall systems is not exactly like a regular condensate of non-interacting or weakly interacting Bosons - but has many elements in common.

Magneto-transport experiments performed on electron double layer Hall bars at total filling factor 1 had suggested that the conductivity may become fairly large when the correlated state is firmly established [Kel2004]. However, the boundary conditions imposed by the Hall bar geometry did not grant direct access to the conductivity and also raised doubts whether the observed behavior may not only simply be the signature of the regular quantum Hall effect. A Corbino ring geometry, which is generally used to investigate directly the σ_{xx} component of the conductivity tensor, was suggested. However, a regular Corbino ring which generally consists of three concentric rings, i.e., two Ohmic contacts and the 2DES, does not allow independent contact to both layers. To perform interlayer drag and tunneling measurements the total filling factor one state was investigated with a *quasi*-Corbino ring, i.e., an annulus with contact arms attached to both circumferences.

Interlayer drag experiments were performed on such a quasi-Corbino ring, where one 2DES is the active (drive) layer, i.e., where a voltage is applied, and the other 2DES is a passive (drag) layer. It was found that when the magnetic field approaches a value that corresponds to a total filling factor of 1, a drag voltage appears which is identical in sign and magnitude to the voltage across the drive layer, as soon as the coupling parameter is

sufficiently small. At the same time, a minimum in the current through the drive layer can be observed. When the state is firmly established, the conductance $G = I/V$ of the drive layer is vanishingly small. In this situation the $\nu_{tot} = 1$ state resembles the other regular integer filling factors, where the radial current through the bulk is zero, because there is only an azimuthal (circling) part. Thus, the question is if at $\nu_{tot} = 1$ circling currents in the drive layer could be present which by the strong interlayer correlation create a circling current of the same magnitude in the drag layer, leading to identical voltages across both layers. However, certain aspects suggest that another mechanism is at work, which is directly related to the interlayer phase-coherence. While a (possible) macroscopic wave function of the Bose-condensate of interlayer excitons would not only have to exist across the entire active sample area, it will also exist *between* the layers, making it impossible to determine in which layer an electron (or hole, for that matter) is in. Identical voltages are then the result of these coherently spread electrons which equilibrate any potential difference between the layers. As the bulk of the correlated system is impenetrable for any current, it appears that this "layer connection governed by coherently-spread electrons" is limited to a region (of unknown width) near the sample edges. It may as well be that the edges are therefore in a state like the regular integer quantum Hall effect (of single layer filling factor 1). This would explain the similarities in the magneto-transport data between $\nu = 1$ and $\nu_{tot} = 1$. The interior of the bulk, on the other hand, could consist of inert interlayer excitons which are indifferent to any electrical and/or magnetic field.

Increasing the temperature has found to delay the emergence of the total filling factor 1 state towards lower coupling parameters d/l_B, i.e., it requires a lower d/l_B to observe identical voltages across both layers. This also means that increasing d/l_B at lowest temperatures results in a similar behavior than increasing the temperature at low d/l_B. Nevertheless, the smooth transition from two uncorrelated layers each at filling factor 1/2 to a correlated bilayer system on decreasing the temperature and/or d/l_B appears to support the notion of a puddle model [Ste2002]. In this model some areas of the active region are in a state of interlayer phase-coherence while others are still uncorrelated. When the coupling is increased (by lowering the temperature or density and magnetic field) these regions grow and eventually percolate. For that reason the bilayer system is not instantaneously transferred between both states and no phase transition with a discontinuity can be found.

The motivation for investigating the total filling factor 1 state in Corbino rings was the notion that its conductivity may become very large in an equivalent experiment to the Hall bar counter-flow configuration. However, as the bulk of a Corbino ring is impenetrable for single electron current, it is evident that such an analogy cannot be easily made and that the results in Hall bars may simply be due to the edges which connect

source and drain. Nevertheless, contrary to naïve expectations, bilayer superfluidity in magneto-transport may be apparent in the *disappearance* of the conductance and not in its strong increase, since the exciton formation opens up an energy gap around the Fermi energy. In this situation no regular current can be injected into the superfluid phase. The effects observed in Hall bars are then only the manifestations of edge channels.

Interlayer tunneling experiments on both Corbino rings and Hall bars were conducted. Instead of finding a tunneling conductance dI/dV anomaly with a small width and a high amplitude at a total filling factor 1 in AC modulated measurements, the width of the tunneling conductance peak was very broad and appeared to increase with a decreasing coupling parameter. As the interlayer resistance is large compared to other resistances in the circuit for $\nu_{tot}^{-1} \lesssim 0.50$, it was assumed that 2-terminal measurements were sufficient at $\nu_{tot}^{-1} = 1$ as well. This, however, is not the case anymore, once the system exhibits interlayer phase-coherence. In this situation, both the (4-terminal) DC interlayer bias and the AC modulation decrease with decreasing d/l_B. Since the 4-terminal interlayer resistance is then (much) smaller than other series resistances, only a small fraction of the 2-terminal voltage drops across the barrier. Thus, the width of the tunneling anomaly appears to increase, if dI/dV is plotted versus this 2-terminal voltage.

Pure DC interlayer tunneling measurements were performed which (also) had shown that for sufficiently strong interlayer correlation, the 4-terminal interlayer resistance is very small. However, as soon as a critical current $I_{critical}$ is exceeded, the enhanced tunneling quenches *abruptly*, leading to a 4-terminal resistance comparable to the 2-terminal one. The value of the residual 4-terminal interlayer resistance for $I < I_{critical}$ depends on the choice of contacts, the parameter d/l_B and the temperature. It was also found that when the density imbalance that is imposed by the interlayer bias, is compensated for, the 4-terminal interlayer resistance can be further reduced. If the current is plotted versus the 4-terminal instead of the 2-terminal voltage, the I/V characteristic resembles those of the Josephson effect of superconductivity. The sign of the 4-terminal voltage in the regime of interlayer phase-coherence appears to be influenced by the choice of contacts. If the interlayer voltage is probed across the boundary of a quantum Hall system (such as the width of a Hall bar bilayer) its sign was found to depend on the sign of the magnetic field. This contact dependence however requires further systematic investigation.

The enhanced tunneling is explainable in terms of a model which assumes a process analogues to Andreev reflection. In this model, every incident electron from the leads of one layer will meet the correlated state of the active region somewhere near the sample boundary. Once that happens, it is changed into a quasiparticle of the condensate. Owing to the interlayer phase-coherence, the quasiparticle is easily transferred between layers,

and it is then reflected back into the leads of the other layer to conserve total charge. However, this enhanced quasiparticle tunneling is limited to an area of unknown width close to the sample edges, since it remains impossible to observe enhanced interlayer tunneling across the annulus of a Corbino ring. Thus, the quasiparticle lifetime appears to be rather short. When the interlayer bias is increased, the imposed electrochemical potential difference by the leads increases the quasiparticle tunneling beyond a critical point and it stops altogether.

In a complementary tunneling experiment, a Corbino ring was set-up as in a drag experiment. At total filling factor 1, a variable resistor R_{Load} was then applied between the inner and outer circumference of the drag layer. For $R_{Load} \to \infty$, the system displayed the total filling factor one state with a strongly reduced conductance of the drive layer and a large drag voltage (equal to the drive voltage). However, as R_{Load} was slowly reduced to zero, the current through the circuit of the drive layer increased again, and it was identical in magnitude and sign to the current that was now flowing through R_{Load}. Here, the resistive link which connects both perimeters of the drag layer allows the electrons to shortcut the gapped bulk of the total filling factor one state. Despite the presence of the excitonic condensate in the bulk (which remains unaffected), now a current can flow which is maintained by the quasiparticle tunneling at both sample edges. It is argued [Su2008] that with each incident electron, an exciton is launched in the bulk, driven by the large potential difference between the inner and outer edge of the drive layer. This exciton supercurrent can progress from one side of the sample to the other because of the link in the drag layer that allows a steady state current. As the drive current is identical in sign and magnitude to the drag current (which are both measured bulk-externally), it implies that bulk-internally currents of opposite direction may flow, i.e., an excitonic supercurrent. However, there is no direct way to probe the properties of the bulk using regular transport experiments.

Ring-shaped (i.e., Corbino) bilayer samples have been able to provide a deeper insight into the physics of the total filling factor one state. Since Corbino rings allow a separation between bulk- and edge-transport, this experimental work was able to distinguish between edge effects which are carried by quasiparticles and the physics of the bulk, and it demonstrated for the first time the existence of critical currents at $\nu_{tot} = 1$ in four-terminal (DC) measurements.

Bibliography

[Ahl2002] E. Ahlswede, *PhD thesis, Max-Planck Institut for Solid State Research, Stuttgart* (2002).

[Bal2001] L. Balents and L. Radzihovsky, *Phys. Rev. Lett.* **86**, 1825 (2001).

[Bla1962] J. M. Blatt and K. W. Böer and W. Brandt, *Phys. Rev.* **126**, 1691 (1962).

[Boe1990] G. S. Boebinger and H. W. Jiang and L. N. Pfeiffer and K. W. West, *Phys. Rev. Lett.* **64**, 1793 (1990).

[Bue1988] M. Buettiker, *Phys. Rev. B* **38**, 9375 (1988).

[But2004] L. V. Butov, *J. Phys.: Condens. Matter* **16**, R1577 (2004).

[Cer2008] Dilution Refrigeration, *http://na47sun05.cern.ch/target/outline/dilref.html* (2008).

[Cha1994] T. Chakraborty and P. Pietilainen, *The fractional quantum Hall effect.* Springer Verlag (1994).

[Chm2008] A R. Champagne and J. P. Eisenstein and L. N. Pfeiffer and K. W. West, *Phys. Rev. Lett.* **100**, 096801 (2008).

[Che2006] Y. P. Chen, *Phys. Rev. B* **73**, 115314 (2006).

[Chk1992] D. B. Chklovskii and B. I. Shklovskii and L. I. Glazman, *Phys. Rev. B* **46**, 4026 (1992).

[Coh1997] C. Cohen-Tannoudji and B. Diu and F. Laloë, *Quantenmechanik Teil 1.* W. de Gruyter (1997).

[Cot1992] R. Cote and L. Brey and A. H. MacDonald, *Phys. Rev. B* **46**, 10239 (1992).

[Dat1995] S. Datta, *Electronic transport in mesoscopic systems.* Cambridge University Press (1995).

[Dem2001] E. Demler and C. Nayak and S. D. Sarma, *Phys. Rev. Lett.* **86**, 1853 (2001).

[Kla1991] U. Klass and W. Dietsche and K. von Klitzing and K. Ploog, *Z. Phys. B* **82** (1991).

[Eis1990b] J. P. Eisenstein and L. N. Pfeiffer and K. W. West, *Phys. Rev. Lett.* **57**, 2324 (1990).

[Eis1990a] J. P. Eisenstein and H. L. Stoermer, *Science* **248**, 1510 (1990).

[Eis1991] J. P. Eisenstein and L. N. Pfeiffer and K. W. West, *Appl. Phys. Lett.* **58**, 1497 (1991).

[Eis1992] J. P. Eisenstein and L. N. Pfeiffer and K. W. West, *Phys. Rev. Lett.* **69**, 3804 (1992).

[Ens2000] C. Enss and S. Hunklinger, *Tieftemperaturphysik*. Springer Verlag (2000).

[Eza1993] Z. F. Ezawa and A. Iwazaki, *Phys. Rev. B* **47**, 7311 (1993).

[Fer1989] H. A. Fertig, *Phys. Rev. B* **40**, 1087 (1989).

[Fog2001] M. M. Fogler and F. Wilczek, *Phys. Rev. Lett.* **86**, 1833 (2001).

[Fro1986] H. Fronius and A. Fischer and K. Ploog, *J. Appl. Phys.* **25**, 137 (1986).

[Goe2004] J. Göres, *PhD thesis, Max-Planck Institut for Solid State Research, Stuttgart* (2004).

[Gir1984] S. M. Girvin, *Phys. Rev. B* **29**, 6012 (1984).

[Gir2000] S. M. Girvin, *Physics Today* **53**, 39 (2000).

[Gir2002] S. M. Girvin, *Phys. Scripta* **102**, 112 (2000).

[Gra1993] T. J. Gramila and J. P. Eisenstein and A. H. MacDonald and L. N. Pfeiffer and K. W. West, *Phys. Rev. B* **47**, 12957 (1993).

[Gud1987] V. Gudmundsson and R. R. Gerhardts, *Phys. Rev. B* **35**, 8005 (1987).

[Giu2008] P. Giudici and K. Muraki and N. Kumada and Y. Hirayama and and T. Fujisawa, *Phys. Rev. Lett.* **100**, 106803 (2008).

[Hal1983] B. I. Halperin, *Helv. Phys. Acta* **56**, 75 (1983).

[Hoh1967] P. C. Hohenberg, *Phys. Rev.* **158**, 383 (1967).

[Har1999] P. Harrison, *Quantum Wells, Wires and Dots*. John Wiley and Sons, Inc. (1999).

[Hu1992] J. Hu and A. H. MacDonald, *Phys. Rev. B* **46**, 12559 (1992).

[Hus2005] D. A. Huse, *Phys. Rev. B* **72**, 064514 (2005).

[Jai1989] J. K. Jain, *Phys. Rev. Lett.* **63**, 199 (1989).

[Jec2001] B. Jeckelmann and B. Jeanneret, *Rep. Prog. Phys.* **64**, 1603 (2001).

[Jog2006] Y. N. Joglekar and A. V. Balatsky and S. D. Sarma, *Phys. Rev. B* **74**, 233302 (2006).

[Jog2000] Y. N. Joglekar and A. H. MacDonald, *Physica E* **6**, 627 (2000).

[Joe2000] C. Jörger and W. Dietsche and W. Wegscheider and K. von Klitzing, *Physica E* **6**, 586 (2000).

[Kel1968] L. V. Keldysh and A. N. Kozlov, *Sov. Phys. JETP* **27**, 521 (1968).

[Kel1965] L. V. Keldysh and Y. E. Kopaev, *Sov. Phys. Solid State* **6**, 6219 (1965).

[Kel2002] M. Kellogg and I. B. Spielman and J. P. Eisenstein and L. N. Pfeiffer and K. W. West, *Phys. Rev. Lett.* **88**, 126804 (2002).

[Kel2004] M. Kellogg and J. P. Eisenstein and L. N. Pfeiffer and K. W. West, *Phys. Rev. Lett.* **93**, 036801 (2004).

[Kli1980] K. v. Klitzing and G. Dorda and M. Pepper, *Phys. Rev. Lett.* **45**, 494 (1980).

[Kos1973] J. M. Kosterlitz and D. J. Thouless, *J. Phys. C* **6**, 1181 (1973).

[Lau1982] R. B. Laughlin, *Surface Science* **113**, 26 (1982).

[Lau1983] R. B. Laughlin, *Phys. Rev. Lett.* **50**, 1395 (1983).

[Lie1994] K Lier and R. R. Gerhardts, *Phys. Rev. B* **50**, 7757 (1994).

[Lil1998] M. P. Lilly and J. P. Eisenstein and L. N. Pfeiffer and K. W. West, *Phys. Rev. Lett.* **80**, 1714 (1998).

[Mac0708] Personal correspondence with A. H. MacDonald.

[Mer1966] N. D. Mermin and H. Wagner, *Phys. Rev. Lett.* **22**, 1133 (1966).

[Mit1996] A. Mittal and R. G. Wheeler and M. W. Keller and D. E. Prober and R. N. Sacks, *Surf. Sci.* **361/362**, 537 (1996).

[Moo1995] K. Moon and H. Mori and Kun Yang and S. M. Girvin and A. H. MacDonald and L. Zheng and D. Yoshioka and Shou-Cheng Zhang, *Phys. Rev. B* **51**, 5138 (1995).

[Mur1994] S. Q. Murphy and J. P. Eisenstein and G. S. Boebinger and L. N. Pfeiffer and K. W. West, *Phys. Rev. Lett.* **72**, 728 (1994).

[Mur1995] S. Q. Murphy and J. P. Eisenstein and L. N. Pfeiffer and K. W. West, *Phys. Rev. B* **52**, 14825 (1995).

[Mue1990] G. Müller and D. Weiss and S. Koch and K. von Klitzing and H. Nickel and W. Schlapp and R. Lösch, *Phys. Rev. B* **42**, 7633 (1990).

[Mra2004] K. Muraki and J. G. S. Lok and S. Kraus and W. Dietsche and K. von Klitzing and D. Schuh and M. Bichler and W. Wegscheider, *Phys. Rev. Lett.* **92**, 246801 (2004).

[Mra2008] K. Muraki, NTT Basic Research Laboratories

[Paq1985] D. Paquet and T. M. Rice and K. Ueda, *Phys. Rev. B* **32**, 5208 (1985).

[Par2006] K. Park and S. D. Sarma, *Phys. Rev. B* **74**, 35338 (2006).

[Pra1987] R. E. Prange and S. M. Girvin, *The Quantum Hall Effect*. Springer Verlag (1987).

[Roo2008] B. Roostaei and K. J. Mullen and H. A. Fertig and S. H. Simon, *arXiv:0804.1148* (2008).

[Ros2005] E. Rossi and A. S. Nunez and A. H. MacDonald, *Phys. Rev. Lett.* **95**, 26604 (2005).

[Rub1997] H. Rubel and A. Fischer and W. Dietsche and K. von Klitzing and K. Eberl, *Phys. Rev. Lett.* **78**, 1763 (1997).

[Sar1997] S. D. Sarma and A. Pinczuk, *Perspectives in quantum Hall effects*. John Wiley and Sons, Inc. (1997).

[Sni2008] G. Snider, *http://www.nd.edu/ gsnider/* (2008).

[Sno2002] D. Snoke, *Science* **298**, 1368 (2002).

[Spi2000] I. B. Spielman and J. P. Eisenstein and L. N. Pfeiffer and K. W. West, *Phys. Rev. Lett.* **84**, 5808 (2000).

[Spi2001] I. B. Spielman and J. P. Eisenstein and L. N. Pfeiffer and K. W. West, *Phys. Rev. Lett.* **87**, 036803 (2001).

[Spi2004] I. B. Spielman and M. Kellogg and J. P. Eisenstein and L. N. Pfeiffer and K. W. West , *Phys. Rev. B* **70**, 081303(R) (2004).

[Sta1985] E. Stahl and D. Weiss and G. Weimann and K. von Klitzing and K. Ploog, *J. Phys. C* **18**, L783 (1985).

[Ste2001] A. Stern and S. M. Girvin and A. H. MacDonald and N. Ma, *Phys. Rev. Lett.* **86**, 1829 (2001).

[Ste2002] A. Stern and B. I. Halperin, *Phys. Rev. Lett.* **88**, 106801 (2002).

[Sto1999] H. L. Stoermer, *Rev. Mod. Phys.* **71**, 875 (1999).

[Su2008] J.-J. Su and A. H. MacDonald, *arXiv:0801.3694* (2008).

[Tso1992] H. C. Tso and P. Vasilopoulos and F. M. Peeters, *Phys. Rev. Lett.* **68**, 2516 (1992).

[Tsu1982] D. C. Tsui and H. L. Stormer and A. C. Gossard, *Phys. Rev. Lett.* **48**, 1559 (1982).

[Tut2004] E. Tutuc and M. Shayegan and D. A. Huse, *Phys. Rev. Lett.* **93**, 036802 (2004).

[Vei2002] M. Y. Veillette and L. Balents and M. P. A. Fisher, *Phys. Rev. B* **66**, 155401 (2002).

[Wie2004] R. D. Wiersma and J. G. S. Lok and S. Kraus and W. Dietsche and K. von Klitzing and D. Schuh and M. Bichler and H.-P. Tranitz and W. Wegscheider, *Phys. Rev. Lett.* **93**, 266805 (2004).

[Wie2005] R. D. Wiersma, *PhD thesis, Max-Planck Institut for Solid State Research, Stuttgart* (2005).

[Wig1934] E. P. Wiegner, *Phys. Rev.* **46**, 1002 (1934).

[Yan1998] K. Yang, *Phys. Rev. B* **58**, R4246 (1998).

[Yan2001] K. Yang and A. H. MacDonald, *Phys. Rev. B* **63**, 73301 (2001).

[Yos1989] D. Yoshioka and A. H. MacDonald and S. M. Girvin, *Phys. Rev. B* **39**, 1932 (1989).

[Zhe1993] L. Zheng and A. H. MacDonald, *Phys. Rev. B* **48**, 8203 (1993).

[Zhe1993b] L. Zheng and A. H. MacDonald, *Phys. Rev. B* **47**, 10619 (1993).

[Zho1999] F. Zhou and Y. B. Kim, *Phys. Rev. B* **59**, R7825 (1999).

Acknowledgements

In retrospect there seem to be only very few things I have actually done myself. I would like to acknowledge the following people for their support during the last three years:

- *Klaus von Klitzing* for giving me the opportunity to work on a very interesting project and for his suggestions, questions and discussions.
- *Werner Dietsche* for accepting me as a PhD student and for always having the right idea when it comes to solve a physical or technical problem.
- *Günter Reiss* for acting as a member on my defense committee.
- *Jurgen Smet* and *Jürgen Weis* for providing technical support.
- *Sjoerd Lok* for designing the Corbino geometry and his introduction to the topic.
- *Stefan Schmult* for his MBE growth of high-mobility bilayer samples.
- *The entire von-Klitzing group (and alumni)* for being a great bunch of people.
- *Yoshiro Hirayama*, *Koji Muraki* and *the entire NTT staff* for putting up with a "Gaijin". Japan was both a scientific and cultural experience. Also, I would like to thank *Rika Murayama* who was able so solve all other issues (administrative, personal) that arose during my stay in Japan.
- *Manfred Schmid, Ingo Hagel, Steffen Wahl, Walter Schmied* and *Hans Riek* for setting up our new dilution refrigerator.
- *Monika Riek, Thomas Reindl* and *Achim Güth* for keeping the clean room in shape.
- *Ulrike Waizmann* for her introduction to eBeam lithography (which she eventually was doing it for me).
- *Benjamin Stuhlhofer* and *Monika Riek* for bonding my samples.
- *Werner Rauscher* for many repairs and sophisticated constructions.

- *Werner Wegscheider* and *Dieter Schuh* for providing MBE material.
- *Maik Hauser* for growing a great electron double-layer wafer.
- *Ruth Jenz* for being of great help in all administrative questions.
- *Joern Göres* and *Koji Muraki* for providing some Figures for my thesis.
- *Allan H. MacDonald* for discussions.
- *Ady Stern* for making calculations and discussions.
- *...and my family and friends.*

Appendix

Growth Sequence Wafer 81653

material	(deposition) time (s)	thickness (10^{-10} m)	repetitions (entire block)
GaAs	360	1000	
-	3	STOP	12
AlAs	14	20	|
-	3	STOP	|
GaAs	7	20	⊥
AlGaAs	19	80	50
-	3	STOP	|
GaAs	8	23	|
-	3	STOP	⊥
AlGaAs	71	300	
AlGaAs:Si	83	350	
AlGaAs	119	500	
-	20	STOP	
AlGaAs	119	500	5
-	20	STOP	⊥
GaAs	68	190	
-	20	STOP	
AlAs	12	17	5
-	3	STOP	|
GaAs	1	2.8	|
-	3	STOP	⊥
-	20	STOP	
GaAs	67	187	
-	20	STOP	
AlGaAs	660	2800	
-	3	STOP	
AlGaAs:Si	95	400	
-	3	STOP	
AlGaAs	480	2000	
GaAs	71	200	

SURFACE

Si-doped regions ($n \sim 2 \cdot 10^{18}$ cm^{-3}), quantum wells and the barrier are shaded. The composition parameter for AlGaAs $\equiv Al_xGa_{1-x}As$ is x=0.33.

Samples

The following to tables contain all samples that were examined. The tables include the dimensions and the measured interlayer resistances in and out of resonance. Sample references in the main text are given by e.g. 81653:146C, where a "C" after the sample number indicates that it is a Corbino ring and a "H" that it is a Hall bar geometry.

Corbino Samples

wafer	sample	outer diameter (10^{-6} m)	ring width (10^{-6} m)	interlayer resistance at B=0 T *in/out of resonance* (10^6 Ω)	Temp. (K)
81653	146C	860	270	(A) 0.82/100	4.20
				(B) 0.33/>20	0.01
81653	247C	600	140	(A) 1.30/ 42	4.20
				(B) 0.55/ 76	0.25
81653	248C	780	230	(A) 0.88/ 40	4.20
D050803A	267C	480	80	(B) 10/ 25	0.01

Hall Bar Samples

All samples are standard Hall bars of dimension (880 × 80) μm^2.

wafer	sample	interlayer resistance at B=0 T *in/out of resonance* (10^6 Ω)	Temp. (K)
81653	210H	(B) 0.55/>20	0.01

(A): deduced from 2pt I/V characteristic (error ±5%)
(B): deduced from 2pt differential conductance dI/dV

Intrinsic Densities and Mobilities

The table below shows the approximate intrinsic densities and mobilities deduced from magneto-transport sweeps at approximately 15 mK. These values may differ by ± 5 % from sample to sample.

wafer	density upper and lower QW (10^{14} m^{-2})	mobility upper/lower QW (m^2 V^{-1}s^{-1})
81653	~ 4.3	$\sim 65/45$
D050803A		

81653 grown at the Max-Planck Institute in Stuttgart, Germany by M. Hauser

D050803A grown at the University of Regensburg, Germany by D. Schuh and W. Wegscheider

Bilayer Capacitance and Imbalances

A bilayer can be considered to be equivalent to two conducting plates of area A which are separated by a dielectric material of thickness d. The bilayer is thus a capacitor which has the following characteristics:

dielectricity of barrier	$\varepsilon \approx 12$ (ϵ_{GaAs}=13, ϵ_{AlAs}=11)
Hall bar area	A=(80×880)·10^{-12} m^2
layer separation	d=28.6·10^{-9} m.

The capacitance of such a parallel-plate capacitor is given by

$$C = \varepsilon_0 \varepsilon \frac{A}{d} \approx 260 \cdot 10^{-12}\ F, \tag{7.1}$$

with the vacuum permittivity $\varepsilon_0 = 8.8542 \cdot 10^{-12}$ F m^{-1}. The charge transfer between the plates upon applying a voltage of ΔV [V] can be estimated by

$$C \cdot \Delta V = \Delta N \cdot e \tag{7.2}$$

$$\Longrightarrow\ \Delta N = (C \cdot \Delta V)/e, \tag{7.3}$$

where e is the electron charge and N the number of electrons. The *density* change is $\Delta n = \Delta N/A$. For a given (matched) electron density the change in percent can be calculated which has shown to agree well with the results of magneto-transport experiments.